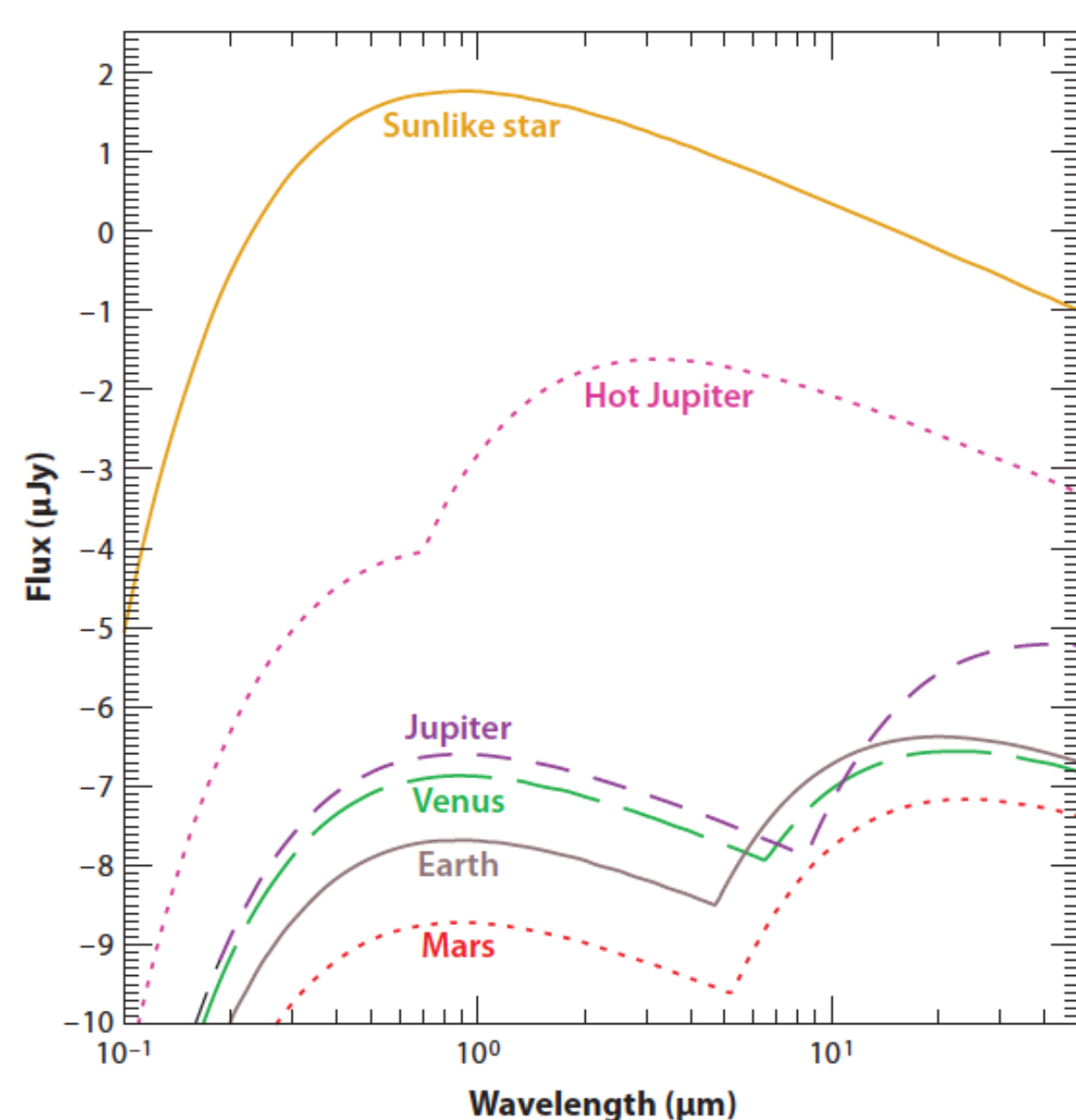


Colors of Alien Worlds from Direct Imaging Exoplanet Missions

Principal Investigator: Renyu Hu (3222)

Reflection of Exoplanets

Current observations of exoplanet atmospheres using the transit technique work the best for planets close to their parent stars. Due to stellar irradiation, these planets generally have warm and hot atmospheres.

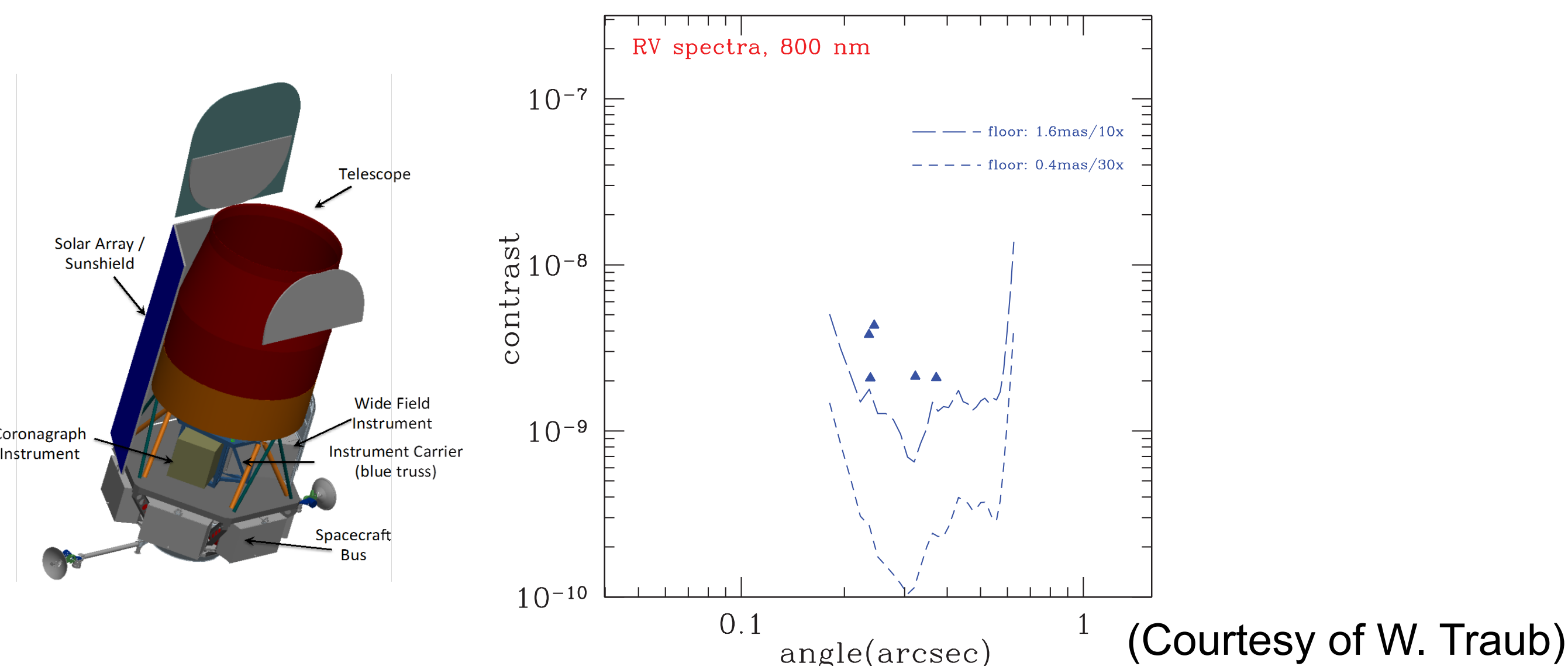


Future direct-imaging exoplanet space missions will provide the capability to directly detect exoplanets of nearby stars. The inner working angles of the missions – the smallest angle at which a planet can be detected – determine that the exoplanets to be observed are sufficiently separated from their parent stars. These exoplanets will have much colder atmospheres and different chemical states than the exoplanets observed currently by the transit technique.

(Seager & Deming 2010)

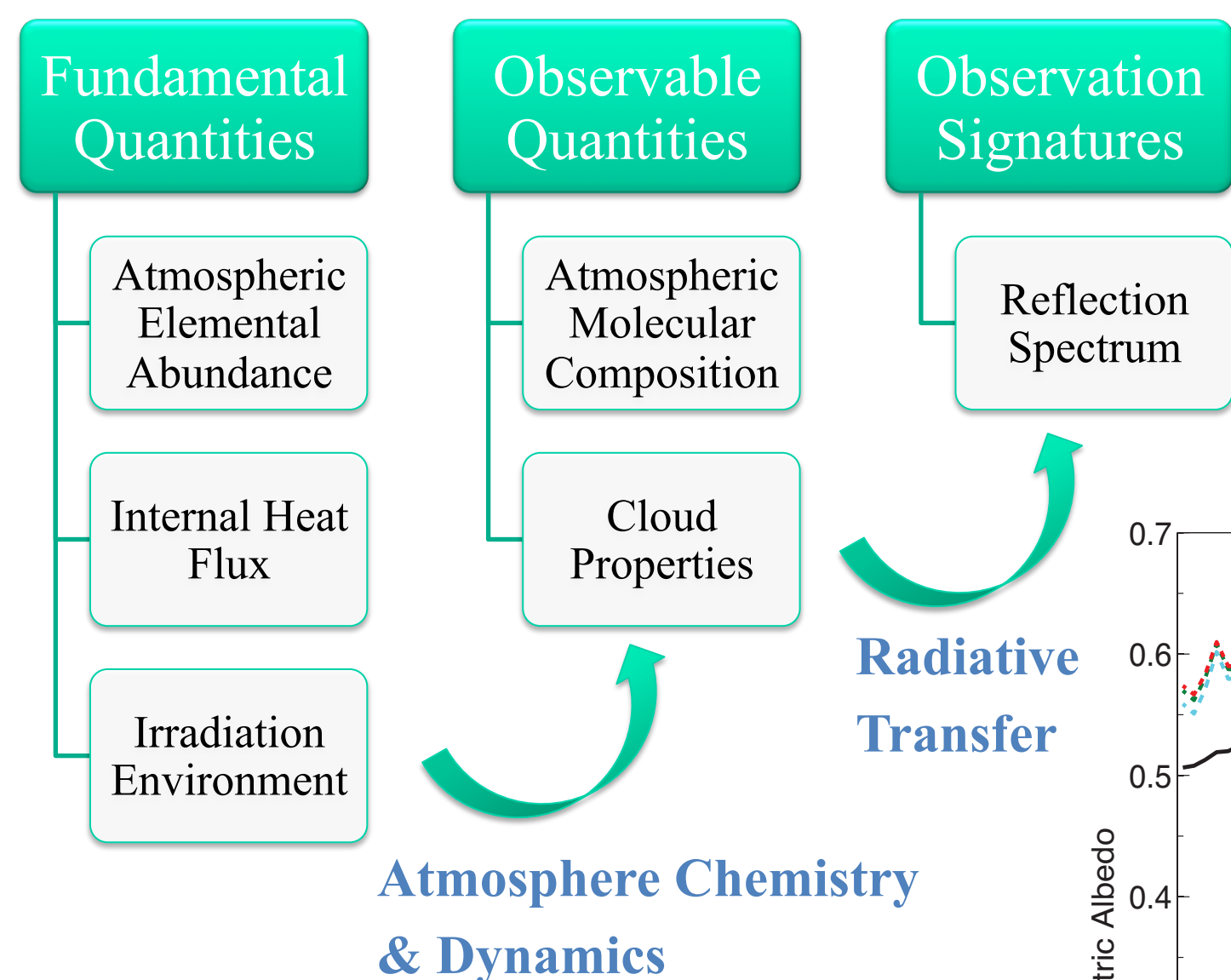
WFIRST-AFTA

The Wide-Field Infrared Survey Telescope (WFIRST) is a NASA observatory designed to perform wide-field imaging and slitless spectroscopic surveys of the near infrared (NIR) sky for the community. The current Astrophysics Focused Telescope Assets (AFTA) design of the mission makes use of an existing 2.4m telescope to enhance sensitivity and imaging performance.

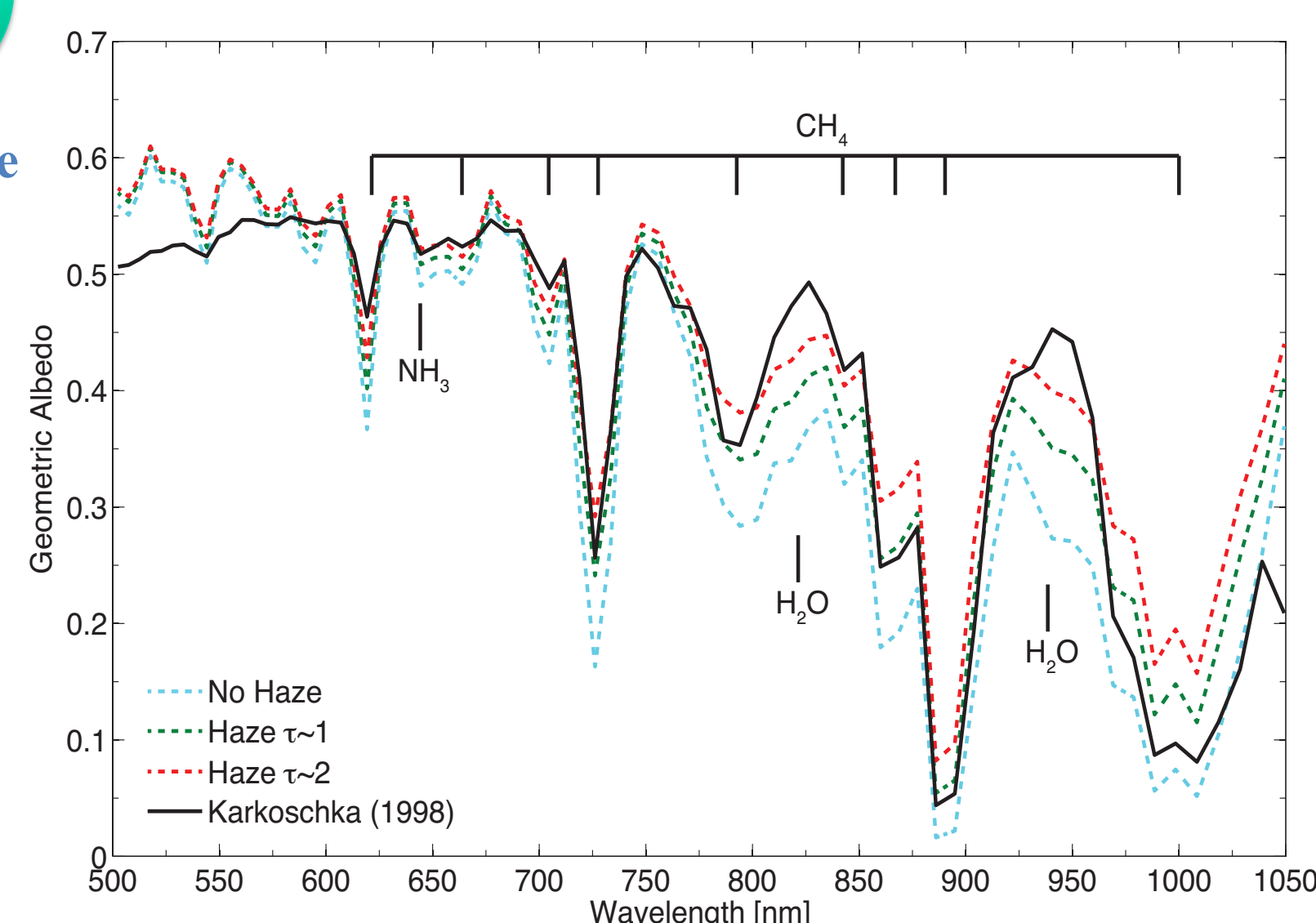


Method

I have developed a state-of-the-art atmospheric chemistry and radiative transfer model for exoplanets based on fundamental principles. The model includes water and ammonia as potential condensable species, estimates the particle size for calculating the optical properties of clouds, and considers the cloud feedback on the adiabatic lapse rate and the albedo of the planet.

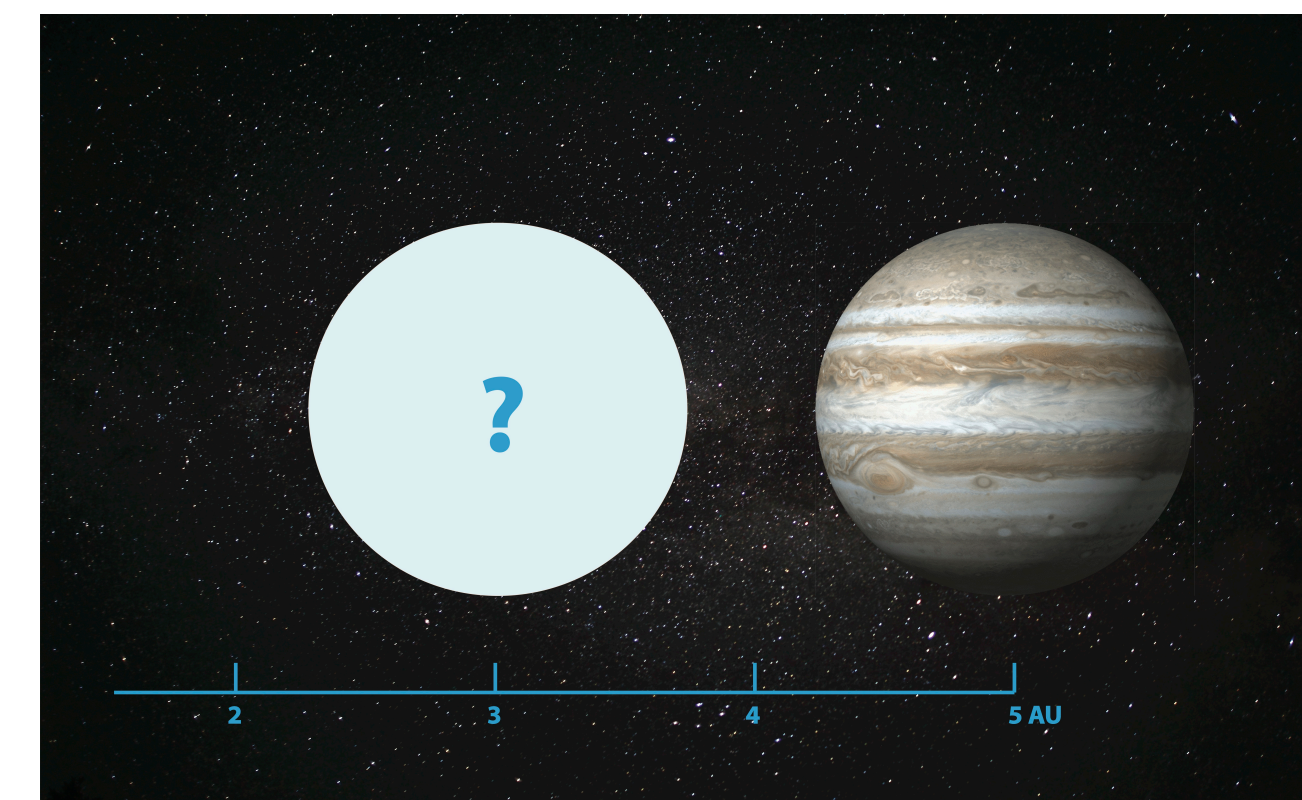


I tested the model by reproducing the temperature-pressure profile, the cloud structure, and the geometric albedo spectrum of Jupiter. An upper tropospheric haze can affect the depths of weak methane bands.



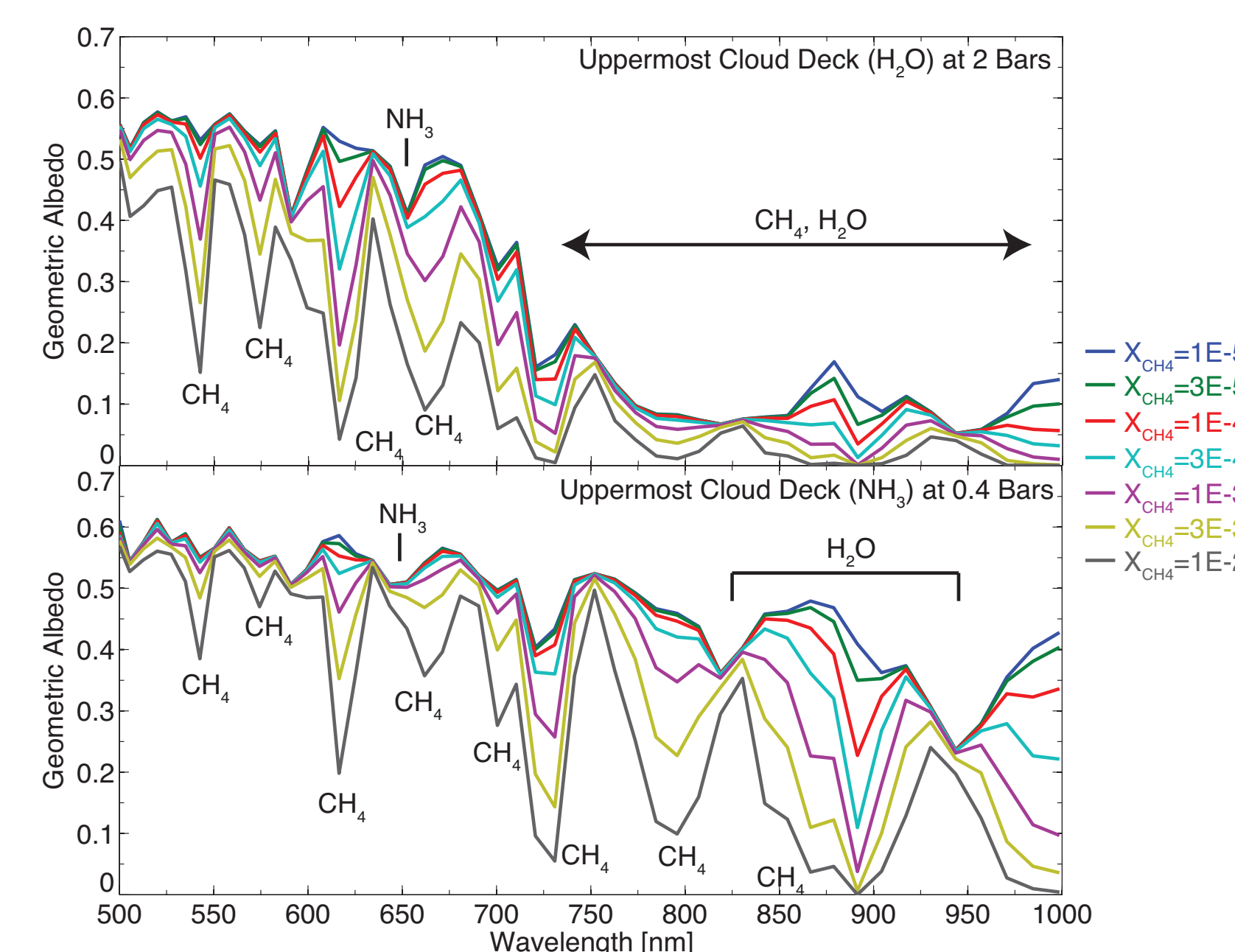
What can we learn about giant exoplanets from their reflection spectra?

Whether clouds exist is the primary factor that controls the appearance of an exoplanet. Rayleigh scattering, molecular absorption, and scattering and absorption by atmospheric condensates determine the reflection spectra of gaseous exoplanets. A great diversity in the possible spectral features of the reflected light of exoplanets can be anticipated.

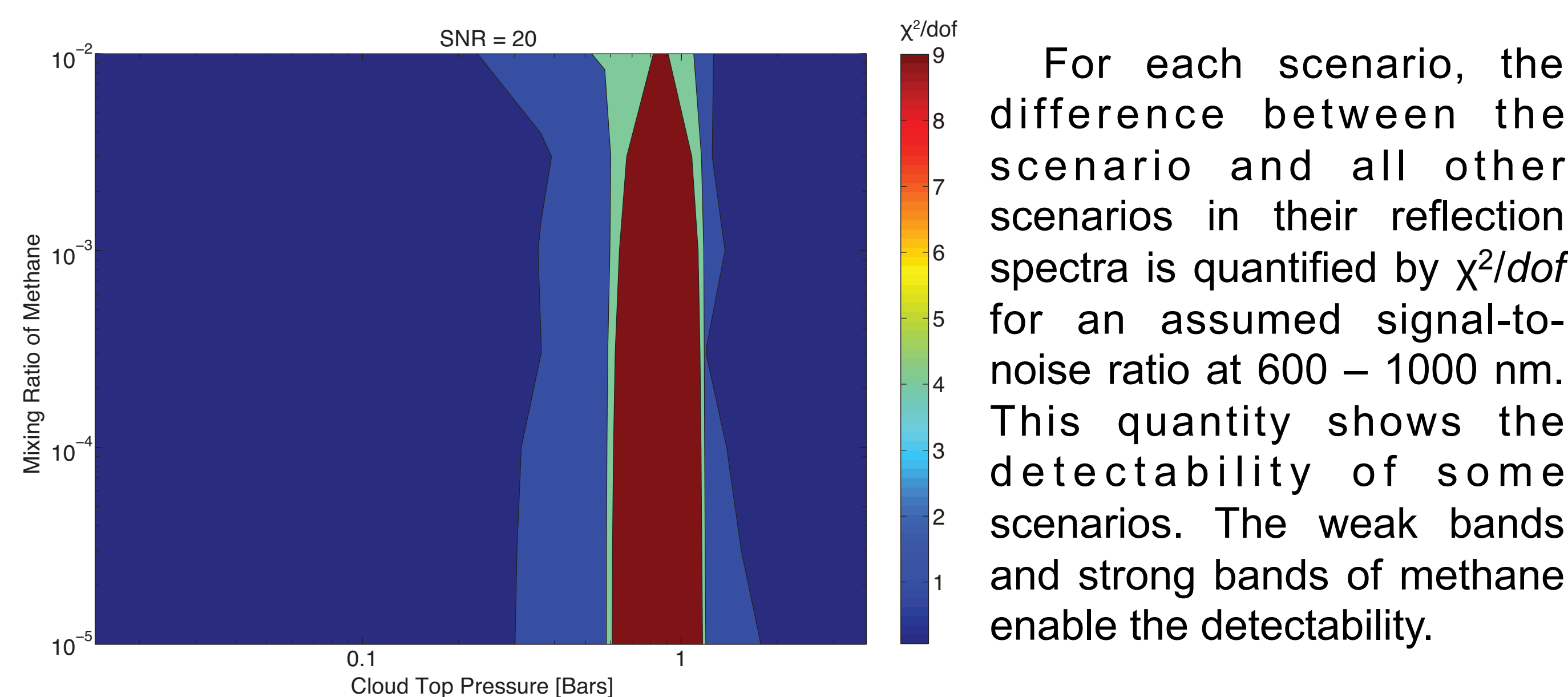


Both the cloud top pressure and the mixing ratio of methane, and other species to a lesser extent, determine the spectral shapes of the exoplanets to be characterized by WFIRST-AFTA.

When the uppermost cloud deck is shallower than ~1 bars (e.g. NH_3 cloud), the methane absorption features are prominent at 700 – 1000 nm when the mixing ratio of methane is higher than 10^{-4} . When the uppermost cloud deck is deeper than ~1 bars (e.g. H_2O cloud), the planet would be very dark at all wavelengths longer than 750 nm, and the methane absorption features are prominent at 600 – 750 nm.

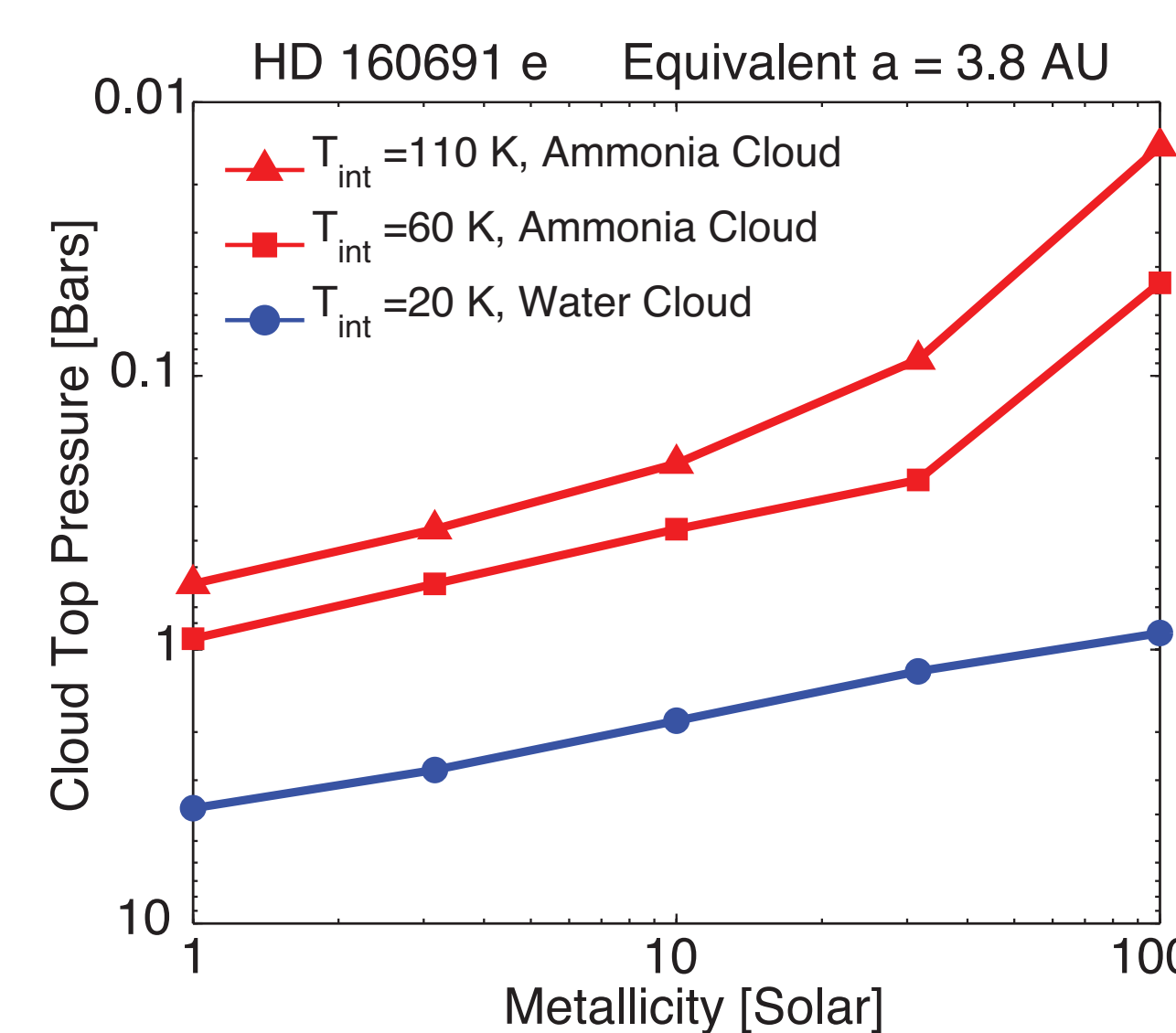


I find that the cloud top pressure and the mixing ratio of methane can be derived unambiguously from a single reflection spectrum with the nominal spectral capability provided by WFIRST-AFTA, if the cloud top pressure is between 0.6 and 1.5 bars.



For each scenario, the difference between the scenario and all other scenarios in their reflection spectra is quantified by χ^2/dof for an assumed signal-to-noise ratio at 600 – 1000 nm. This quantity shows the detectability of some scenarios. The weak bands and strong bands of methane enable the detectability.

The cloud top pressure depends on both the abundances of water and ammonia gas in the atmosphere, and the internal heat flux of the planet. The cloud top pressure does not depend on the methane abundance.



The cloud top is at a lower pressure

- when the planet is closer to the host star;
- when the atmosphere has more H_2O or NH_3 ;
- when the planet has a greater internal heat flux.

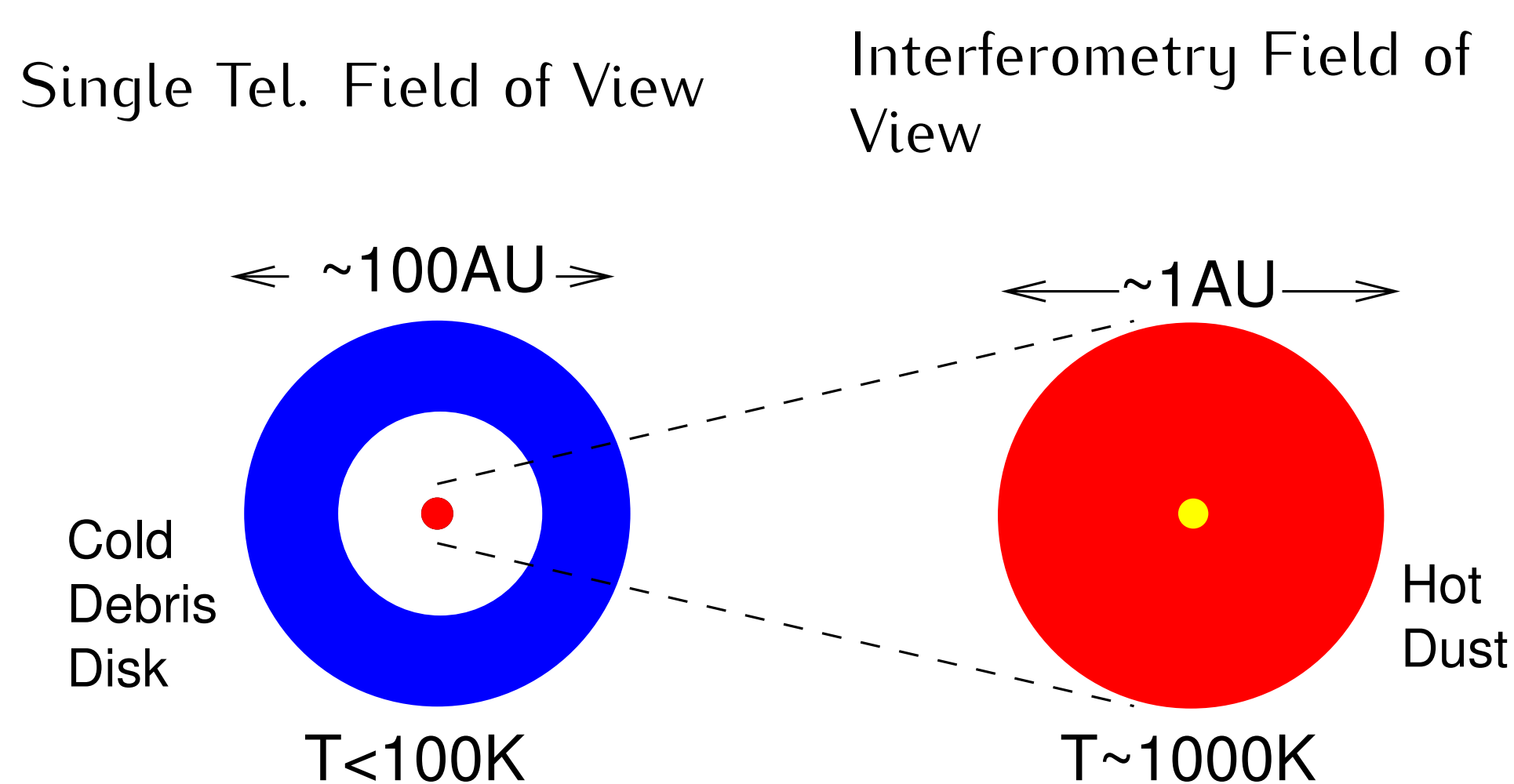
If a matured planet has a very low internal heat flux, NH_3 clouds may not form because of a deep H_2O cloud layer that dissolves NH_3 .

Resolving the Circumstellar Environment Near the Habitable-Zone of Main-Sequence Stars

Principal Investigator: Paul D. Nuñez (3262)

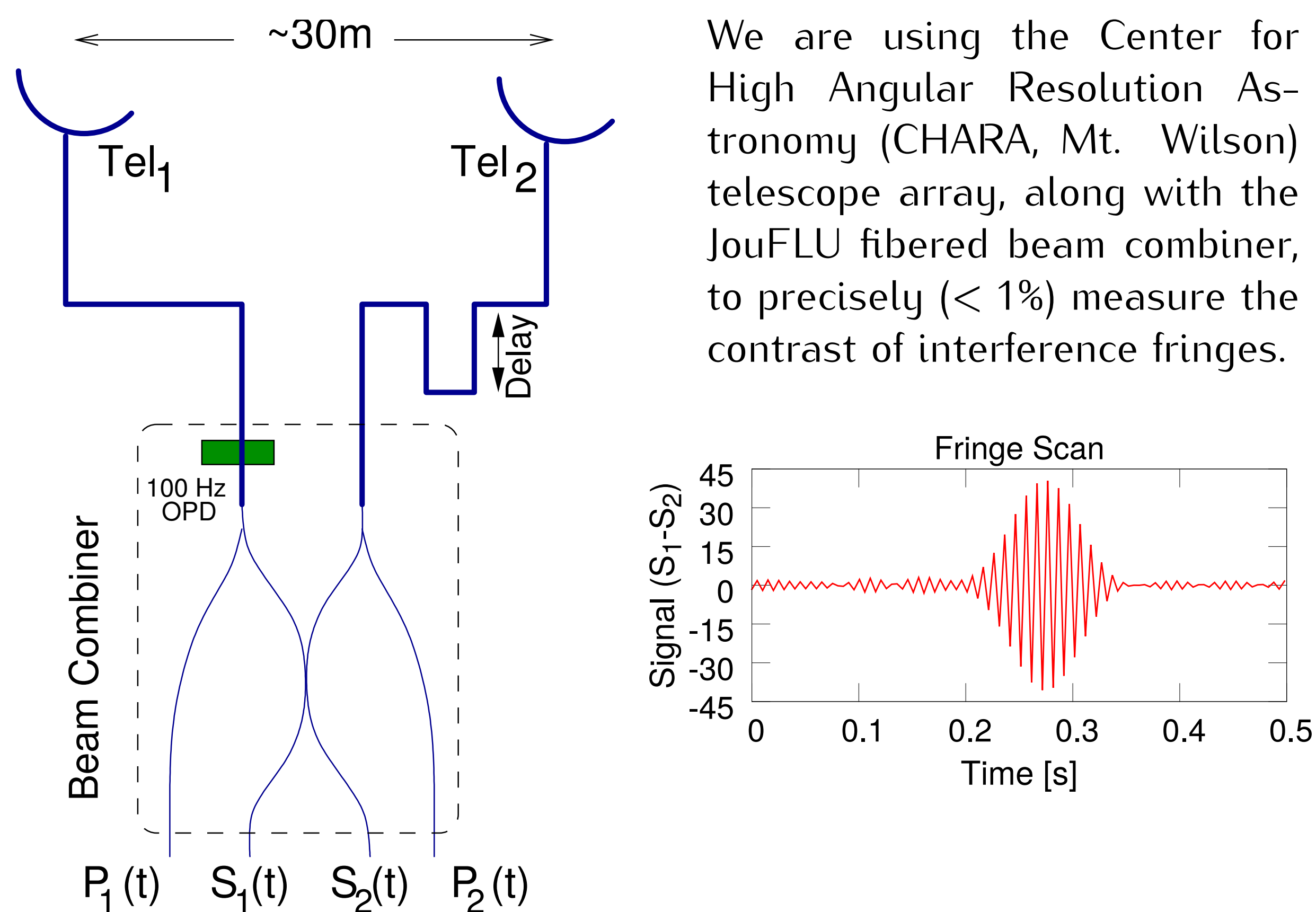
B. Mennesson (3262), N. Scott, T. ten Brummelaar (GSU)

We have been measuring Exozodiacal light levels in the Near Infrared (NIR) around main sequence stars, as part of a NASA Exoplanet Research Program Grant. **NIR Circumstellar excess light within 1AU from neighboring stars most likely originates from hot dust**, which may hint at the existence of exoplanets, but also hinder exoplanet detection with future direct imaging missions.

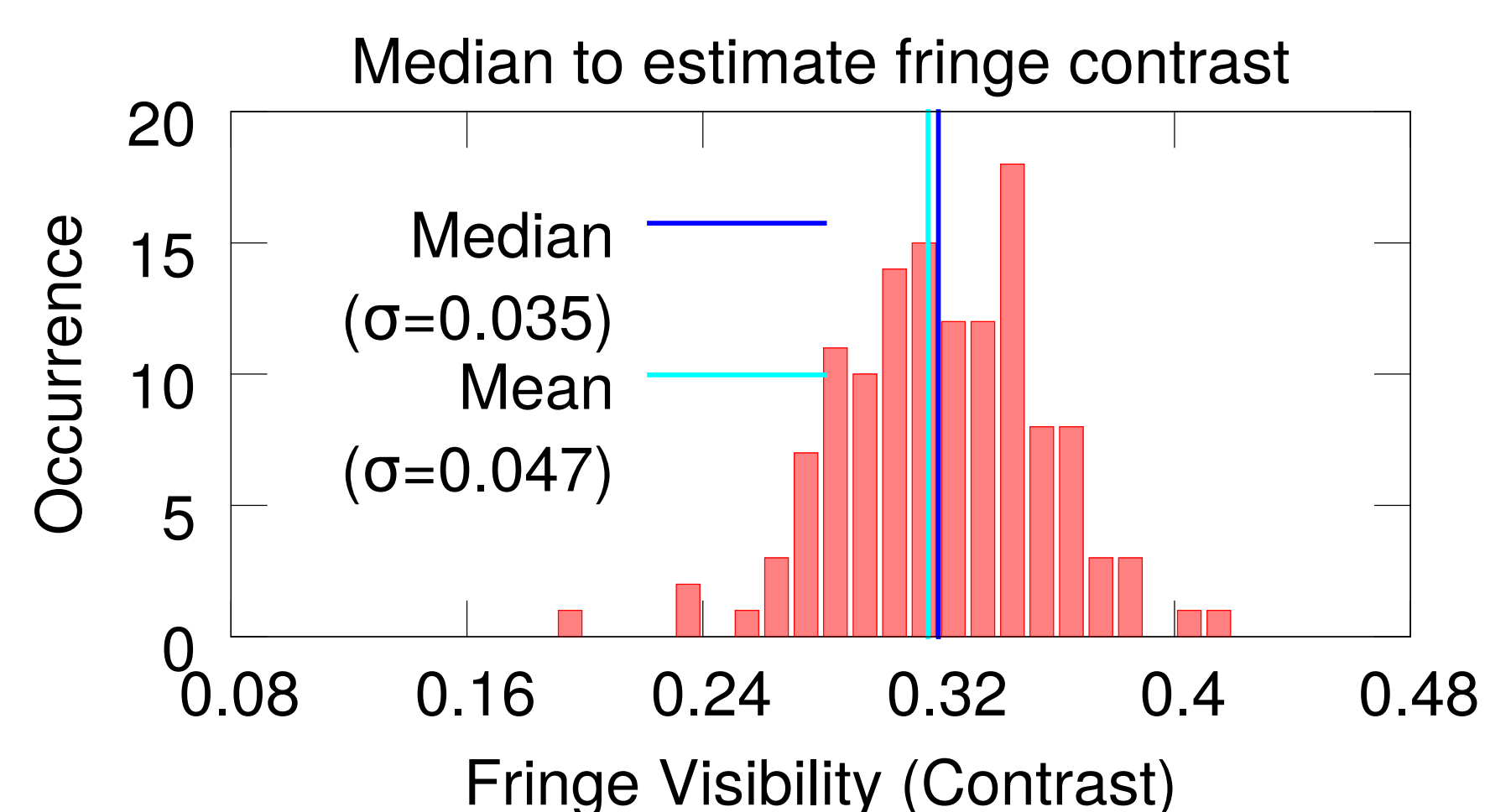


- We require very high angular resolution, attainable with optical long-baseline interferometry, which combines light between separate telescopes to form interference fringes.

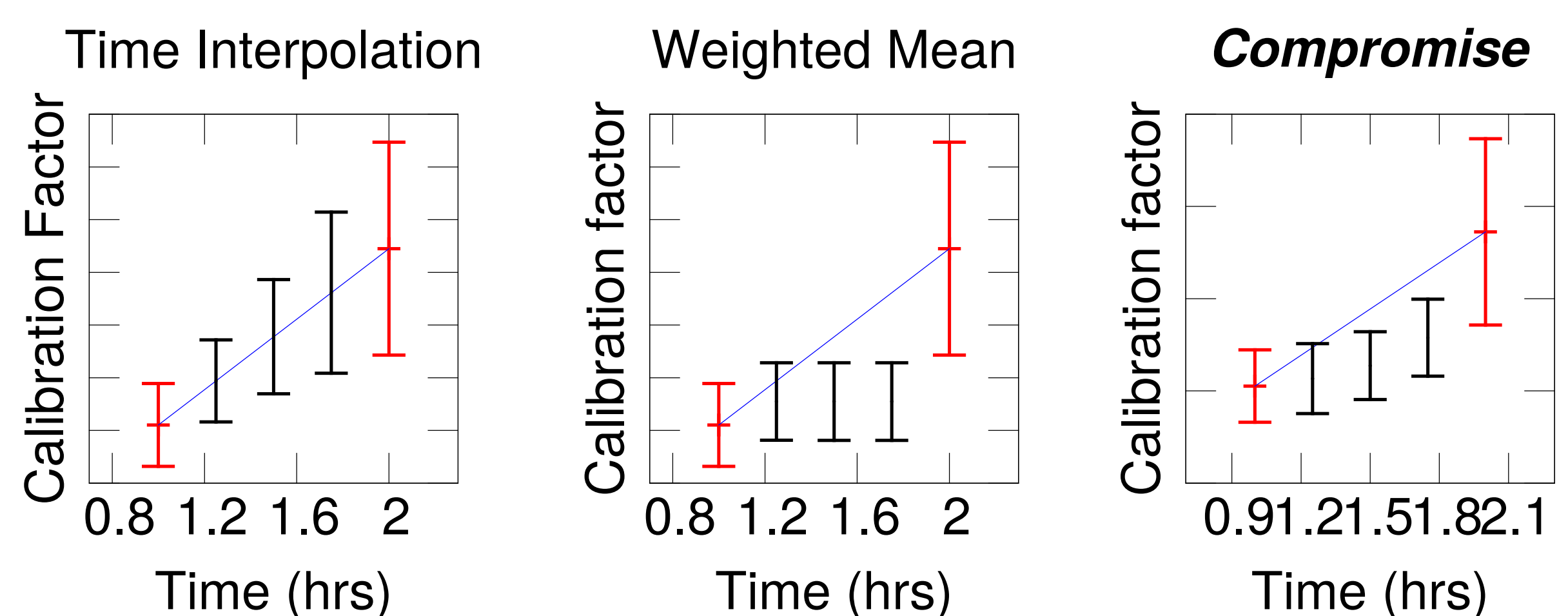
- The observational signature of faint ($\sim 1\%$) circumstellar excess light is a small ($\sim 1\%$) deficit in the fringe contrast compared to a non-excess star.



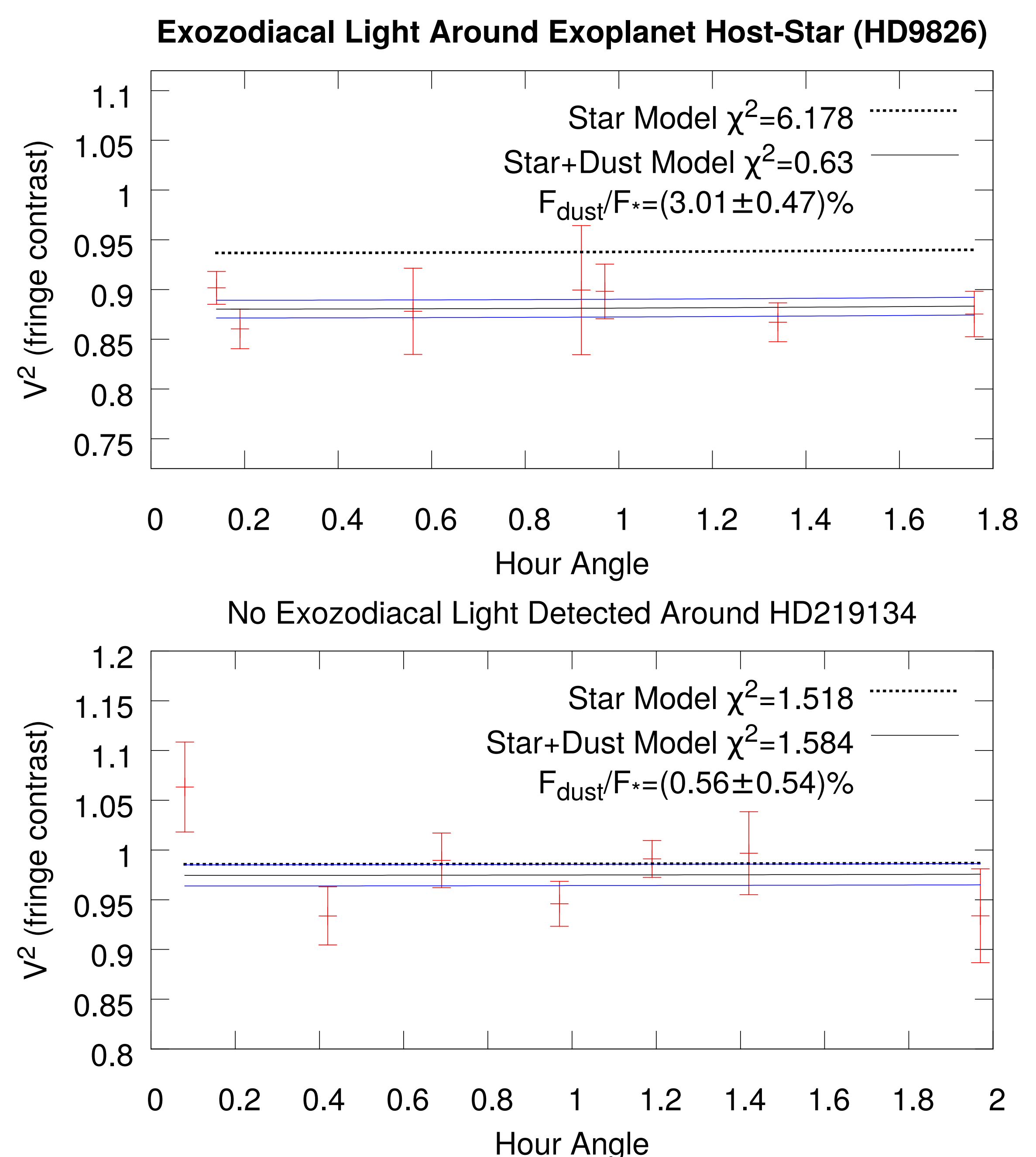
We have developed a Data Analysis Pipeline which minimizes statistical and calibration biases in the circumstellar excess estimation. For each observation we estimate the interference fringe contrast from an ensemble of fringe scans.



- We have shown that the median of the squared visibilities is an unbiased estimate of the squared (uncalibrated) visibility.
- Bootstrapping methods are used to calculate the uncertainties, making no assumptions about the statistics of the visibilities.
- We have improved the visibility calibration: we take into account the time variation as well as the uncertainty of each calibration observation (shown below in red).



Results (FY15): We have observed 55 targets, including 41 main sequence stars new to this program. We have analyzed data for 31 stars, and have **detected NIR circumstellar excesses for 7 stars** at the few percent level, 3 of which were previously unobserved or undetected. Below we show an example detection and an example non-detection.



A continuation of the ongoing survey may allow us to shed light on the poorly understood phenomenon of hot circumstellar dust, by searching for correlations with basic stellar characteristics and the existence of an outer-colder debris disk.

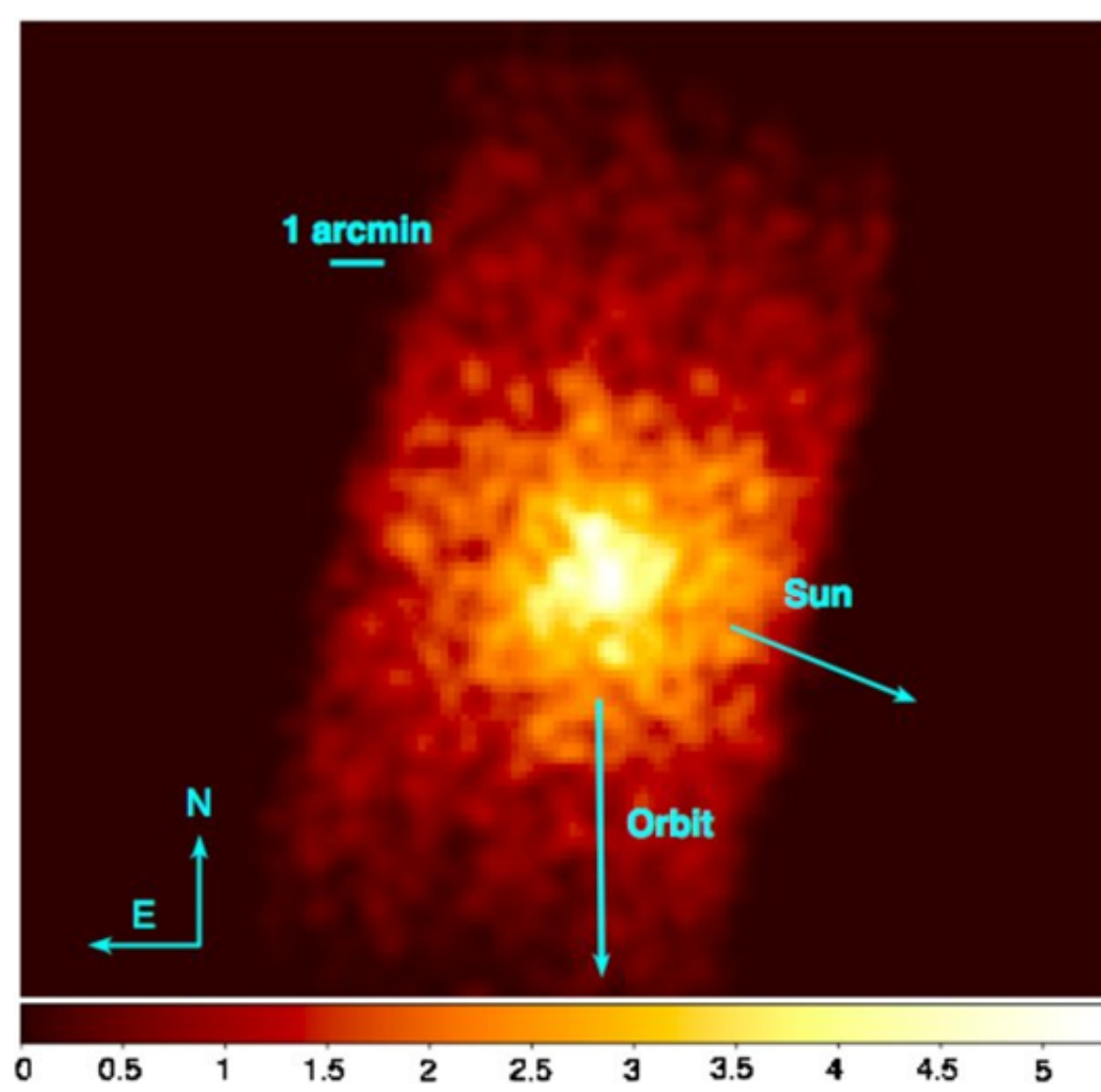
Measurement of Single and Multiple Charge Exchange for Highly-Charged Solar Wind Ions with Cometary and Planetary Gases

Principal Investigator: Ali Moradmand, Section 326

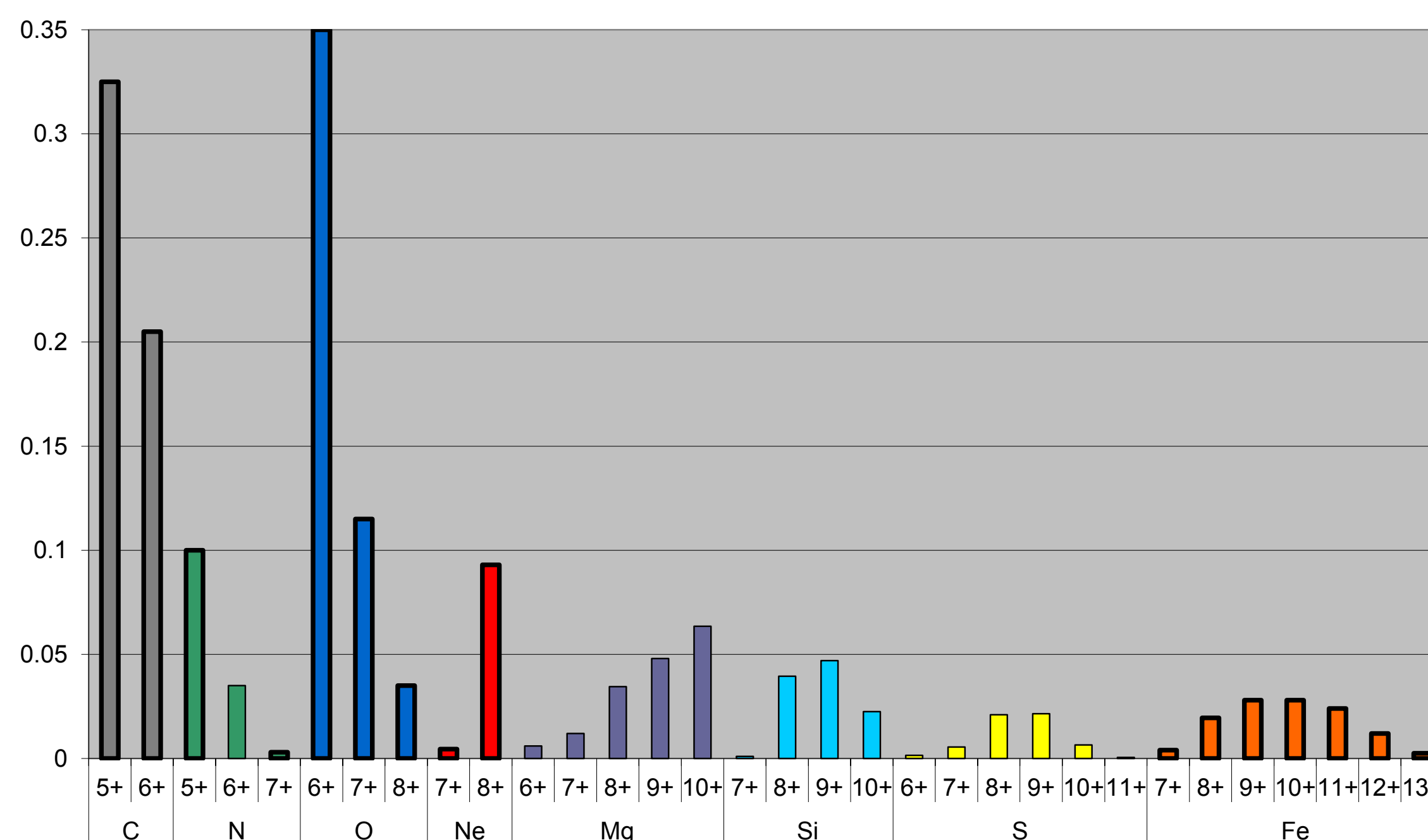
Ara Chutjian, Section 326

Introduction and Motivation

The charge exchange interaction between ions from the solar wind is responsible for X-ray emissions from cometary gases and planetary atmospheres. In order to better understand the expected and observed yields of photon emissions, our work focuses on the measurement of absolute cross sections for multiple charge exchanges using a highly-charged ion source with a retarding-potential analyzer. X-ray emissions are directly imaged using a grazing-incidence spectrometer and CCD camera in order to resolve the radiative transitions in the energy states populated via charge exchange. This work focuses on measurements involving the most abundant solar wind heavy ion, O^{6+} , with a number of neutral target gases found in comets and planetary atmospheres.

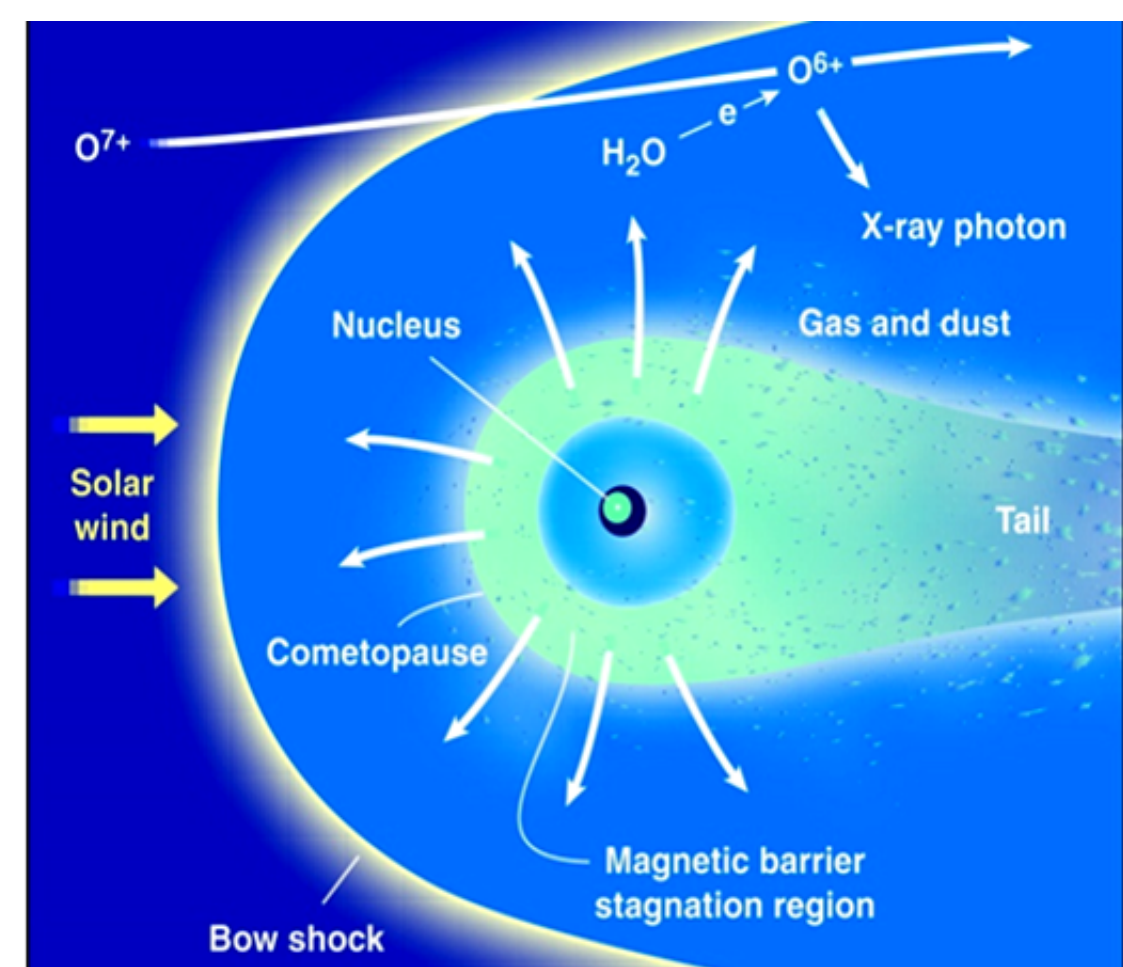


Chandra X-ray image of Comet 8P/Tuttle in the photon energy range 300-1000 eV (4.1-1.2 nm) (Christian et al. 2010).



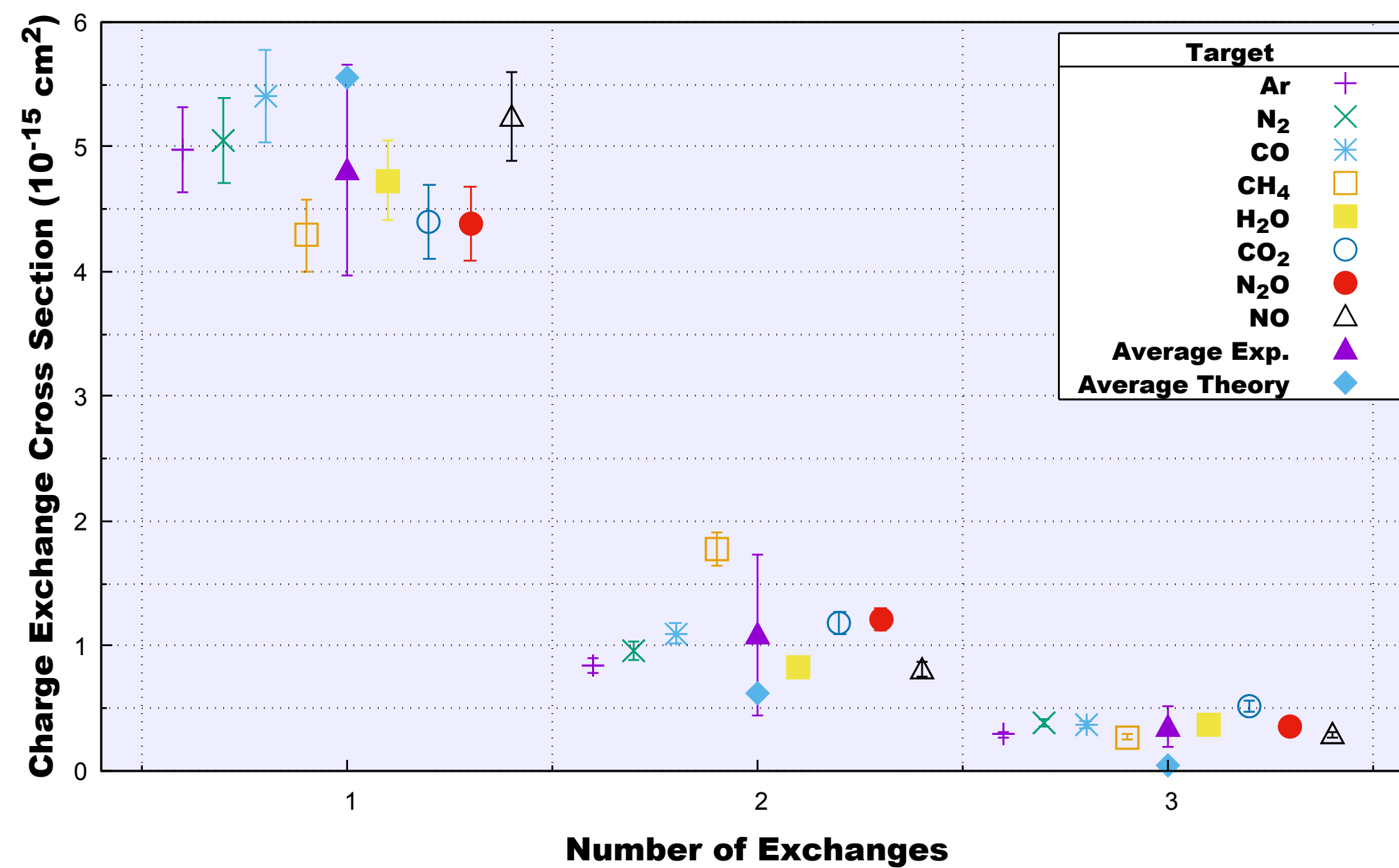
Average abundance of heavy ions in the solar wind. O^{6+} , the most abundant heavy ion, is the focus of this work. The solar wind is bimodal in speed, with a fast (~ 750 km/s) and a slow (~ 400 km/s) component. The present data show cross sections for both ion speeds, and X-ray spectra for the fast ions.

Diagram of the effect of the solar wind on gases surrounding a comet. The X-ray photon is produced by charge exchange which results in a radiative decay in the projectile ion.



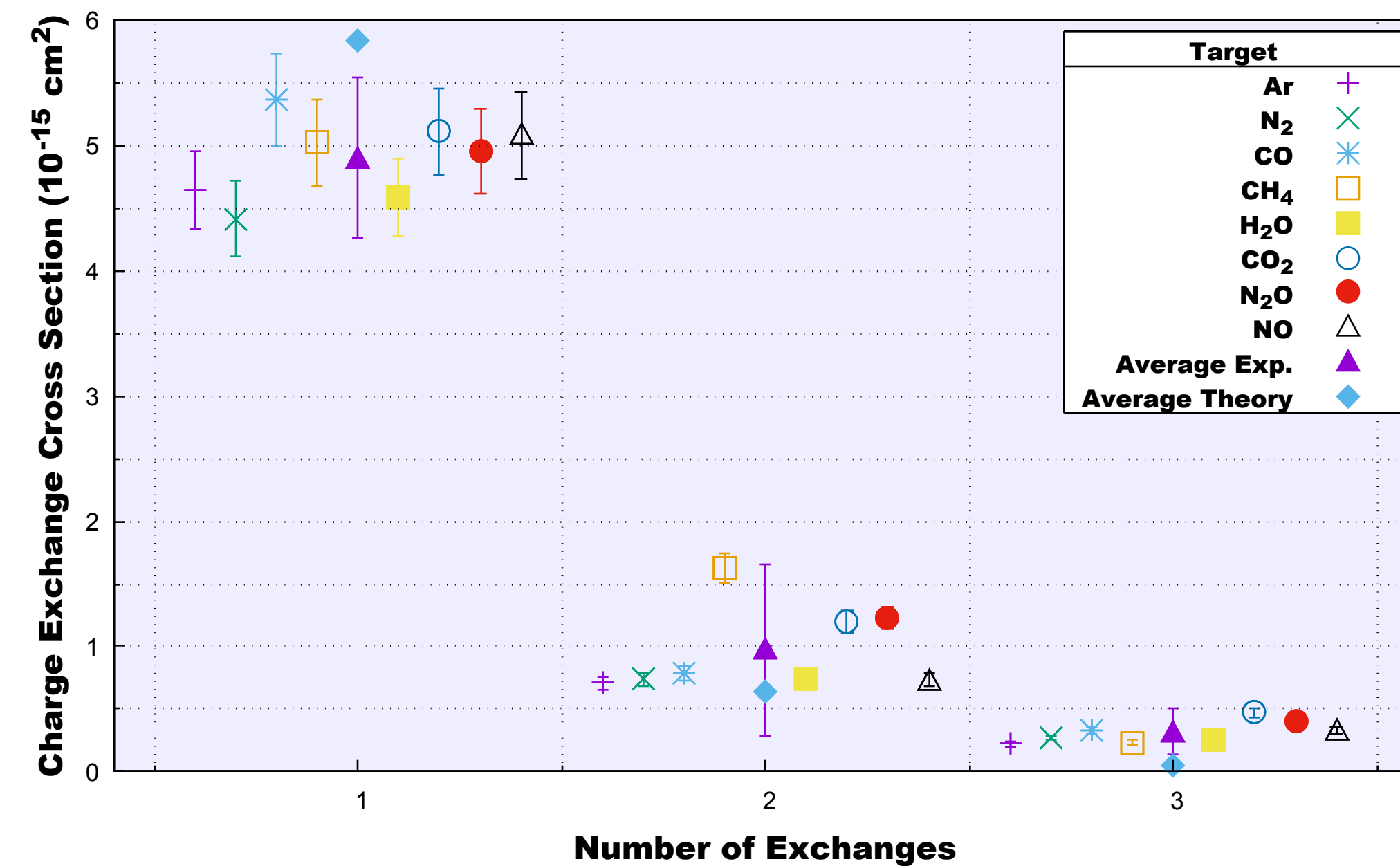
Charge Exchange Cross Section for O^{6+} on Neutral Gases

Slow Solar Wind



Charge Exchange Cross Section for O^{6+} on Neutral Gases

Fast Solar Wind



Present experimental data for charge exchange cross sections for fast (left) and slow (right) O^{6+} ions. Data are presented for individual gases, as well as an overall experimental average, and a theoretical average from present calculations. For the target gases presented, single, double, and triple charge exchange interactions were measured. Quadruple charge exchanges, while possible with the present targets, were below the detectable level, (Machacek, et al. 2015).

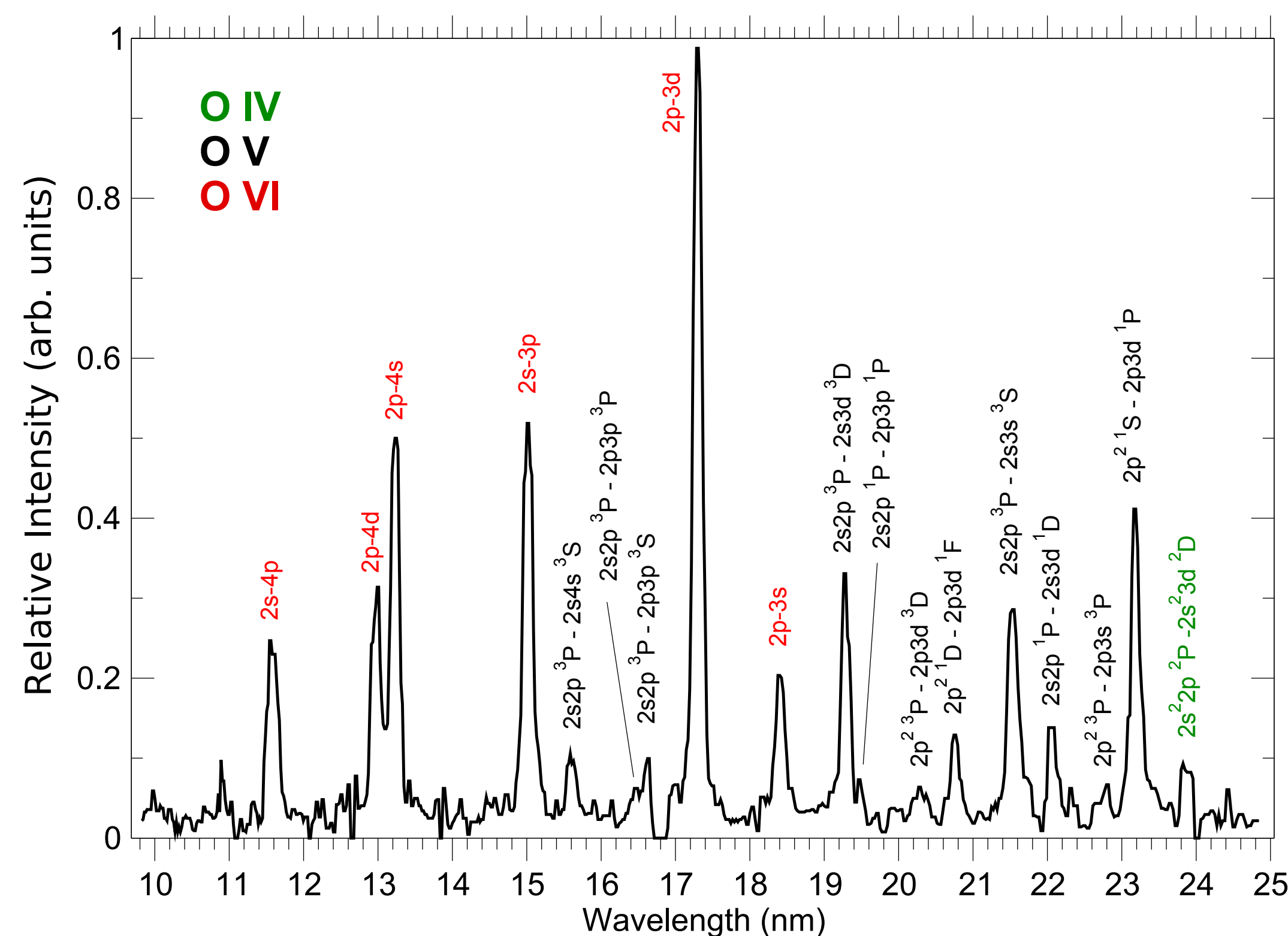
Right: Measured X-ray spectrum in the 10-25 nm wavelength region for fast (~ 750 km/s) O^{6+} ions on Ar gas. The O^{6+} ions are here accelerated with a 7 kV potential and introduced into a gas cell with Ar at ~ 2 mTorr.

The dominant lines are, as expected, from single charge exchange, resulting in transitions in O^{5+} (red, O VI).

Double charge exchanges are observed with singlet and triplet transitions in O^{4+} (black, O V).

The small line near 24 nm is due to a triple exchange to O^{3+} (green, O IV).

All lines are identified using the NIST Atomic Spectra Database.



Ongoing and Future Work

Charge exchange results not presented here include fast and slow ion measurements for Si^{7-10+} with target gases He and H_2 , along with theoretical calculations for those systems

X-Ray measurements are being prepared for O^{6+} for the remaining molecular targets N_2 , CO, CH_4 , H_2O , CO_2 , N_2O , and NO, as well as X-ray spectra in the longer wavelength range ($\sim 40-60$ nm) to supplement the present data

Upcoming charge exchange cross section measurements will focus on the lower-abundance solar wind constituent ions, including Ne, Mg, S, etc.

Rest-frame Optical Spectra and Black Hole Masses of $3 < z < 6$ Quasars

Hyunsung Jun (JPL, 3266), and AKARI QSONG team

Introduction

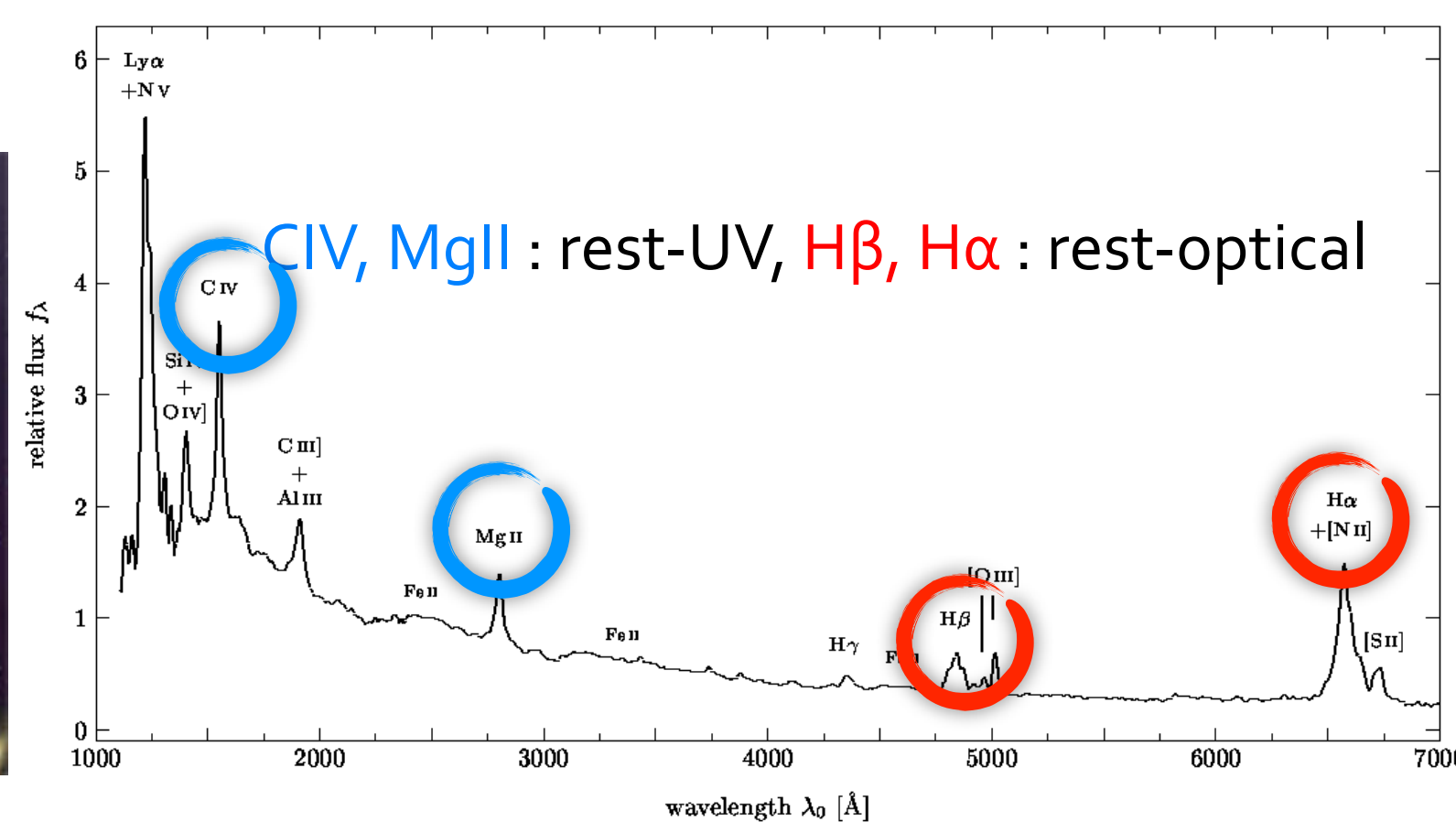
- Quasars (quasi-stellar radio objects) are luminous active galactic nuclei, powered by accreting supermassive black holes (BHs)
- The BH masses of quasars measured from broad emission line kinematics, tell us about their growth history and co-evolution with their host galaxies
- The virial BH mass estimators, e.g., $M_{\text{BH}} = \frac{f}{G} R_{\text{BLR}} (L_{5100}) \left(\frac{\text{FWHM}_{\text{H}\beta}}{2} \right)^2$ from various emission lines are not well calibrated with each other, especially in the distant universe (=high redshift)



Quasars zoomed in (left) and out (right), credit: NASA JPL/Caltech

Objective & Observations

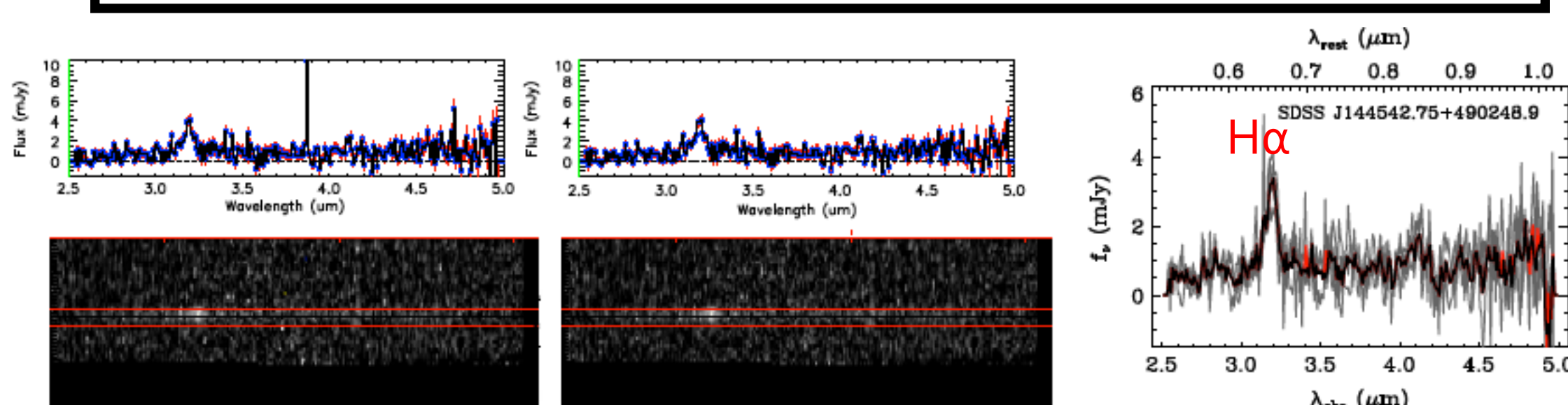
- Using the rest-frame optical spectro-photometric observations of distant quasars, we aim to
 - calibrate a set of rest-frame UV to optical BH mass estimation recipes to check for consistency
 - probe the massive end BH masses at high redshift to understand their mass evolution



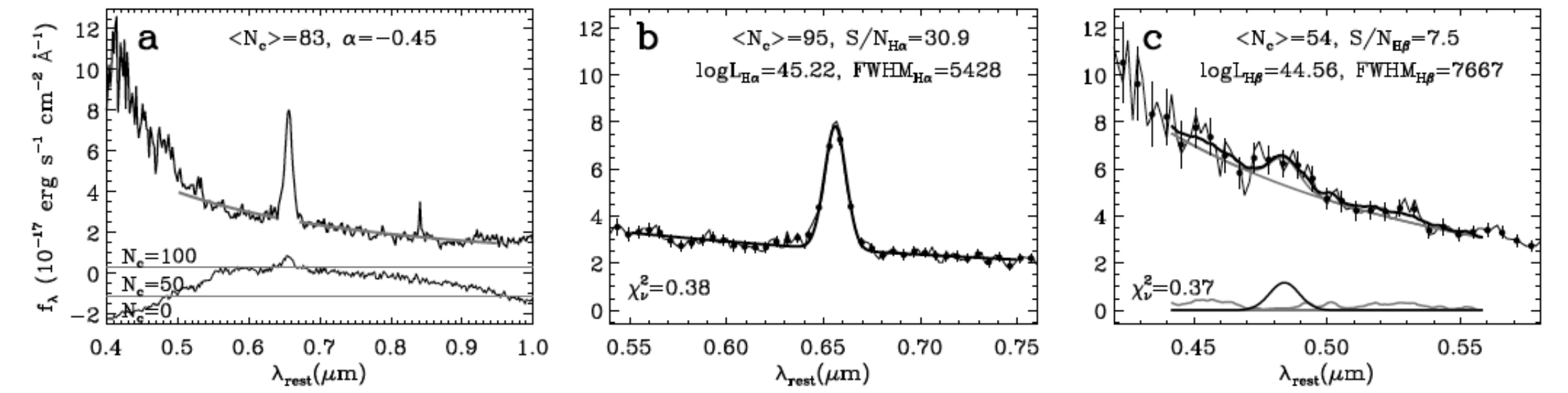
AKARI space telescope (left), typical quasar spectrum (right)

- QSONG (Quasar Spectroscopic Observation with NIR Grism) is an AKARI (明かり) space mission program to obtain 2.5-5.0 micron quasar spectra
- 155 luminous ($L_{\text{bol}} > 10^{47}$ ergs/s) quasars with existing rest-UV spectra, redshift range $3.3 < z < 6.4$ to catch $\text{H}\alpha$ emission

Data analysis

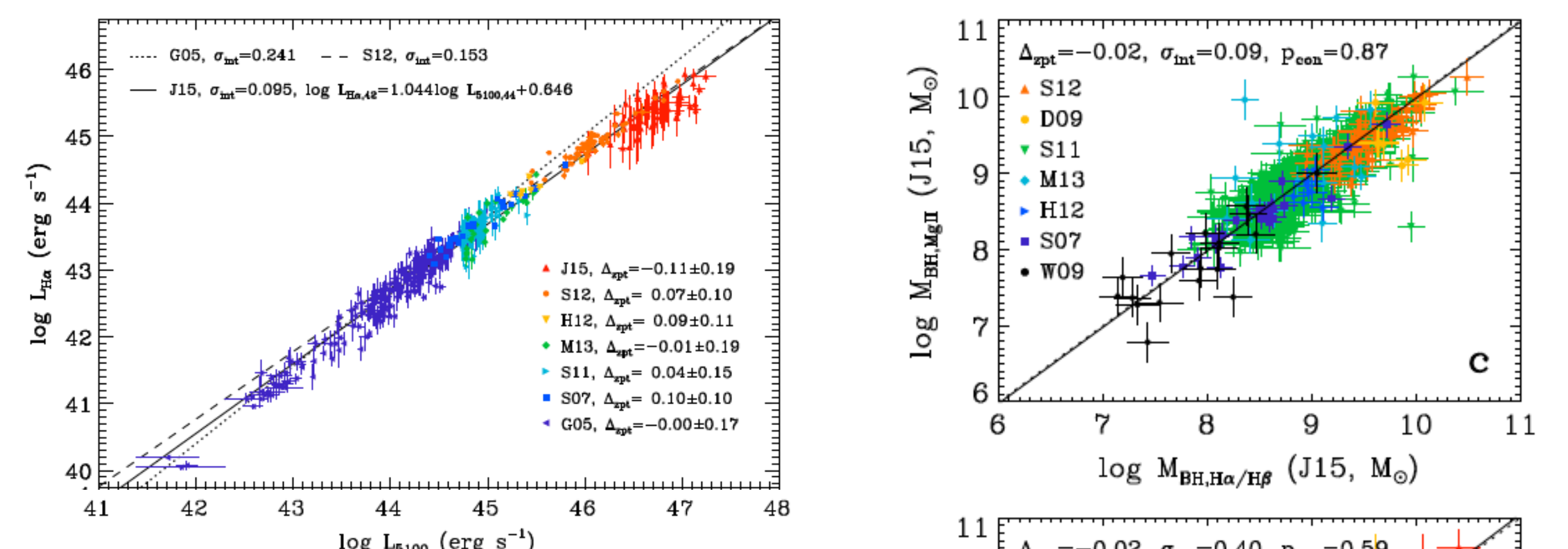


- Data reduction: AKARI pipeline processed spectrum (left), hot pixels rejected (middle), multiple pointings of data stacked with sigma clipping (right)

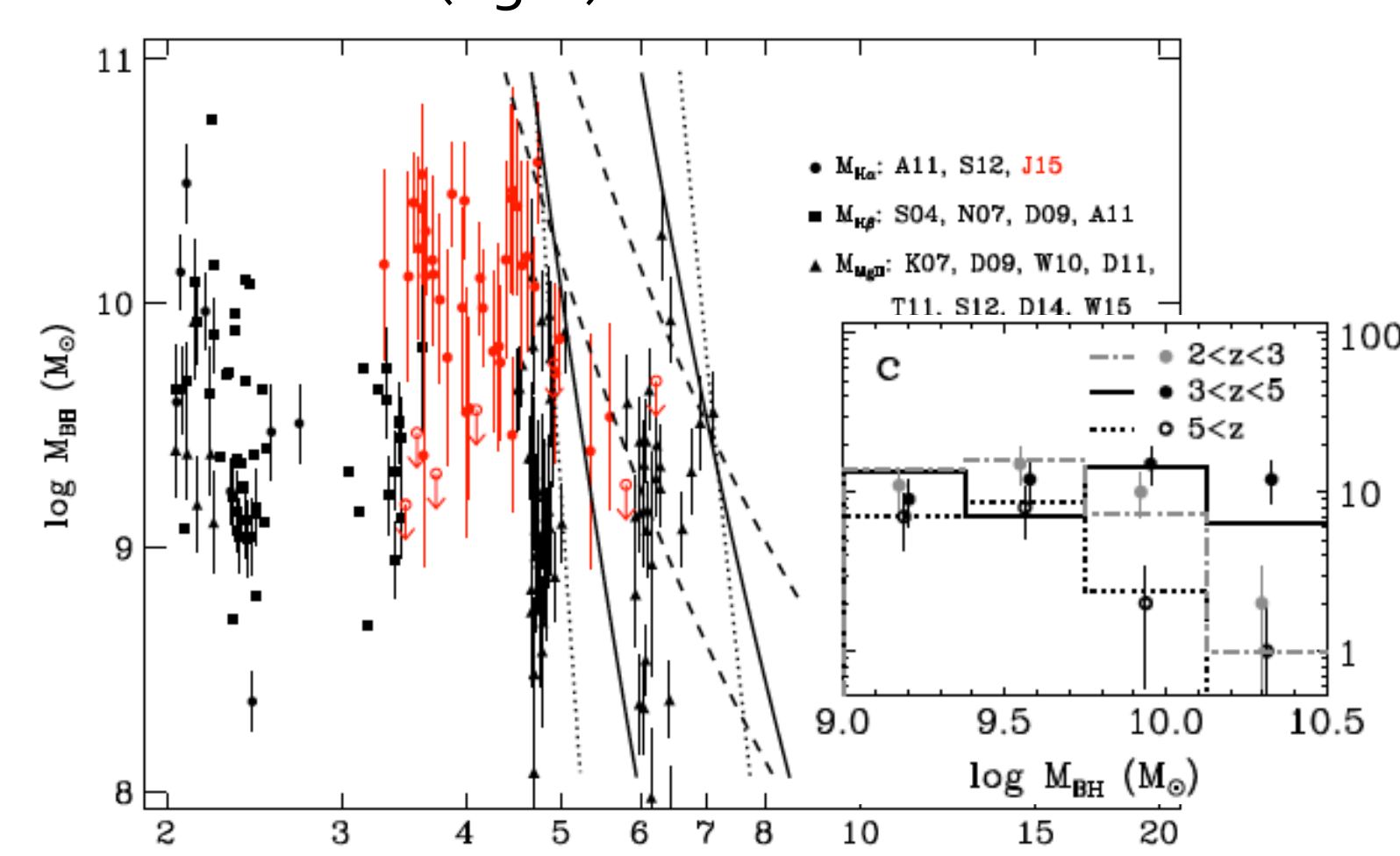


- Analysis: composite spectrum (left), $\text{H}\alpha$ region fit (middle), $\text{H}\beta$ region fit (right). 43 BH mass estimates from $\text{H}\alpha$ ($S/N > 3$) spectra are obtained from line width and continuum luminosity measurements, simulated to be robust under low sensitivity and spectral resolution ($R=120$).

Results & Discussion



- $L(5100)$ - $L(\text{H}\alpha)$ relation holds as a linear function over a wide range of luminosity/redshift (left), supporting that broad line kinematics are still useful to measure BH masses for luminous, distant quasars (red)
- $\text{H}\alpha/\text{H}\beta$ BH masses are consistent with MgII masses up to 0.09 dex intrinsic scatter, but shows 0.40 dex scatter with CIV (right)



- The $\text{H}\alpha/\text{H}\beta/\text{MgII}$ BH masses including the AKARI data (left, red) show a steep decline in the number of the most massive BHs beyond $z=5$, with the $z < 5$ and $z > 5$ distribution at $> 2 \times 10^9$ solar masses indistinguishable by only a 0.3% K-S probability. The luminosity selection corrected BH mass counts (right, lines) support the drop of $z > 5$, 10 billion solar mass BHs

Conclusion

Through the AKARI rest-optical spectroscopy of distant, luminous quasars we find that

- $\text{H}\alpha/\text{H}\beta/\text{MgII}$ BH masses are consistent with each other, and indicate that the bulk of the most massive BH growth have occurred at $z > 5$
- Constraints are given on the earliest assembly (seed mass, radiation efficiency) of the most massive BHs, but also on the BH-galaxy coevolution as the BHs may have finished their growth before the most massive galaxies do at $z < 3$
- Acknowledgement: This research was supported by an appointment to the NASA Postdoctoral Program at the Jet Propulsion Laboratory, administered by Oak Ridge Associated Universities through a contract with NASA

Herschel Galactic plane survey of ionized gas traced by [NII]

Principal Investigator: Umut Yildiz (3266)

Paul Goldsmith (3266), William Langer (3200), Jorge Pineda (3266)

Motivation

- Far infrared and sub-/millimeter atomic & ionic fine structure and molecular rotational lines are **powerful tracers of star formation**.
- Although CO lines trace cool to moderately warm molecular gas, ionized carbon [CII] produces the strongest lines, which arise from almost all warm ($T > 35$ K) parts of the ISM. However [CII] alone cannot distinguish fully ionized gas from weakly ionized gas.
- [NII] plays a significant role in star formation as it is **produced only in ionized regions**; in HII regions as well as diffuse ionized gas. The ionization potential of nitrogen (14.5 eV) is greater than that of hydrogen (13.6 eV), and carbon (11.3 eV), therefore the ionized nitrogen [NII] lines reflect the effects of massive stars, with possible enhancement from X-ray and shock heating from the surroundings.
- It is important to quantify what fraction of [CII] emission arises in the ionized gas, to resolve the different parts of the ISM, leading to determine the total mass of the ISM.*

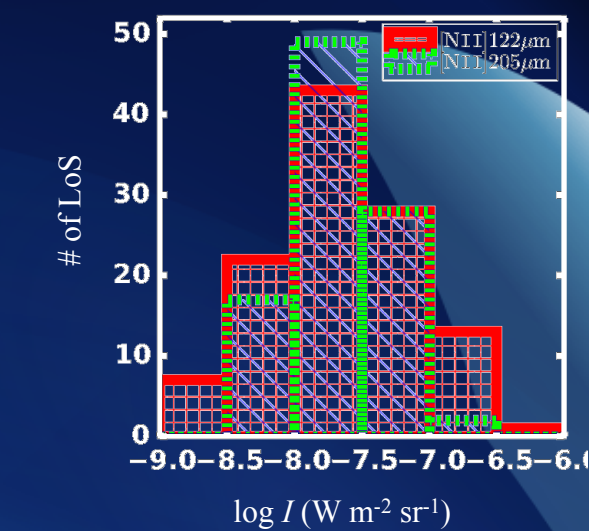
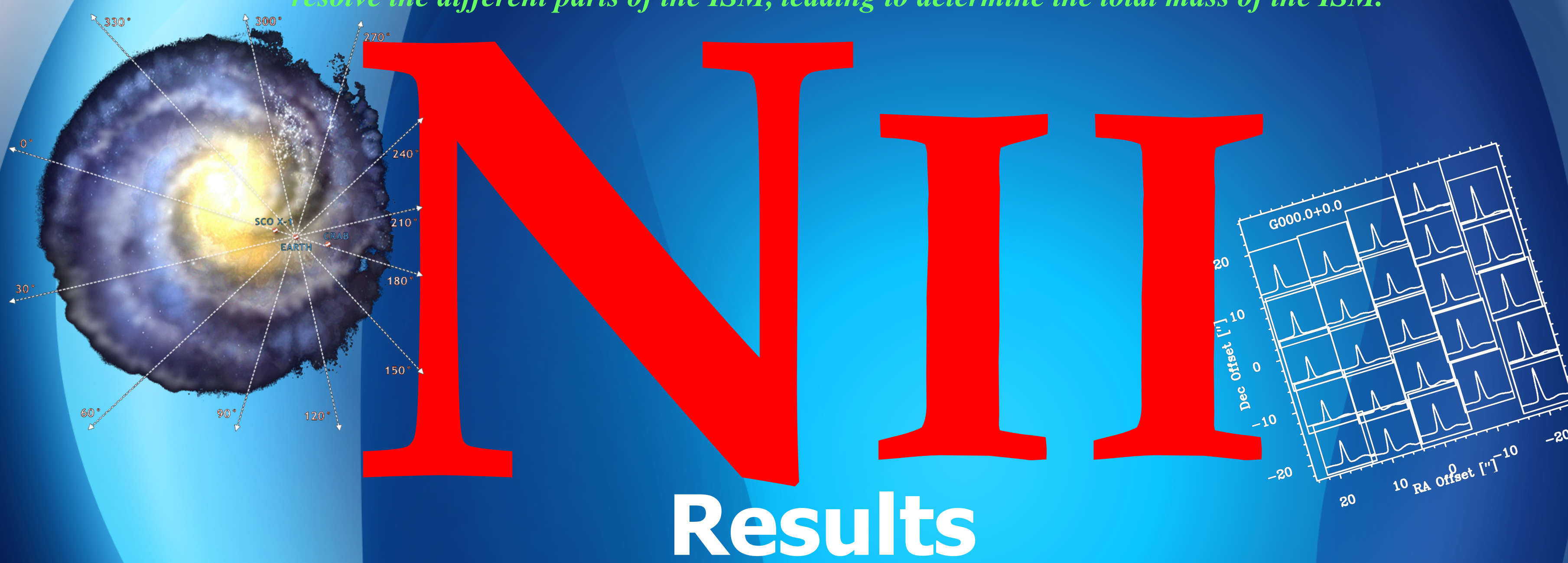


Fig 1: Histogram of intensities



Results

- [NII] has two fine structure transitions at 122 and 205 μm . The two lines can be used to calculate the electron density and column density of N^+ , if one assumes that the emission from both transitions originate in the same gas and under roughly uniform conditions.

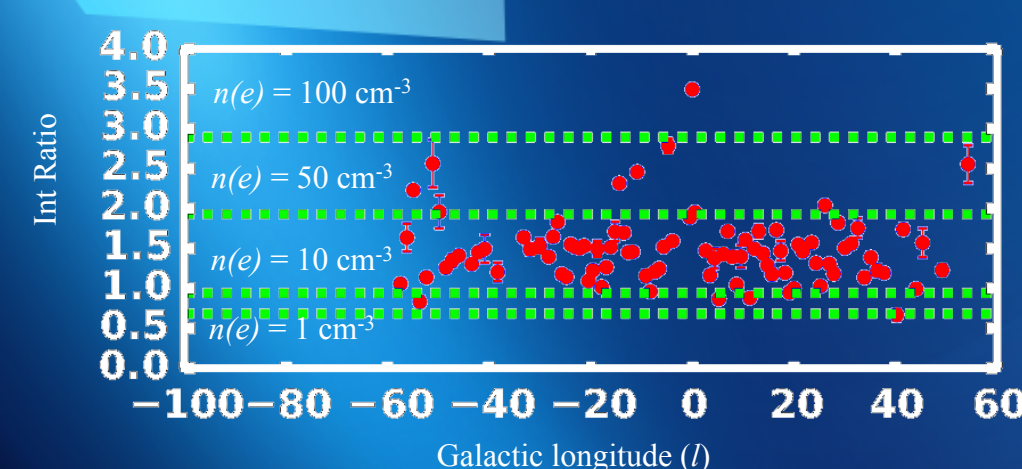


Fig 2: Electron densities are shown as function of the position in the Galactic Plane

- [NII] detections are mainly toward the Galactic center. [NII] electron densities are found to be between 10 to 50 cm^{-3} (Fig. 2) and N^+ column densities range between 10^{16} to 10^{17} cm^{-2} .

- [NII] emission is highly correlated with that of [CII], implying that between 1/3 and 1/2 of the [CII] emission arises in the ionized gas.

- High densities indicate that the source of the emission is not the WIM (Warm Ionized Medium), which has densities 10-100 times smaller.

- Possible origin of the observed [NII] include the ionized surfaces of dense atomic and molecular clouds, the extended low density envelopes of HII regions, and low-filling factor high-density fluctuations of the WIM.*

Methods

- Two far-infrared 122 μm and 205 μm [NII] fine structure spectral lines are observed via Photodetector Array Camera and Spectrometer (PACS) onboard *Herschel* Space Observatory.

- The sample consists of 149 lines-of-sight (LoS) positions in the Galactic plane, following those of the [CII] 158 μm observations obtained with the GOT C+ survey.

- PACS data have 5x5 spatial pixels therefore all 25 spectra are averaged to improve S/N , and that led to increase the number of detections in the averaged spectra.

- The pixel to pixel variation of the emission within a single *Herschel* pointing is relatively small, which is interpreted as the [NII] emission comes from an extended gas.

- [NII] detections are mainly toward the Galactic center (intensity distribution shown in Fig. 1), but the opposite side of the Galactic center gives upper limits of $\sim 4 \times 10^{-10} \text{ W/m}^2/\text{sr}$ for the 122 μm line and $\sim 2 \times 10^{-9} \text{ W/m}^2/\text{sr}$ for the 205 μm line (Fig. 3).

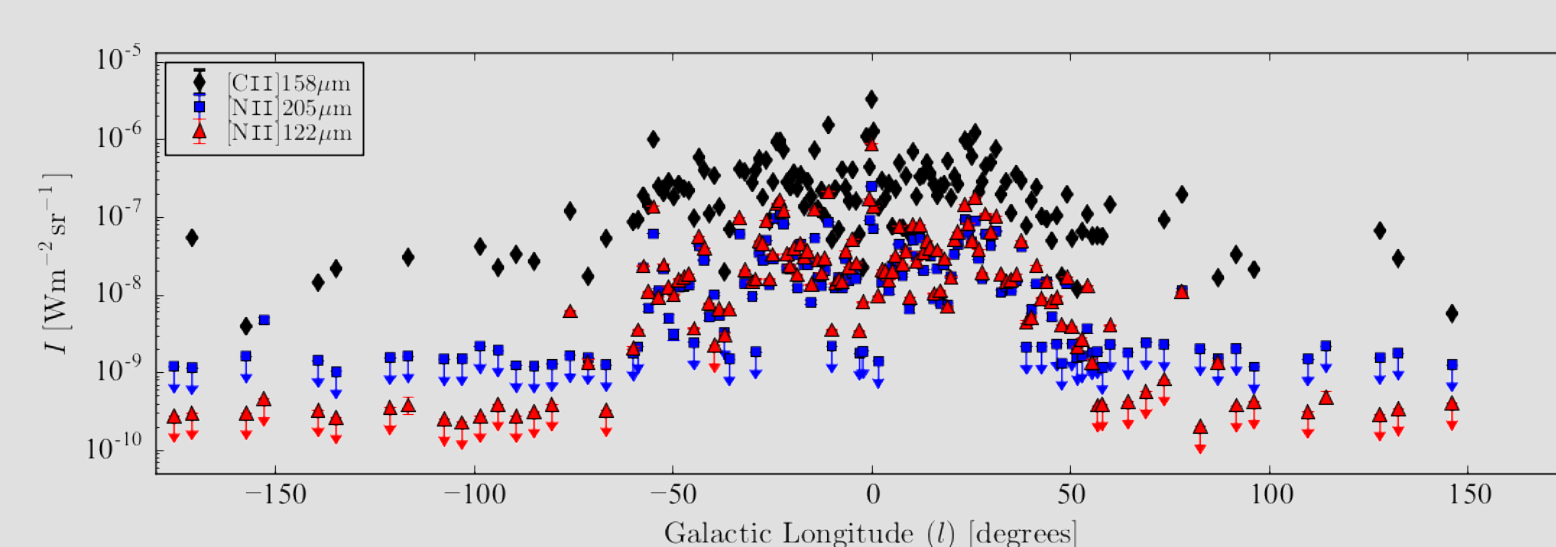


Fig 3: Position vs. intensities of [NII] and [CII] are shown through the Galactic plane.

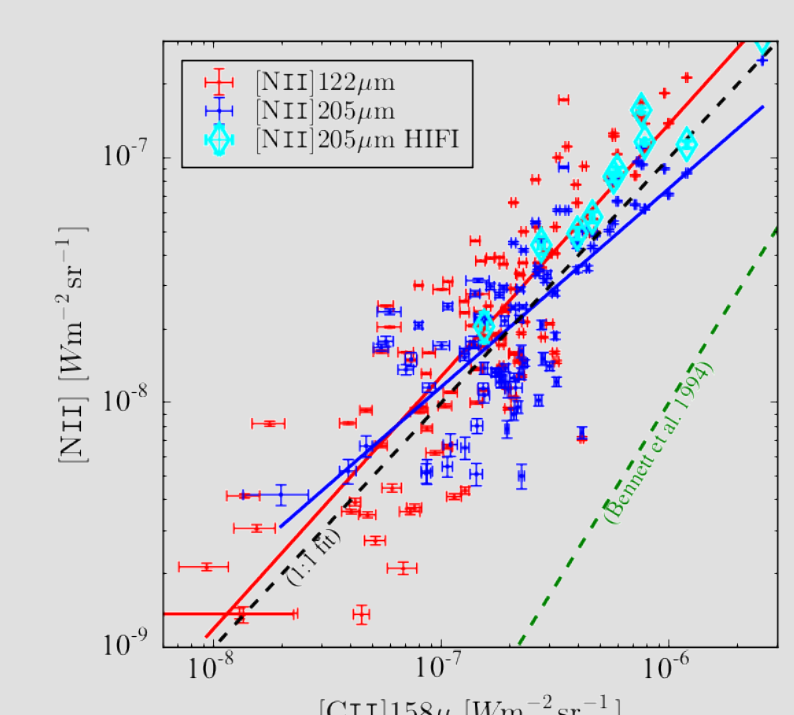


Fig 4: [NII] vs [CII] intensities shows tight correlation.

- [CII] is the most important coolant of atomic hydrogen clouds and the photon dominated regions (PDRs) of molecular clouds and is widely used as a tracer of star formation. We found that [NII] measured with HIFI as well as PACS are linearly correlated with the [CII] emission.

Black Hole Spin: Beyond the Local Universe

Principal Investigator: Dominic Walton (JPL: section 3266)

M. T. Reynolds, J. M. Miller (U. Mich), F. A. Harrison (Caltech), D. Stern (JPL: section 3266)

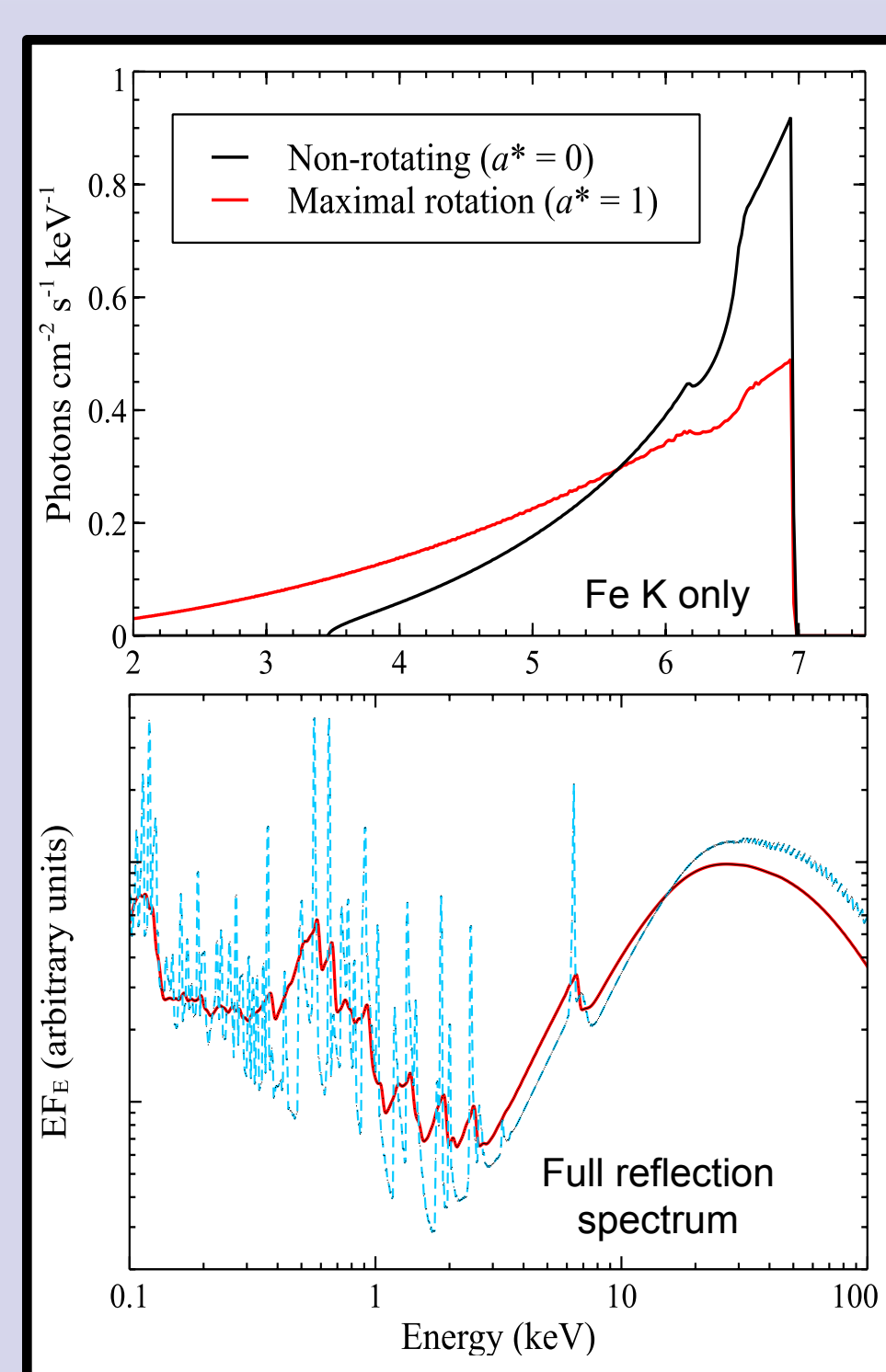
Black Hole Spin

Astrophysical black holes are fully characterised by their mass M and their angular momentum J (typically characterised as a dimensionless 'spin': $a^* = Jc/GM^2$, normalized such that $-1 < a^* < 1$). While we have been measuring masses for decades, black hole spin measurement is a comparatively new field. Nevertheless, it has quickly become a very active area of high-energy astrophysics, as the knowledge of black hole spin has a variety of important applications across several key areas of current research, including the growth of the supermassive black holes (SMBHs) that power active galactic nuclei (AGN; e.g. Berti & Volonteri 2008), launching mechanisms for relativistic jets (Blandford & Znajek 1977), and supernovae (Miller, Miller & Reynolds 2011).

Relativistic Disk Reflection

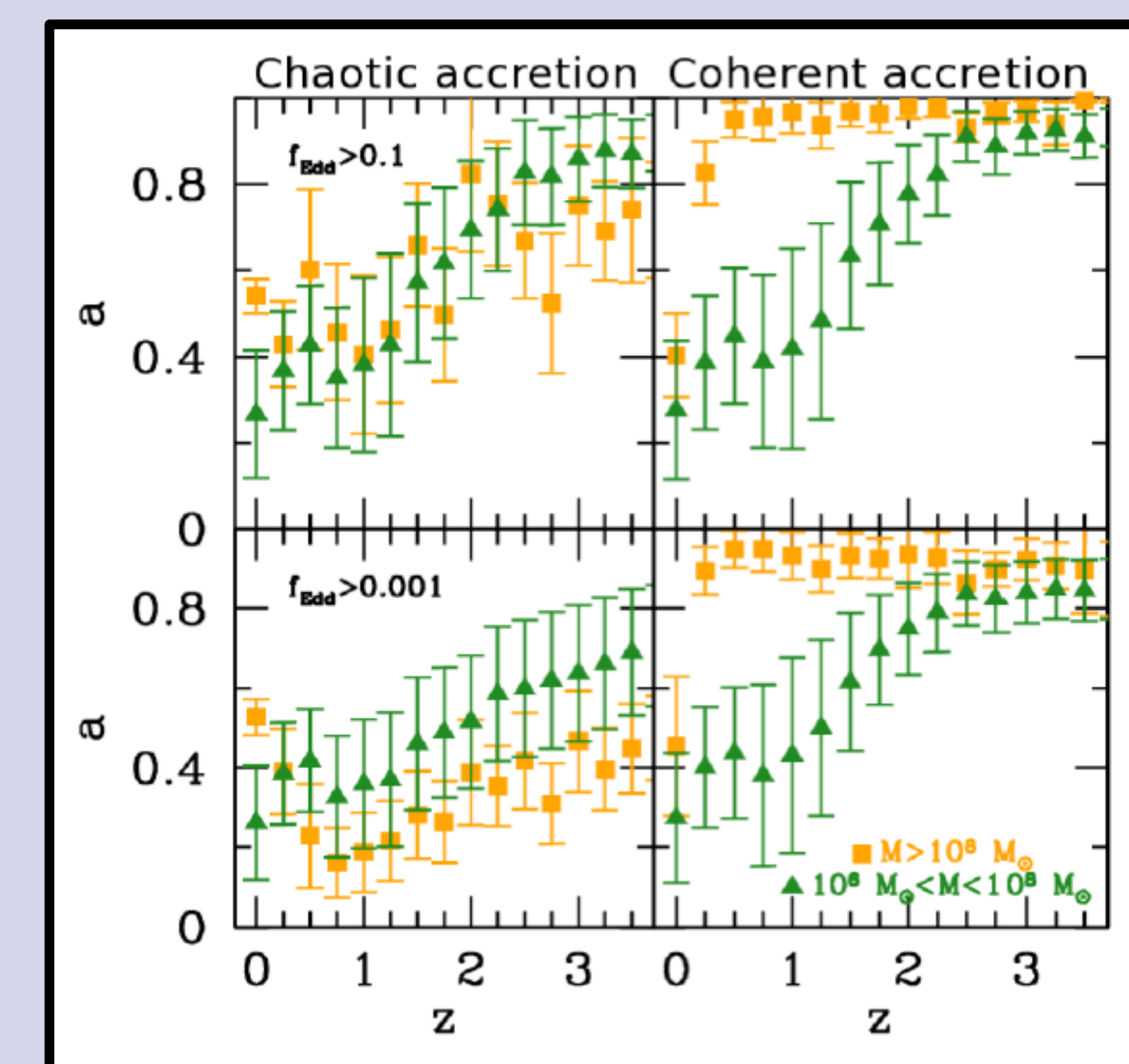
AGN spin measurement is anchored in X-ray spectroscopy. At sufficient rates in infall, material primarily accretes onto a black hole through an accretion disk (Shakura & Sunyaev 1973). Spin measurements involve measuring the relativistic distortions experienced by the 'reflected' emission from the inner accretion disk, produced when the surface of the disk is irradiated by X-rays.

The reprocessed emission spectrum contains fluorescent line emission, typically dominated by the iron K α line at 6.4 keV (e.g. George & Fabian 1991). Relativistic effects associated with the regions of strong gravity close to a black hole (e.g. gravitational redshift, etc.) broaden and skew intrinsically narrow emission lines into a characteristic 'diskline' profile (e.g. Fabian et al. 1989; *right*), which depends on black hole spin.



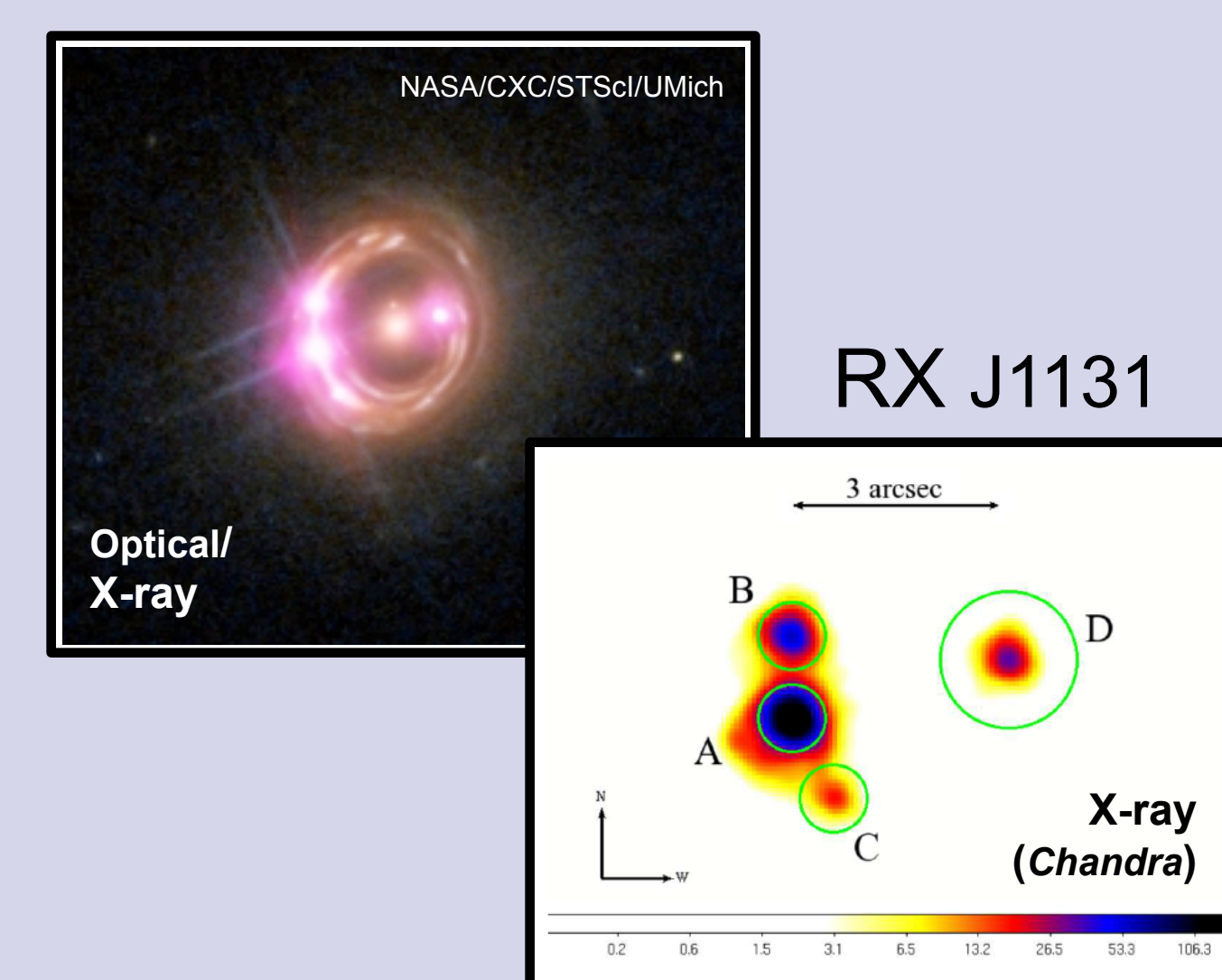
Supermassive Black Hole Growth

The growth history of SMBHs is encoded in their spin. Growth through a series of **chaotic** mergers should result in **spin down**, while growth through prolonged episodes of **coherent** (common angular momentum axis) accretion will result in **spin up**. These different scenarios make different predictions for the redshift evolution of the average SMBH spin (e.g. Volonteri et al. 2013; *right*). Testing these models requires knowledge of the SMBH spin distribution as a function of redshift, out to and beyond the observed peak of AGN activity ($z \sim 2$; Richards et al. 2006), and is one of the main goals of the 2028 *Athena* X-ray observatory.



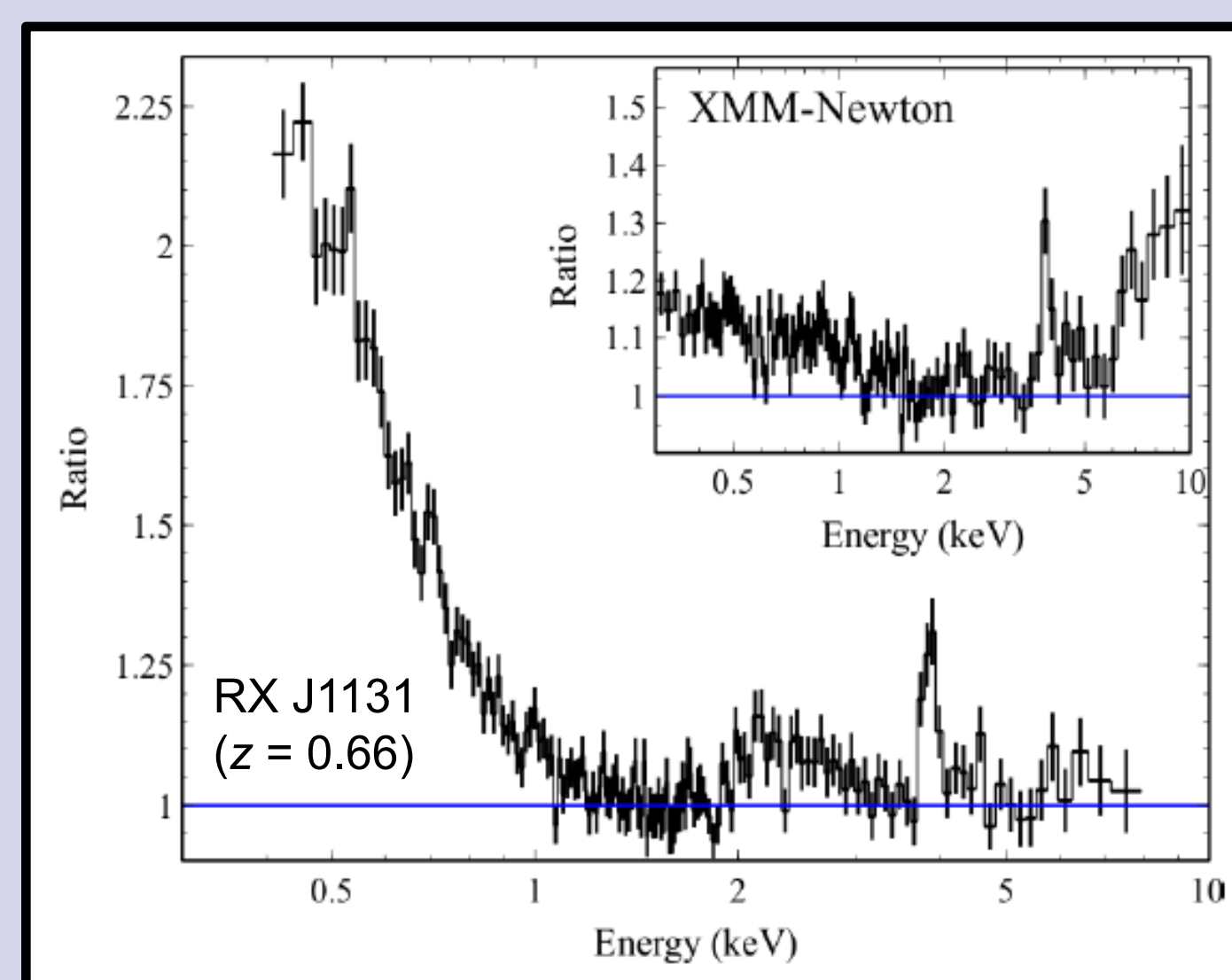
Lensed Quasars

For typical high-redshift AGN, our current X-ray observatories do not have sufficient sensitivity to provide the signal-to-noise (S/N) required for spin measurements. Recently, however, we have demonstrated that strongly lensed quasars (e.g. RX J1131, *right*) offer a rare opportunity to obtain spin measurements from objects at cosmologically interesting redshifts **with current instrumentation**, owing to the combination of the multiple images observed and the amplification of the intrinsic emission by the lens.



RX J1131 and Q 2237

Building on the work robustly demonstrating the relativistic disk reflection paradigm in the local universe (e.g. Risaliti et al. 2013, Walton et al. 2014), we found two high-redshift lensed quasars with sufficient S/N in the archive to reveal relativistic disk reflection signatures: RX J1131 ($z = 0.66$, Reis et al. 2014) and Q 2237 (aka 'the Einstein Cross', $z = 1.7$; Reynolds et al. 2014). Both show broadened iron emission with strong gravitational redshifts (*right* – reflection features from RX J1131, shown as a ratio to the intrinsic AGN continuum; *below* – the full reflection model fit to Q 2237).



By analysing these features with the latest disk reflection models, we have been able to provide the first direct SMBH spin constraints for sources beyond the local universe. Both sources are found to host rapidly rotating black holes:

$$\text{RX J1131: } a^* = 0.87^{+0.02}_{-0.12}$$

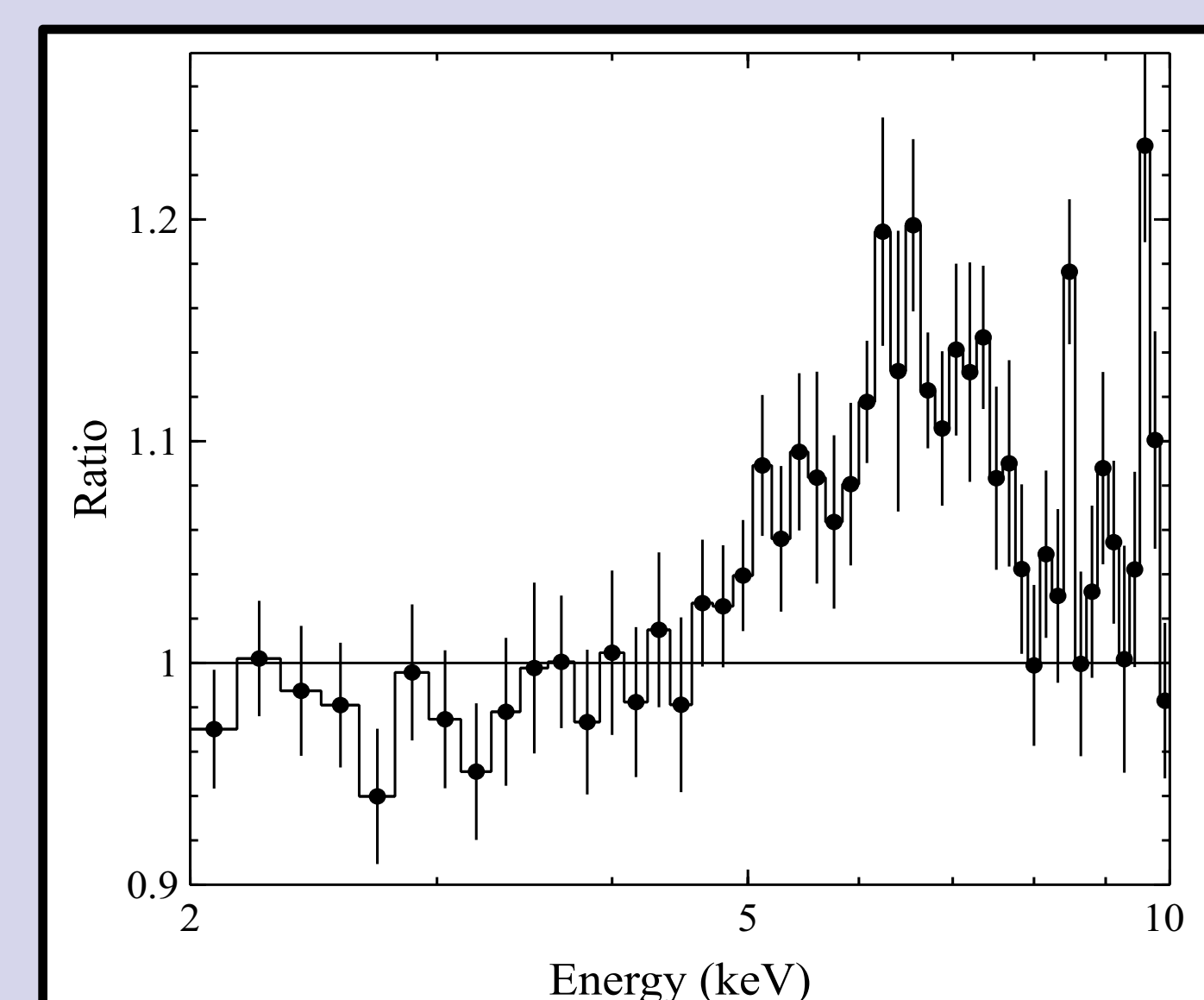
$$\text{Q 2237: } a^* = 0.74^{+0.06}_{-0.03}$$

This would imply that both these black holes grew primarily through coherent episodes of accretion, rather than through a chaotic series of mergers.

Lensed QSO Sample

Over the course of its lifetime so far, the *Chandra* X-ray observatory has been undertaking a major program observing lensed quasars in order to study variability between the different quasar images. *Chandra* is the only X-ray observatory with the imaging capabilities to resolve these images. This has naturally resulted in a large sample of lensed QSOs with X-ray coverage (in addition to RX J1131 and Q 2237). To extend our work on RX J1131 and Q 2237, we compiled a sample of 27 additional lensed quasars over the redshift range $1.0 < z < 4.5$ with *Chandra* observations. Unfortunately the rest of this sample do not currently have sufficient archival S/N in to search for relativistic reflection signatures individually.

However, by combining residuals to the continuum in the iron emission band across the rest of the sample, we were able to again detect relativistically broadened iron emission (Walton et al. 2015; *right*). Although the combined line profile still does not have sufficient S/N to provide an average spin estimate for the sample, this detection further demonstrates the potential of this population for such work.



Conclusions

Knowledge of the SMBH spin distribution as a function of redshift offers a window into the growth history of these objects. However, for typical AGN beyond the local universe, current X-ray instrumentation do not have the sensitivity required to undertake spin measurements, and the next-gen *Athena* X-ray observatory will be required. Here, we have demonstrated that strongly lensed quasars offer a means to obtain high-redshift ($z > 0.5$) SMBH spin measurements via their relativistic disk reflection spectra with current instrumentation. We have already measured the spin of two such sources, RX J1131 ($z = 0.66$) and Q 2237 ($z = 1.7$), finding that both host rapidly rotating black holes, and therefore likely grew primarily through coherent accretion episodes. We also detect relativistically broadened iron emission from a sample of 27 additional lensed QSO sample observed by *Chandra*, indicating this is common among the lensed quasar population, and that additional measurements should be possible with further observations. This opens up the possibility of constructing a pilot sample of high-redshift SMBH spin measurements prior to the launch of *Athena*.

References:

- Berti, E. & Volonteri, M., 2008, ApJ, 684, 822
- Blandford, R. D. & Znajek, R. L., 1977, MNRAS, 179, 433
- Fabian, A. C., et al., 1989, MNRAS, 238, 729
- George, I. M. & Fabian, A. C., 1991, MNRAS, 249, 352
- Miller, J. M., Miller, M. C. & Reynolds, C. S., 2011, ApJ, 731, 5
- Reis, R. C., Reynolds, M. T., Miller, J. M., Walton, D. J., 2014, Nature, 507, 207
- Reynolds, M. T., Walton, D. J., Miller, J. M., Reis, R. C., 2014, ApJ, 792, 19
- Richards, G. T., et al., 2006, AJ, 131, 2766
- Risaliti, G., et al., Nature, 494, 449
- Shakura, N. I. & Sunyaev, R. A., 1973, AAP, 24, 337
- Walton, D. J., et al. 2014, ApJ, 788, 76
- Walton, D. J., et al. 2015, ApJ, 805, 161
- Volonteri, M., Sikora, M., Lasota, J. P. & Merton, A., 2013, ApJ, 775, 94

The Most Luminous Infrared Galaxies in the Universe

Chao-Wei Tsai* (3266), Peter Eisenhardt (3266), Daniel Stern (3266),
Jingwen Wu (UCLA), Roberto Assef (U of Diego Portales, Chile), Andrew Blain (U Leicester)
and WISE Extragalactic Science Collaboration

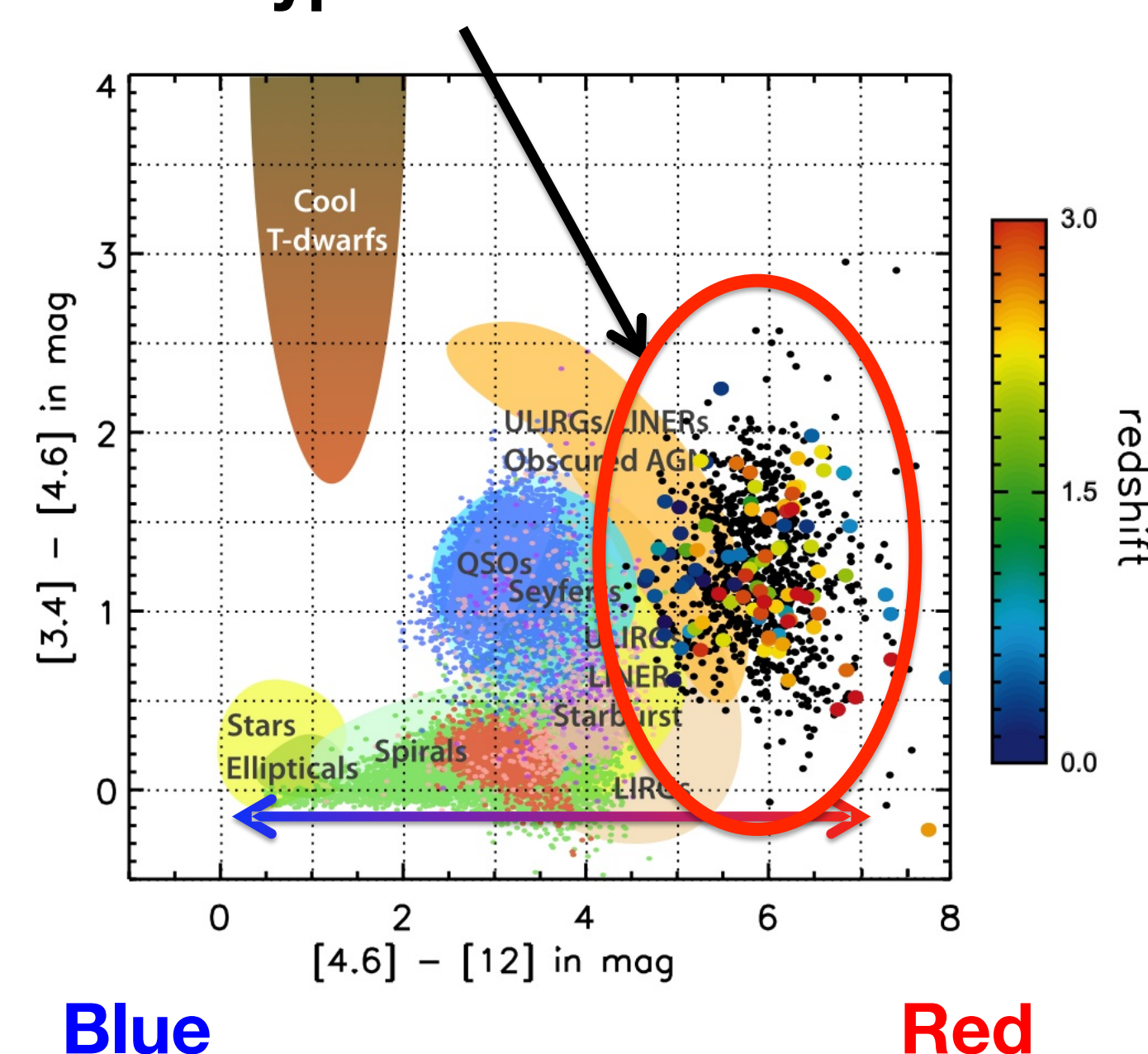
What's new?

Using all sky mid-IR survey data from *Wide-field Infrared Survey Explorer (WISE)*, we have discovered more than one hundred hyperluminous infrared galaxies that radiate over 10^{13} solar luminosities in the infrared. These galaxies, including

W2246-0526 - as luminous as 350 trillion suns and the most luminous galaxy known so far, are likely powered by the accretion of supermassive black holes above a few times 10^9 solar mass.

How to find them?

WISE hyperluminous Galaxies



Friday, May 22, 2015 » MORE AT FACEBOOK.COM/PASADENASTARNEWS AND TWITTER.COM/PASSTARNEWS pasadenastarnews.com

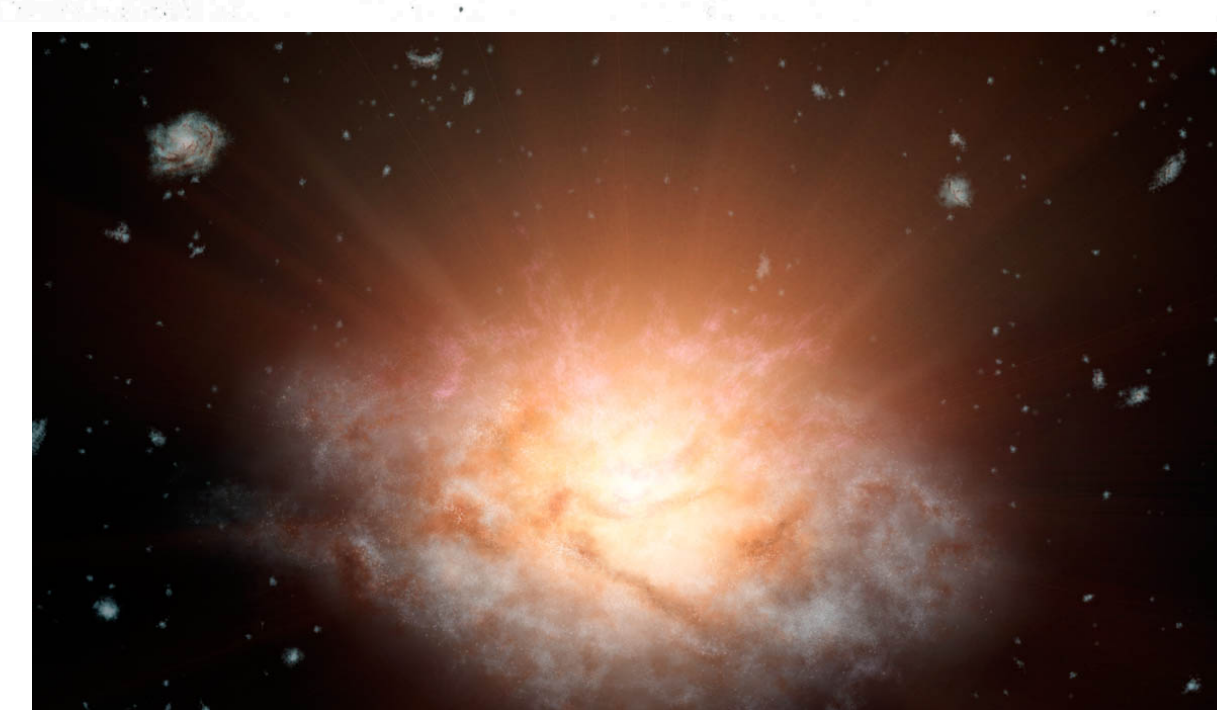
JET PROPULSION LABORATORY DISCOVERY

The most luminous galaxy found

LA CAÑADA FLINTRIDGE »
A distant galaxy sizzling with light from more than 300 trillion stars has been named the most luminous galaxy, NASA's Jet Propulsion Laboratory announced Thursday.

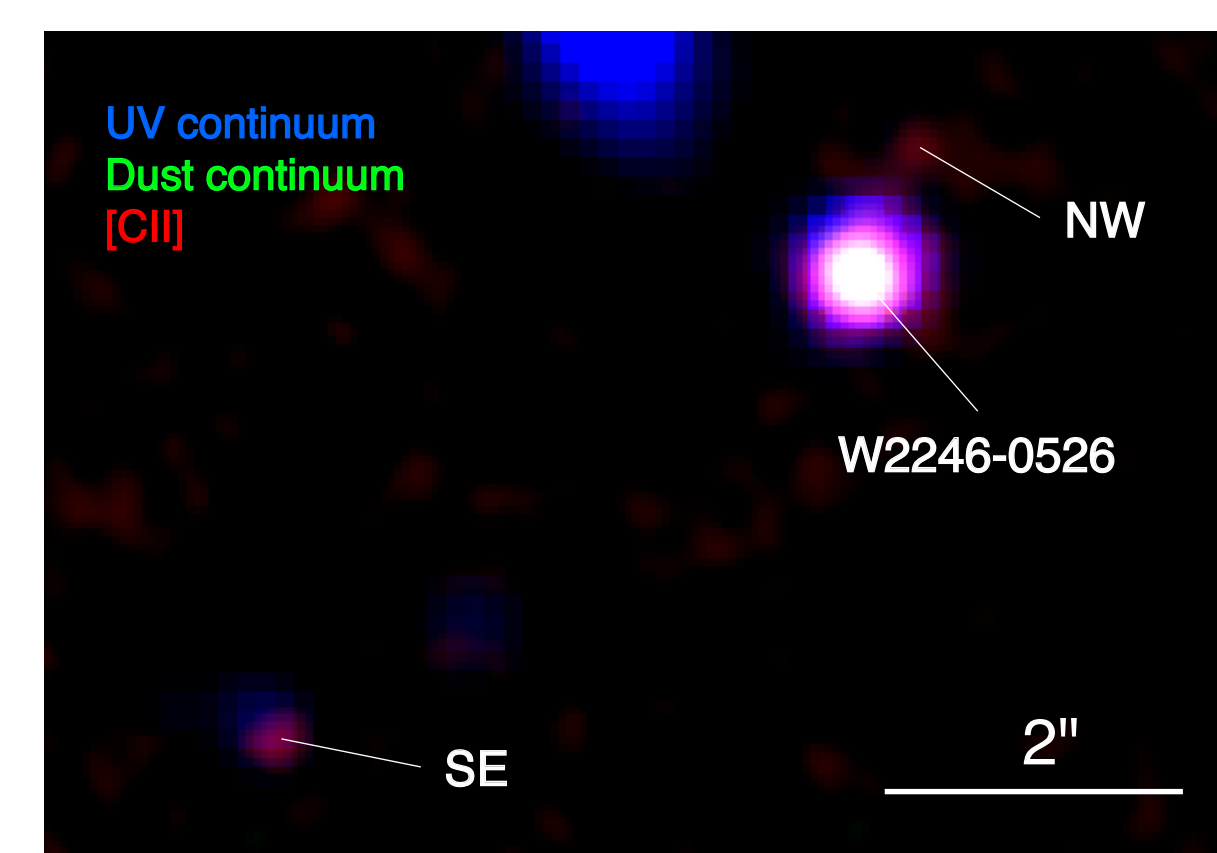
NASA's Wide-field Infrared Survey Explorer spacecraft, managed and operated by JPL, discovered the bright galaxy, which belongs to a new class of objects called extremely luminous infrared galaxies. The light may originate from a major growth spurt of the galaxy's black hole, said Chao-Wei Tsai of JPL and lead author of a report published Friday.

by Zen Vuong, Pasadena Star-News
Based on NASA Press-Release 15-095
and Tsai et al. 2015, ApJ



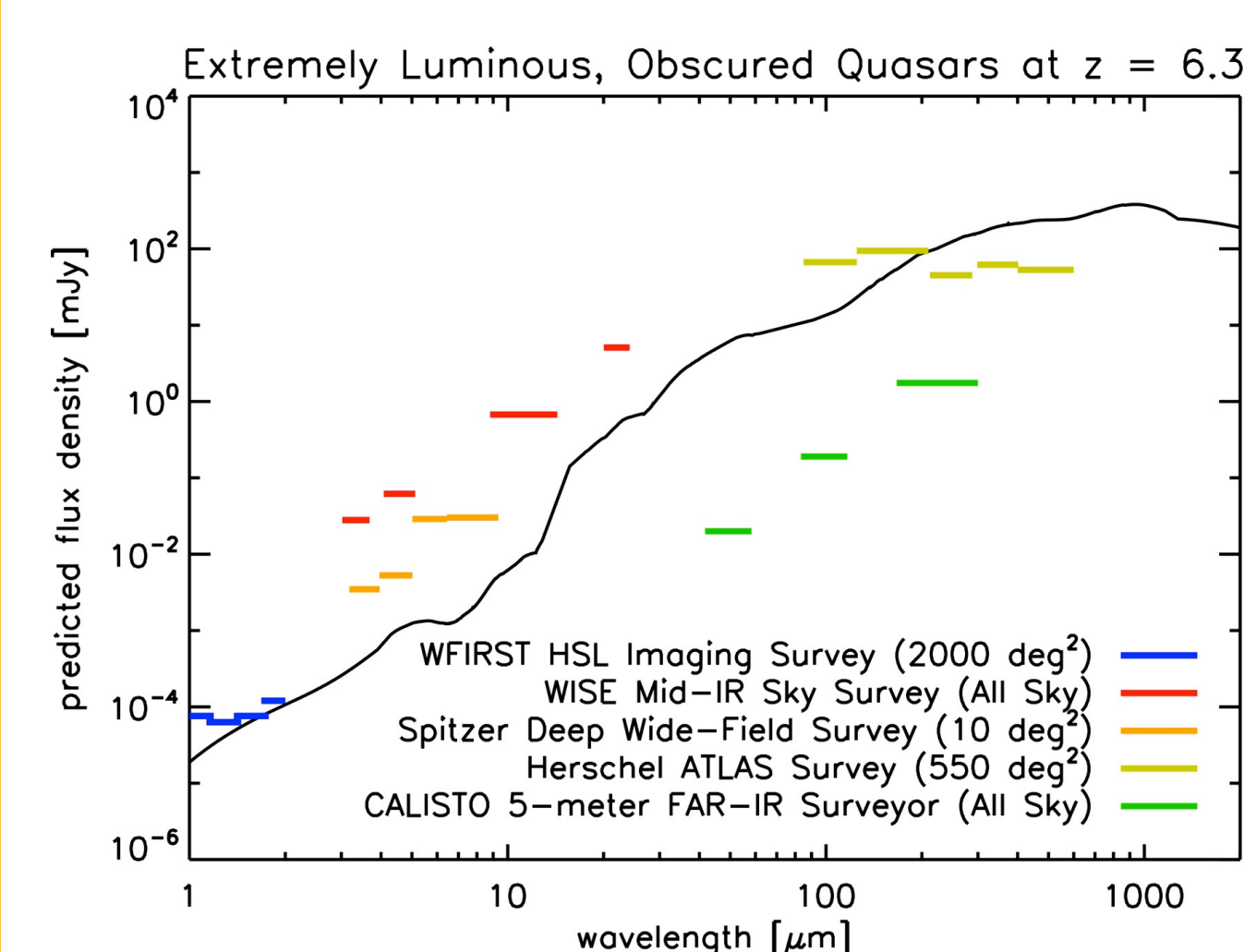
NASA/JPL-CALTECH

This artist's concept depicts the current record holder for the most luminous galaxy in the universe. The galaxy, WISE J224607.57-052635.0, is erupting with light equal to more than 300 trillion suns. It was discovered using data from NASA's WISE mission.



ALMA and HST images of **W2246-0526**
Diaz-Santos et al. 2015, Nature, subm.

and is reradiated in the infrared, peaking at rest frame ~ 6 microns. They have a comparable number density to the luminous quasars. These hyperluminous and obscured galaxies may have similar counterparts at even earlier epochs, within the first billion years of the Universe. But

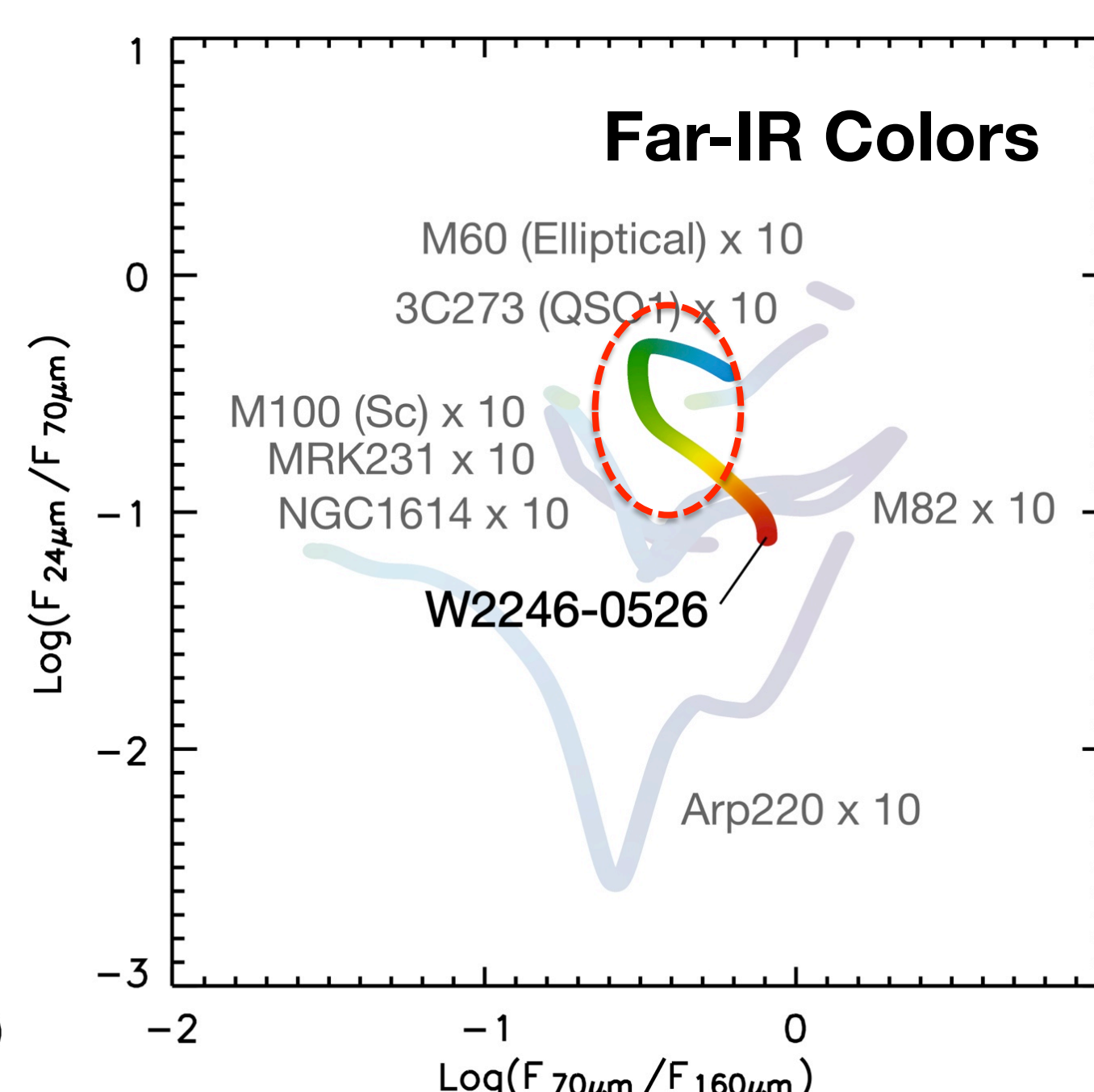
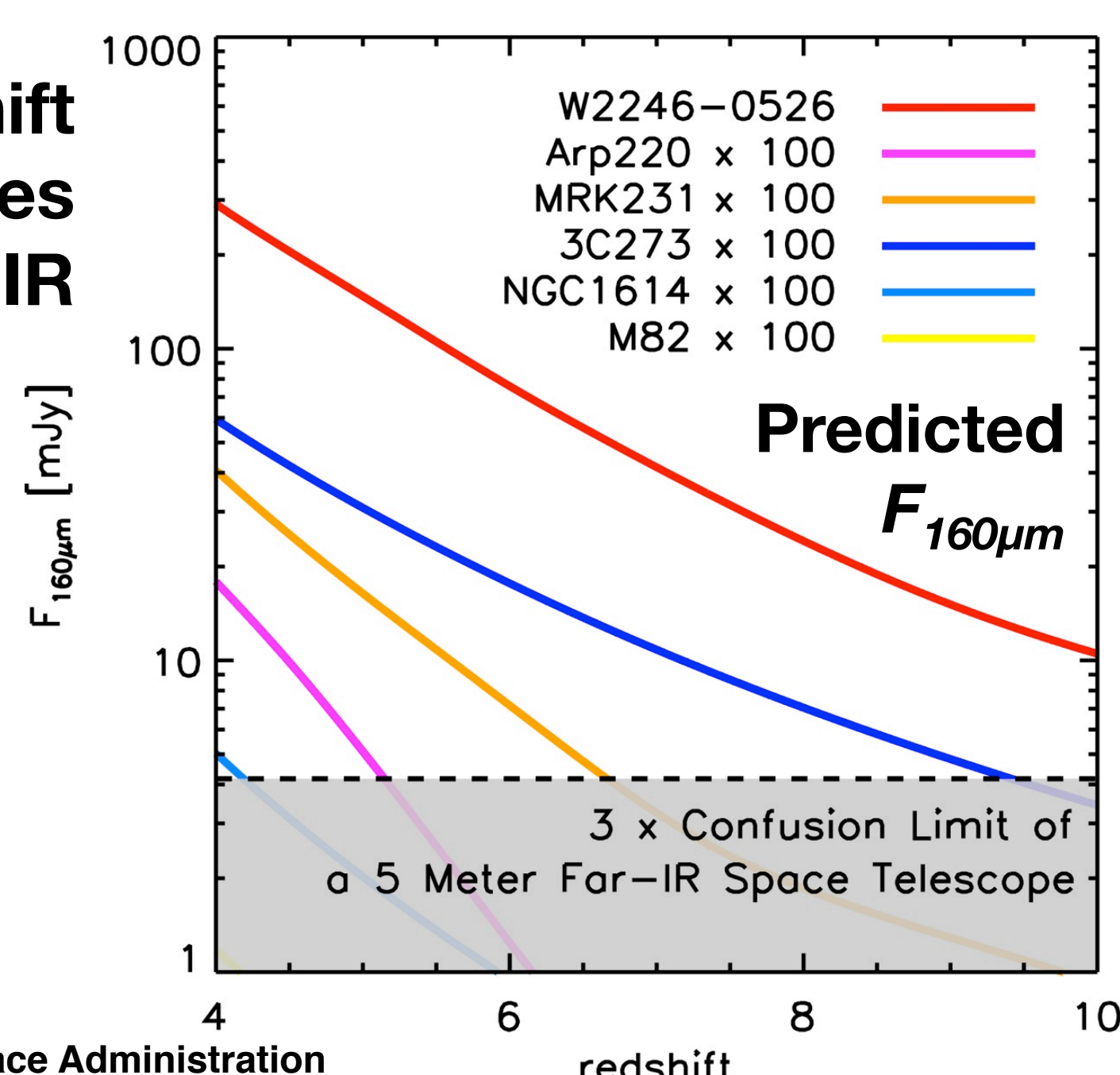


WISE hyperluminous galaxies are selected by their extremely red colors in WISE mid-infrared bands, which indicate strong activity in a dusty environment. These galaxies are likely powered by accreting massive black holes at center.

current surveys are not sufficient to detect them.

Looking forward: Far-IR Mission in 2020s

High-redshift luminous galaxies in Far-IR



Because hyperluminous infrared galaxies are rare and distant, deeper far-IR sky surveys are needed in the future to investigate their analog in the earlier universe. A 5-meter far-IR telescope will be sufficiently picking up similar luminous and dusty populations at the dawn of the Universe.

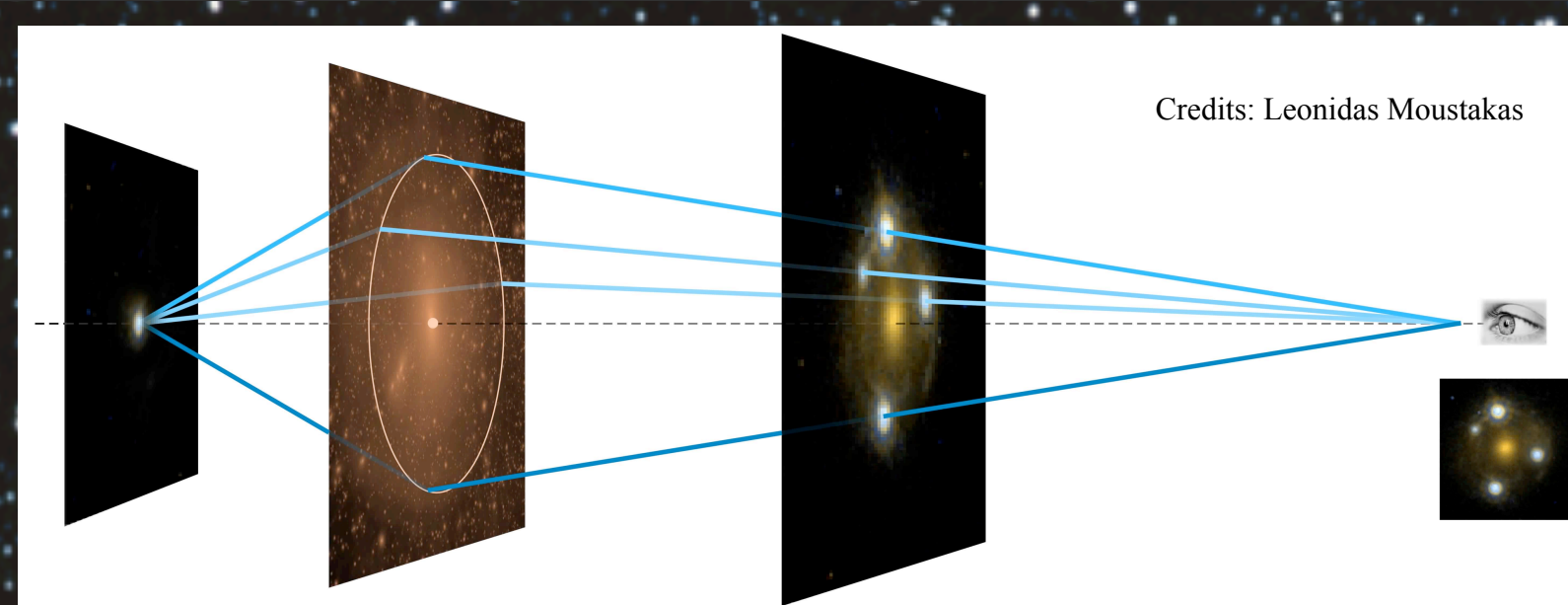
Finally Free: Unlocking Dark Matter Physics from Galactic Substructures

Francis-Yan Cyr-Racine, KISS Postdoctoral Fellow (3266)

Leonidas Moustakas (3266), Charles R. Keeton (Rutgers), Kris Sigurdson (UBC)

Executive Summary

Strong gravitational lensing of a distant source by a foreground galaxy provides a unique way to probe dark matter at cosmological distances. Since the distribution of dark matter within lens galaxies strongly depends on its particle physics, observations of strong gravitational lenses can yield important clues about dark matter.



Credits: Leonidas Moustakas

What is Dark Matter?

It is now well established that the matter content of the Universe is dominated by an unknown exotic component whose properties appear very different compared to the normal baryonic matter surrounding us on Earth. The key point is that the particle physics governing dark matter affects how it is distributed on small length scales (see Fig. 1 and 2). Since the substructure content of galaxies directly depends on this small-scale behavior, constraints on the dark matter subhalos from gravitational lensing give clues about the properties of dark matter particles such as their mass and their possible interactions.

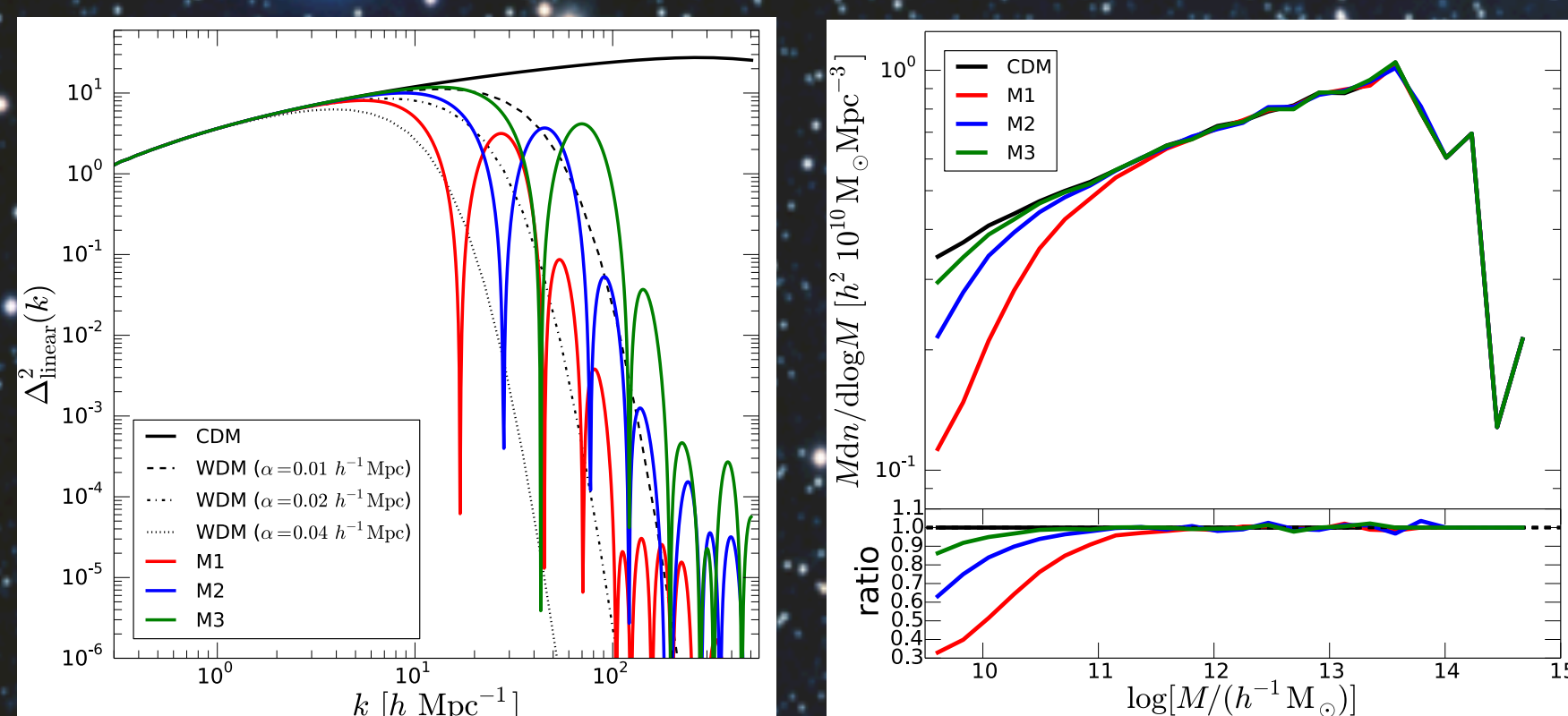


FIG. 1: (Left panel) Linear matter power spectrum plotted as a function of comoving wavenumber k (from Vogelsberger et al. 2015). The black thin solid line illustrates the power spectrum for standard cold dark matter, the dashed lines show different warm dark matter candidates, while the thick colored solid lines show the linear power spectrum for different self-interacting model (Cyr-Racine and Sigurdson 2013; Cyr-Racine et al. 2014) that couples to a bath of “dark” radiation until late times. (Right panel) Halo mass function for cold and self-interacting dark matter models. We observe that the self-interacting models have significantly less small-mass halos than cold dark matter.

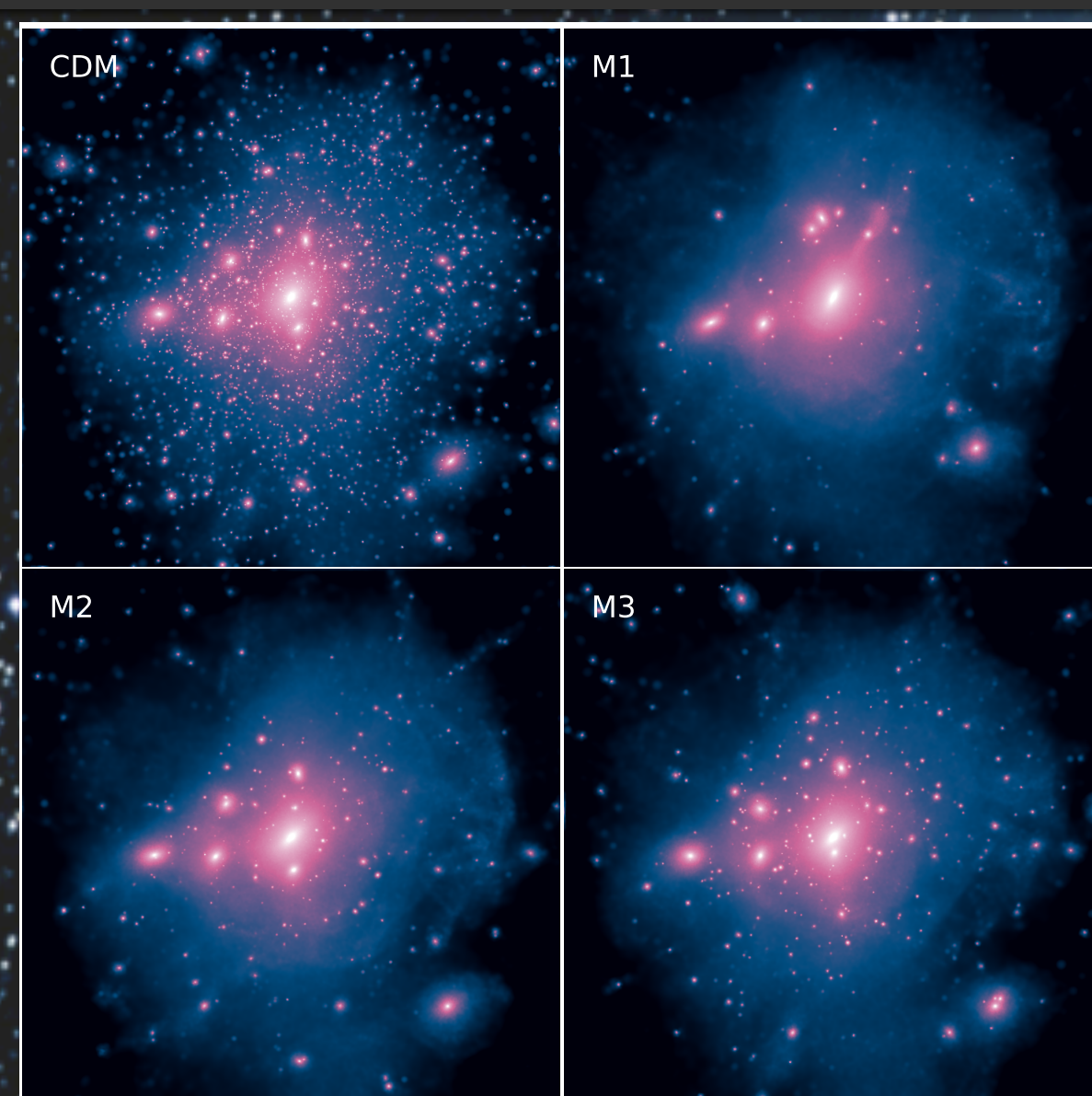


FIG. 2: Simulated galactic dark matter halos for different dark matter models discussed in Fig. 1. Here, the color scale illustrates the dark matter density, with warmer color indicating higher density. These are the result of dark matter-only N -body simulations (from Vogelsberger, Zavala, Cyr-Racine et al. 2015).

National Aeronautics and Space Administration
Jet Propulsion Laboratory
California Institute of Technology
Pasadena, California

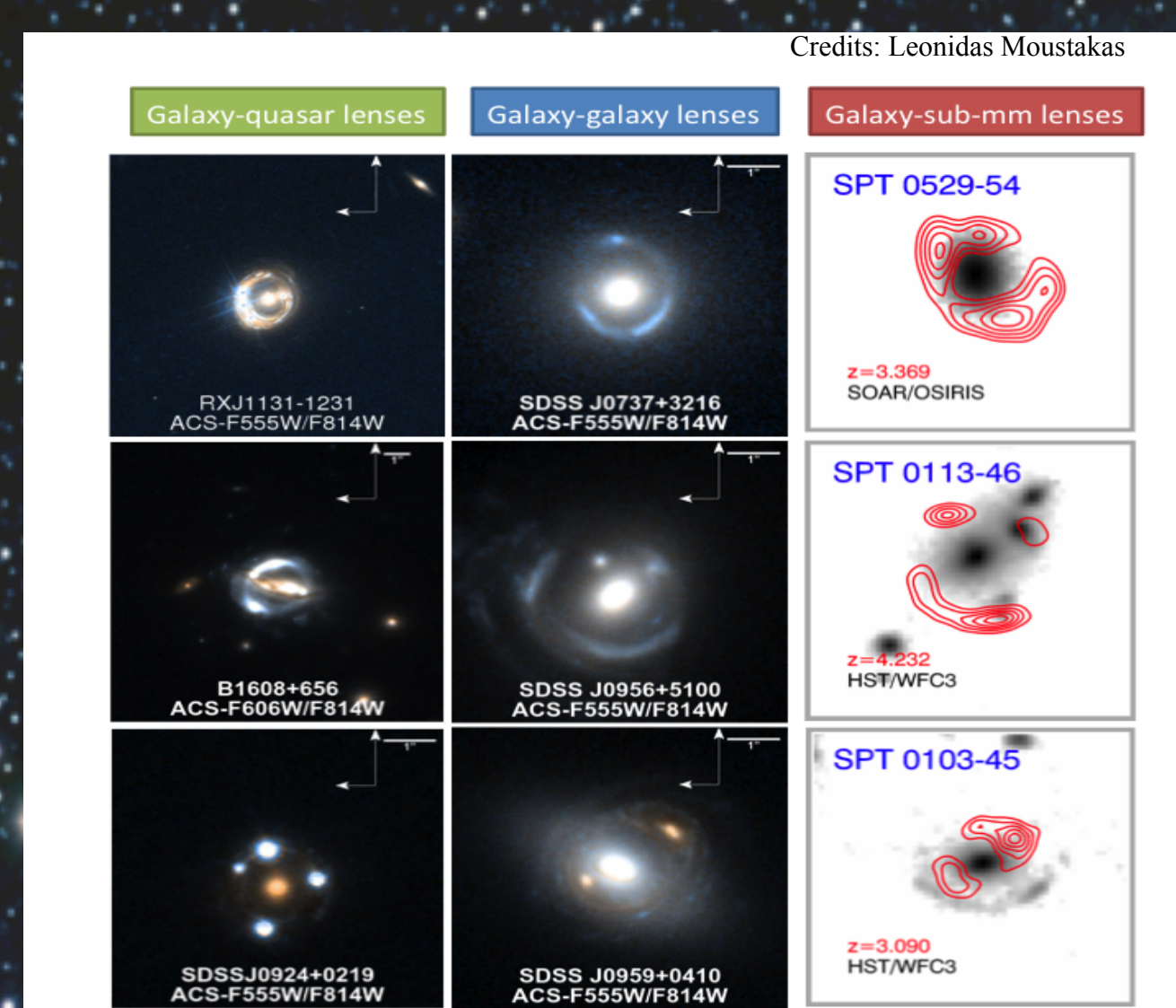
www.nasa.gov

Copyright 2015. All rights reserved.

References:
Cyr-Racine & Sigurdson, 2013, Phys. Rev. D87, 103515.
Cyr-Racine et al., 2014, Phys. Rev. D89, 063517.
Cyr-Racine et al., 2015, arXiv:1506.09724.
Keeton & Moustakas, 2009, ApJ 699, 1720.
Keeton, 2009, arXiv:0908.3001.
Skilling, 2004, AIP Conf. Proc. 735, 395.
Vogelsberger, Zavala, Cyr-Racine et al., 2015, in prep.

Observed Strong Lenses

There are many types of observed strong lenses (see Fig. 3), each presenting unique constraining power on dark matter substructures as well as modeling challenges. The key observables used to determine the distribution of dark matter within the lens are the positions of the multiple images of the source, the brightness of each pixel, and (for compact sources) the arrival time delays between the different images.



Credits: Leonidas Moustakas

FIG. 3: Montage of typical galaxy-scale strong gravitational lenses (c.f. the Master Lens Database, <http://masterlens.org>).

Substructure Lensing

The presence of dark matter substructure within the lens galaxy gives rise to small fluctuations in the observable properties of gravitational lenses that cannot be explained by changes in the uniform mass distribution of the lens. We have developed (Cyr-Racine et al. 2015) a novel approach that greatly speeds up the analysis of the impact of substructures on the lensing observables and also provides new insights on substructure lensing. We divide the subhalos into a distant and local population (see Fig. 4) and find that time-delay fluctuations are mostly affected by distant substructures (see Keeton and Moustakas 2009), while image brightness perturbations are mostly caused by local subhalos.

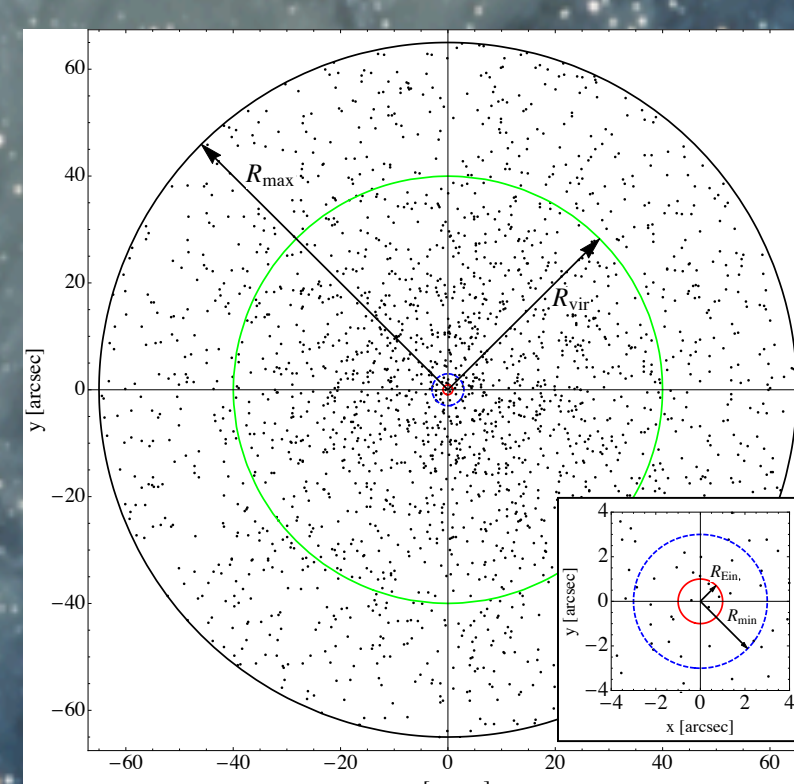


FIG. 4: Illustration of the typical scales involved in a galaxy-scale strong lenses. The lensed images form very close to the Einstein radius (red dashed circle) which itself is located in the very inner region of the dark matter halos (that has radius R_{max}). For our analysis, we divide the subhalo population into a local (within R_{min}) and a distant (beyond R_{min}) sub-population. As shown in Fig. 5, these two populations affect lensing observables differently.

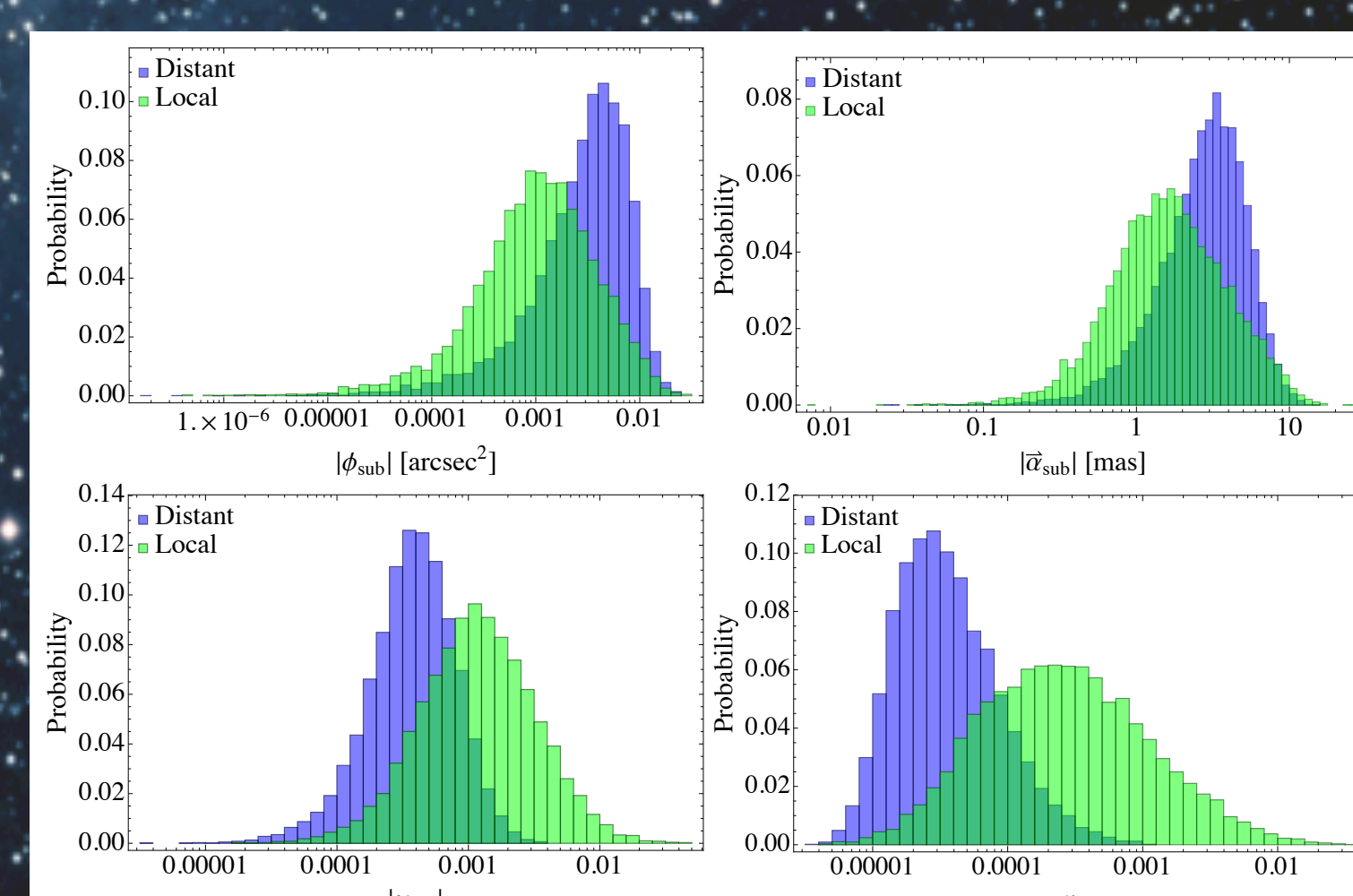


FIG. 5: Probability distributions for the local and distant contributions to the linear lensing quantities. Clockwise from the upper left corner, the histograms show the distribution for gravitational potential, lensing deflection, shear, and convergence perturbations, respectively. We observe that distant substructures are dominating the potential perturbations (responsible for time-delay fluctuations), while local perturbations dominate shear and convergence perturbations (responsible for image brightness fluctuations).

Distant Subhalo Population

The vast majority of subhalos inside lens galaxies are located in the “distant” region of the lens (see Fig. 4). Their large number ensures that statistics of the lensing fluctuations they give rise to are approximately Gaussian. (see also Keeton 2009). We can therefore predict from first principles their impact on lensing observables (see Fig. 6) and marginalize over these distribution to obtain constraints on dark matter properties.

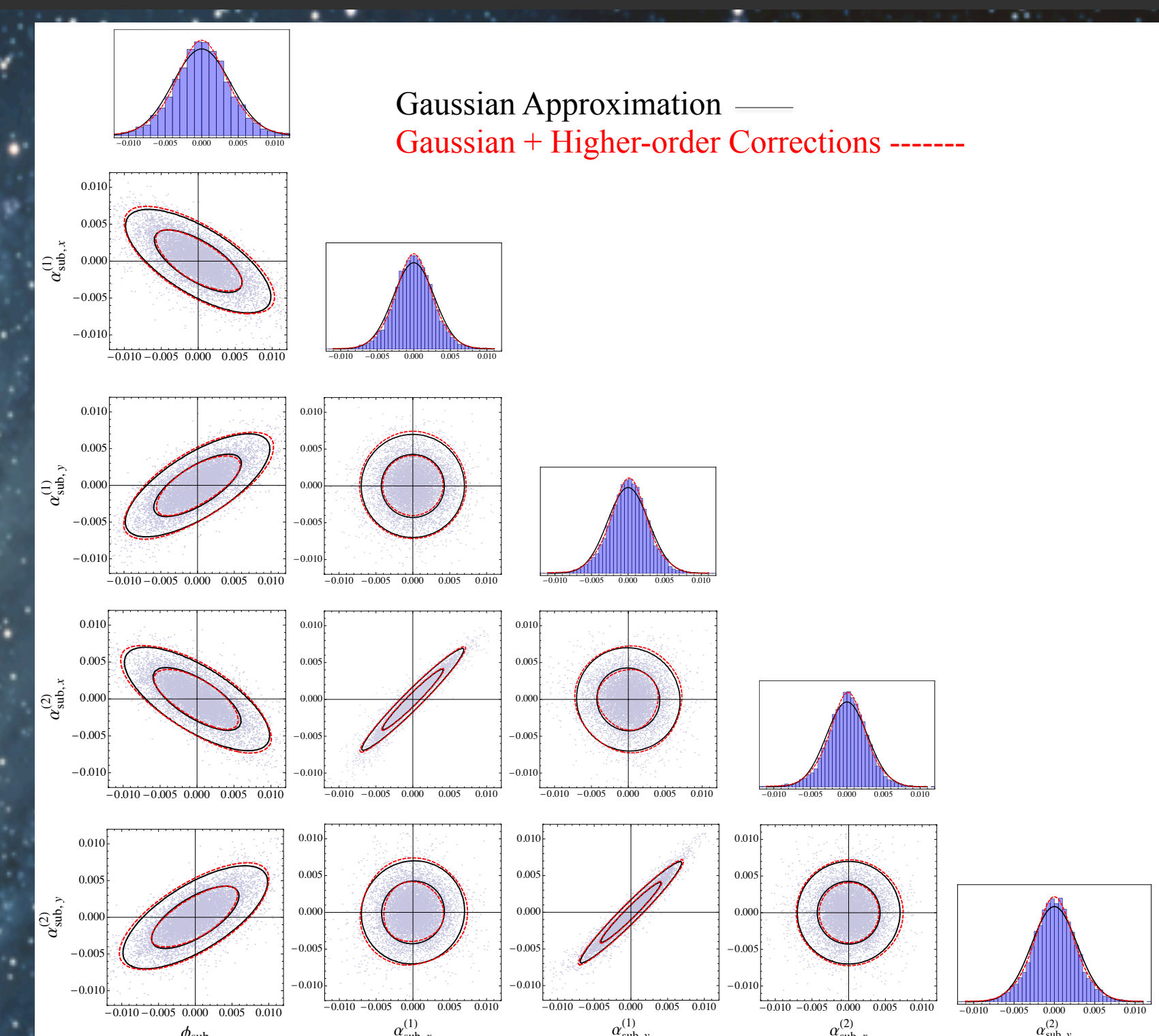


FIG. 6: Probability distribution function for the lensing deflections and relative time delay between two lensed images. The blue points and histograms show the results of 10^4 Monte Carlo realizations of a substructure population. The solid black lines show our Gaussian predictions, while the dashed red lines include the leading order deviation from Gaussianity (from Cyr-Racine et al. 2015).

Constraints on Substructures

Equipped with the distribution of lensing observables, we use a Bayesian inference scheme based on the Nested Sampling algorithm (Skilling 2004) to model the mass distribution of the lens as well as the parameters describing the dark matter substructure population. After marginalizing over nuisance parameters, we obtain the posterior probability distribution (see Fig. 7) for parameters describing the dark matter, allowing us to constrain the physics governing dark matter.

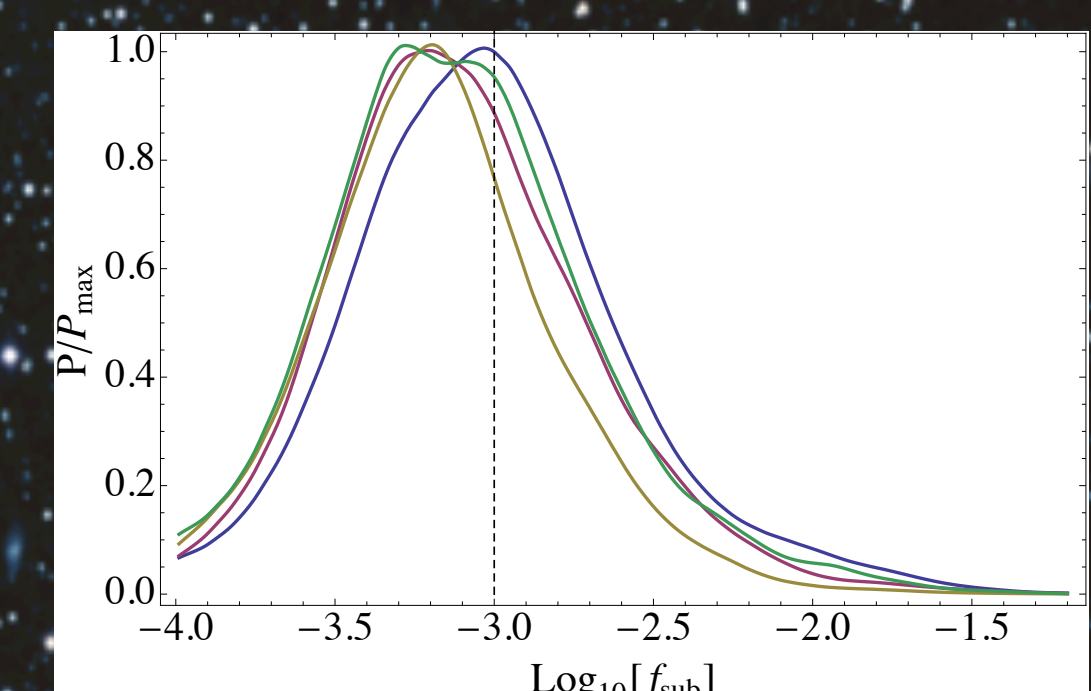


FIG. 7: Marginalized posterior probability distribution for the projected mass fraction in substructures (f_{sub}) for four different ensembles of mock gravitational lenses. The vertical dashed line displays the input value used for the mock data.

Future: Combining Multiple Lenses

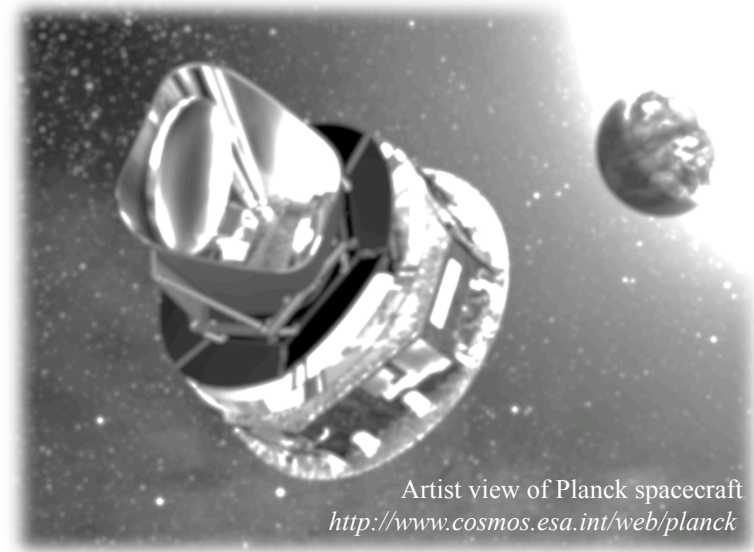
In order to maximize the constraining power of strong gravitational lensing on dark matter physics, one must properly combine the observations from multiple lenses. Developing the methodology to carry out such an analysis is the next major step in this research program and is necessary to fully take advantage of future surveys such as WFIRST or Euclid.

This work is supported in part by the W. M. Keck Institute for Space Studies.

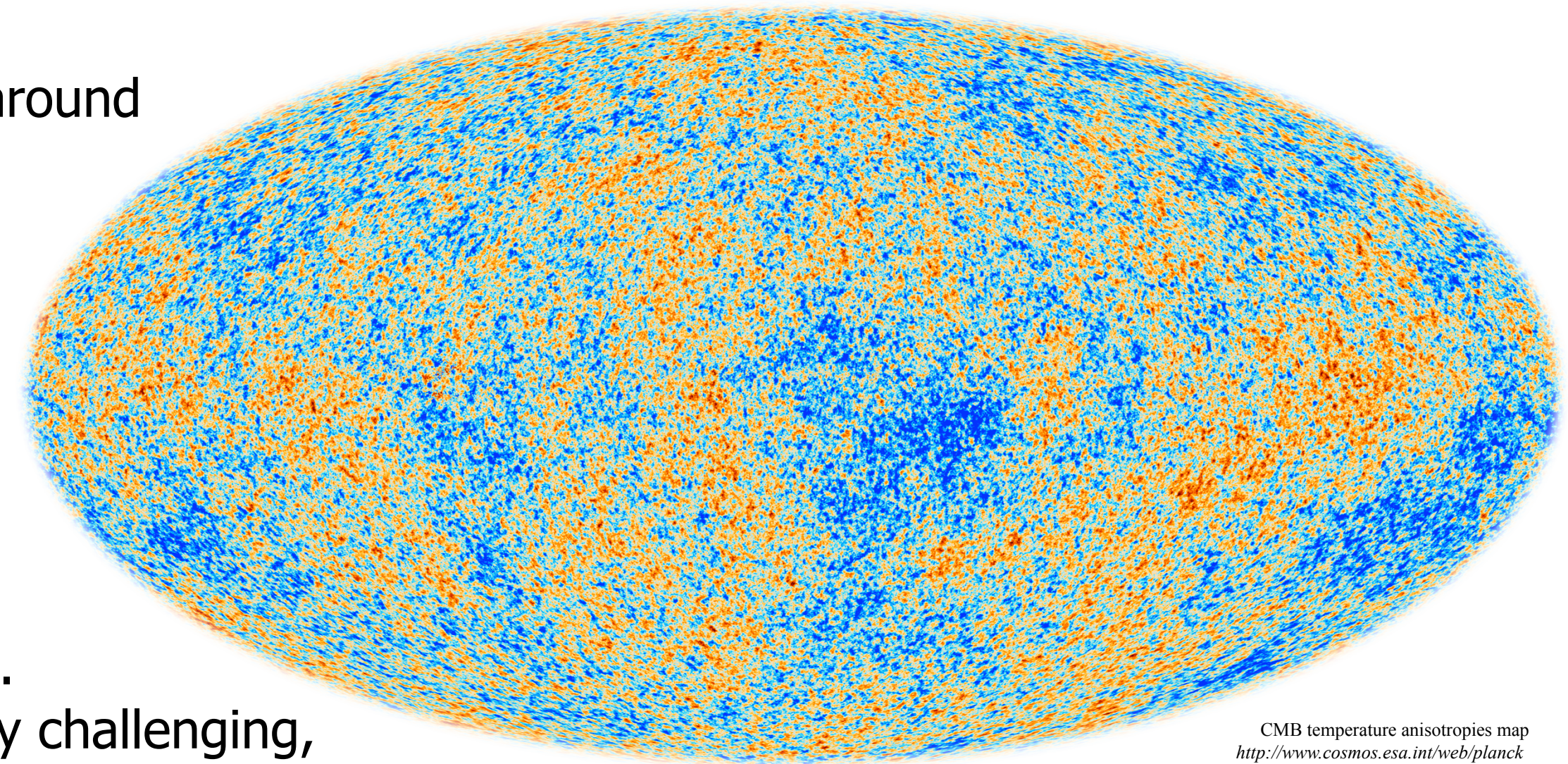
Poster No. A8

PLANCK High Frequency Instrument beam recovery

**Principal Investigator: Gael M. ROUDIER (3268)
Charles R. LAWRENCE (3267), Brendan P. CRILL (3268)**



PLANCK is an European Space Agency (ESA) spacecraft orbiting around the sun at the second Lagrange point. It scanned the entire sky to measure the Cosmic Microwave Background (CMB) anisotropies in temperature and polarization with unprecedented accuracy.



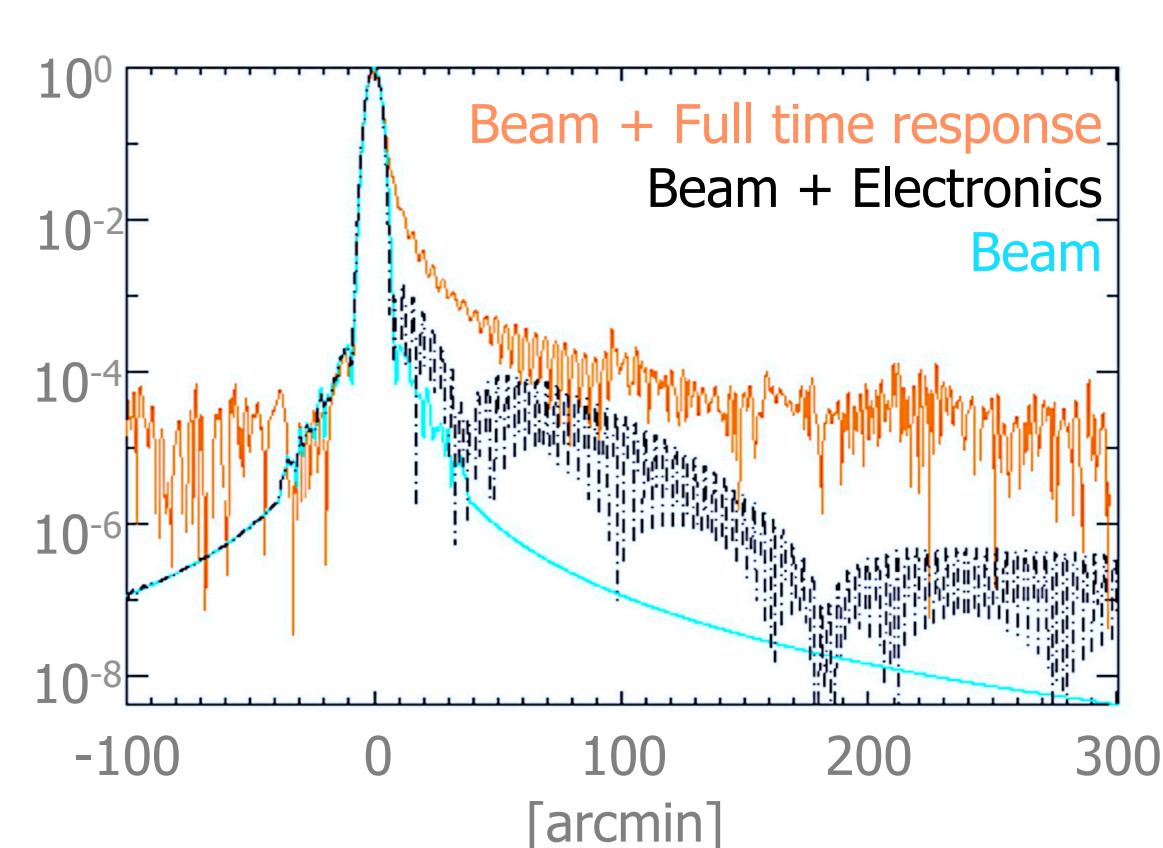
The CMB anisotropies power spectrum contains the necessary information to recover the cosmological standard model (LCDM) parameters. Because CMB polarization holds imprints of the inflation era, it allows to constrain the amplitude of the primordial gravitational wave modes predicted by General Relativity. The retrieval of this signature (B-modes) in the CMB polarized power spectra is extremely challenging, one has to achieve an exquisite control in the systematics that generate spurious signatures in this estimator.

- We present here the methodologies and tools we created for the PLANCK consortium to achieve the required accuracy in the beam estimate (Point Spread Function equivalent for an optical system). The beam window transfer function correlates angular scales, thus distorts the entire power spectrum estimates.
- We use Monte Carlo simulations results of the High Frequency Instrument (HFI) beam pipeline to constrain the Cosmic Birefringence (CB) angle, tracer of exotic physics that mixes the polarization modes, extremely sensitive to beam systematics.

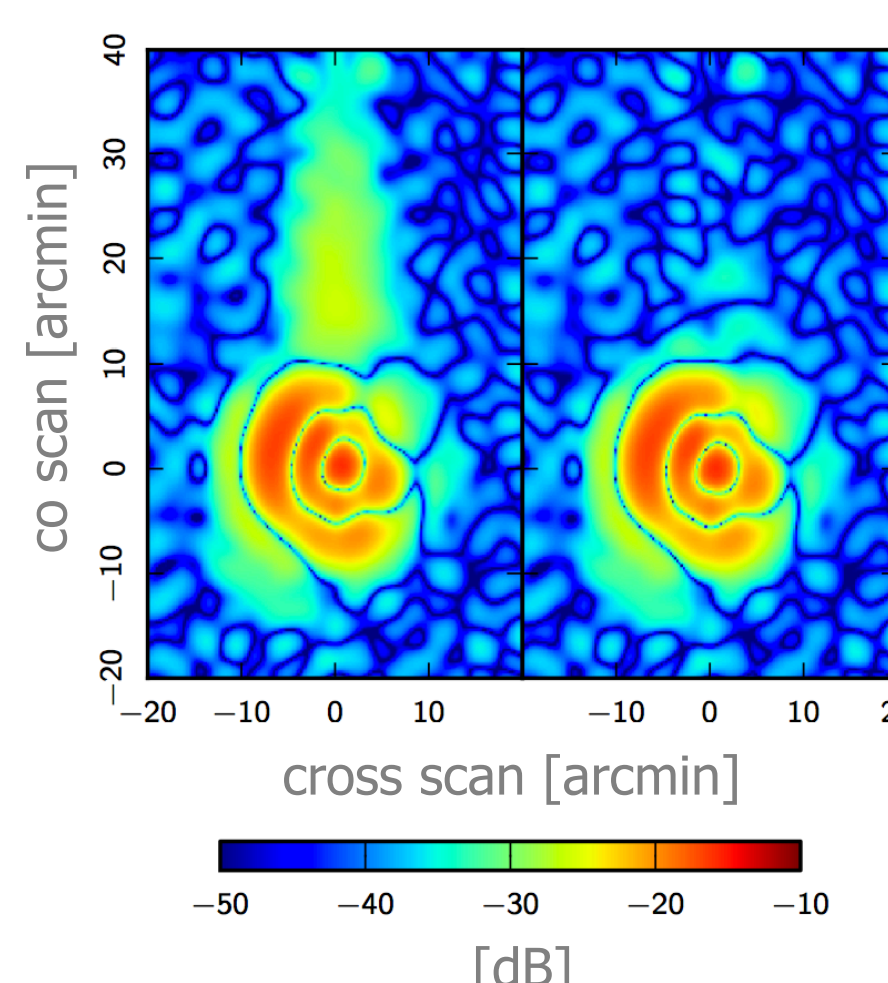
Time response and beam degeneracy

Planets provide a high quality signal in Planck HFI frequency bands. We use the combination of Mars, Saturn and Jupiter to constrain the different regimes of the beam up to 3 degrees : main beam peak, close side lobes and diffraction pattern.

Still, the signal we receive from the calibrators is the combination of the underlying beam and the time response of the detectors, the latter being defined as the sum of time constant decays convolved with the response of the detector's electronic chain.



Time response filtering and beam forming

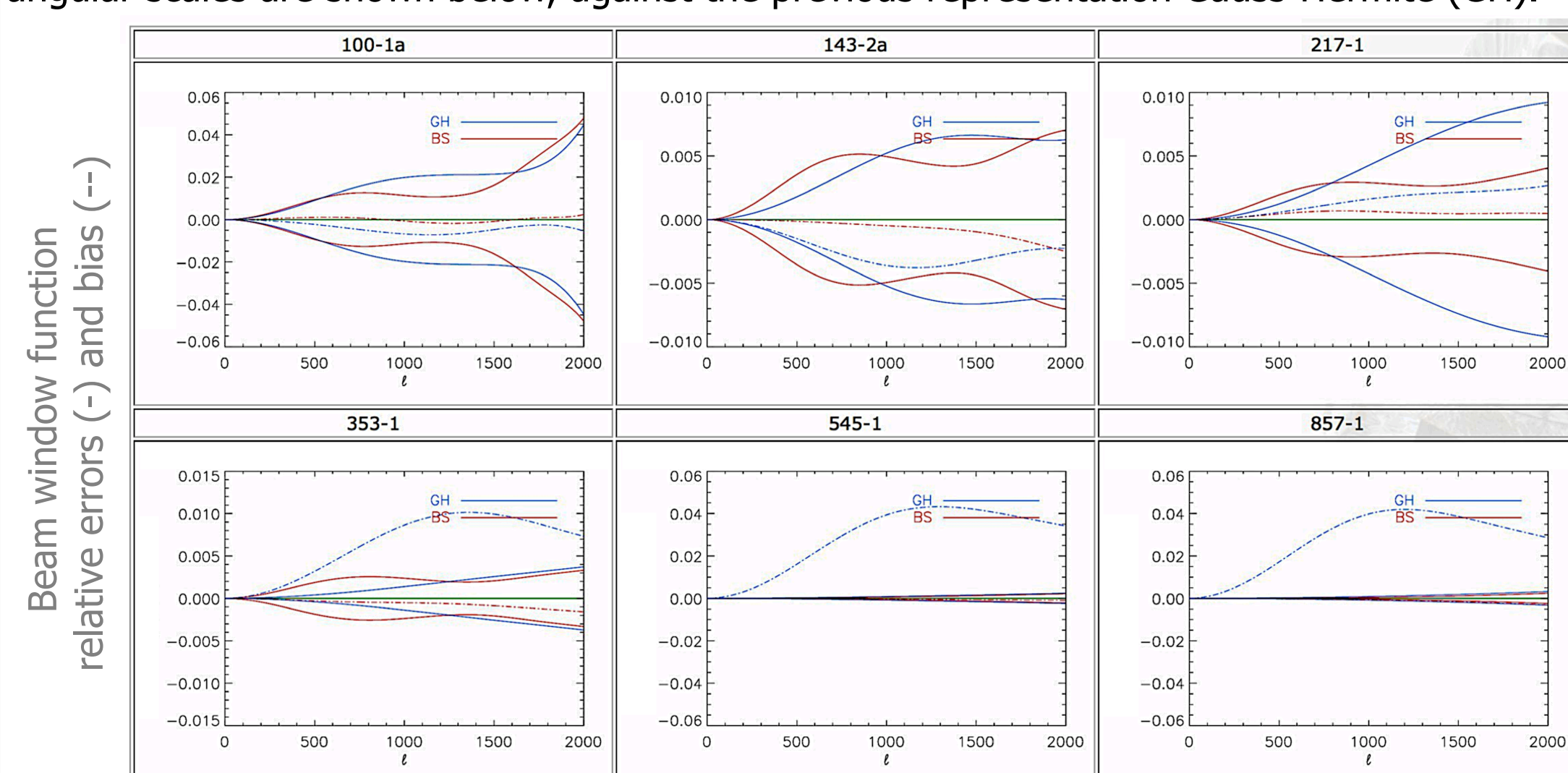


The degeneracy is broken using geometrical assumptions on the induced beam (compactness) while fitting for the time constants.

The left figure displays a 143 GHz beam minus its main component (elliptical Gaussian), using forecasted time constants from ground measurements (left panel) and the same difference using the beam forming code (right panel). The compactness criterion we impose on the recovered beam reduces the elongated artifact along the co scan direction, attributed to the fact that time constants may evolve from ground measurements.

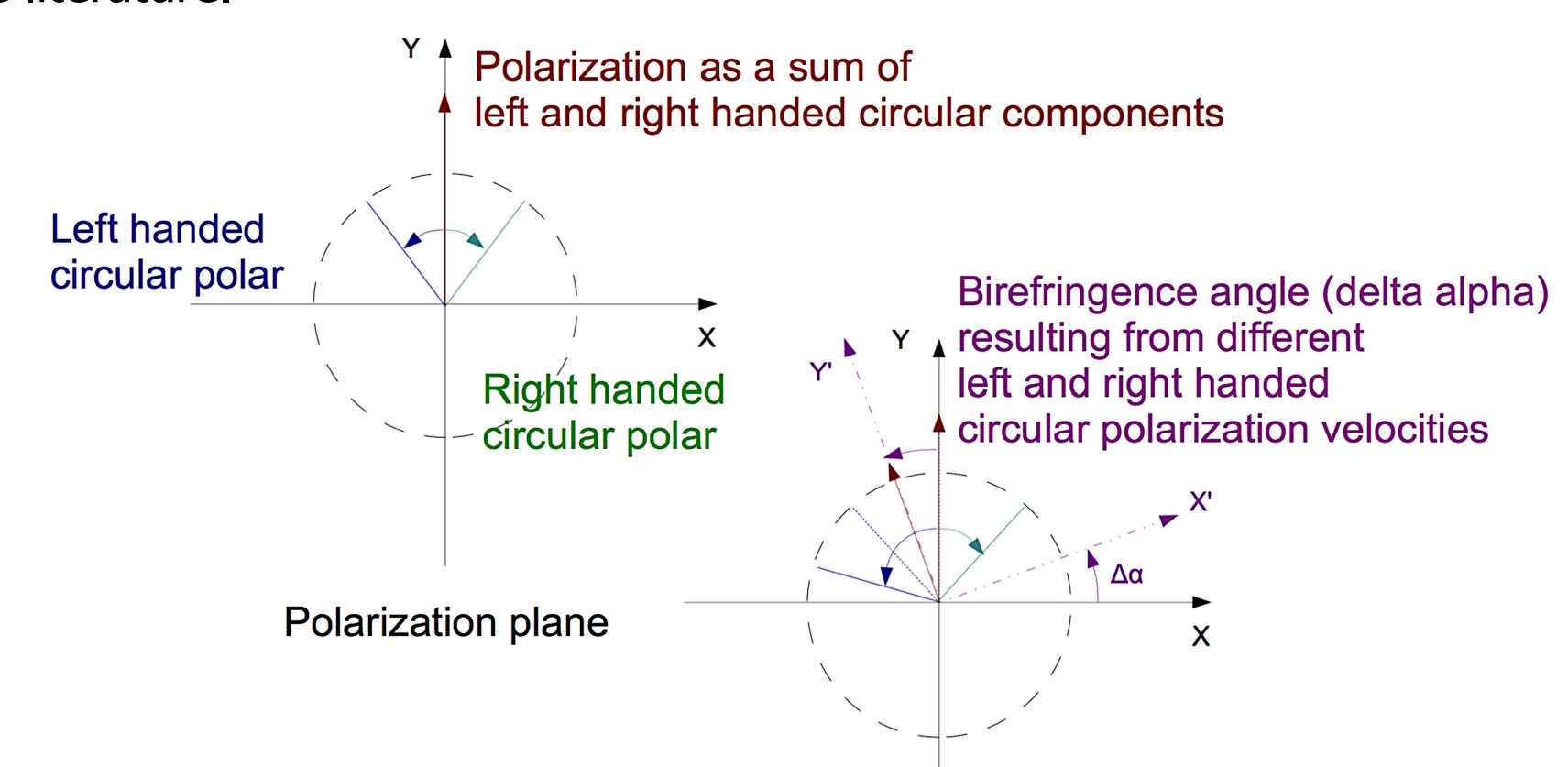
B-Spline beam representation

We fit for B-Spline coefficients to describe the main beam. The performances of the B-Spline (BS) representation, relative bias (dash line) and relative 1 sigma errors (solid lines) as a function of angular scales are shown below, against the previous representation Gauss-Hermite (GH).

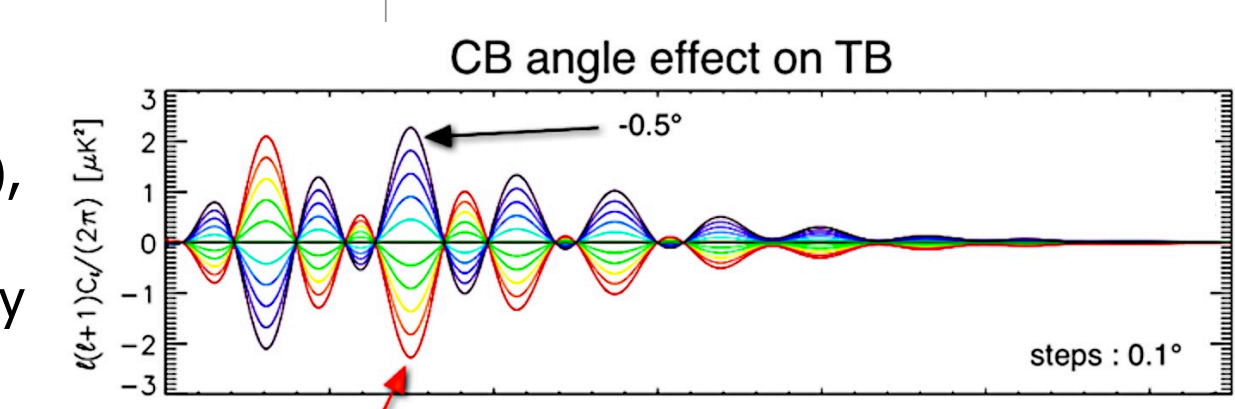


Cosmic Birefringence

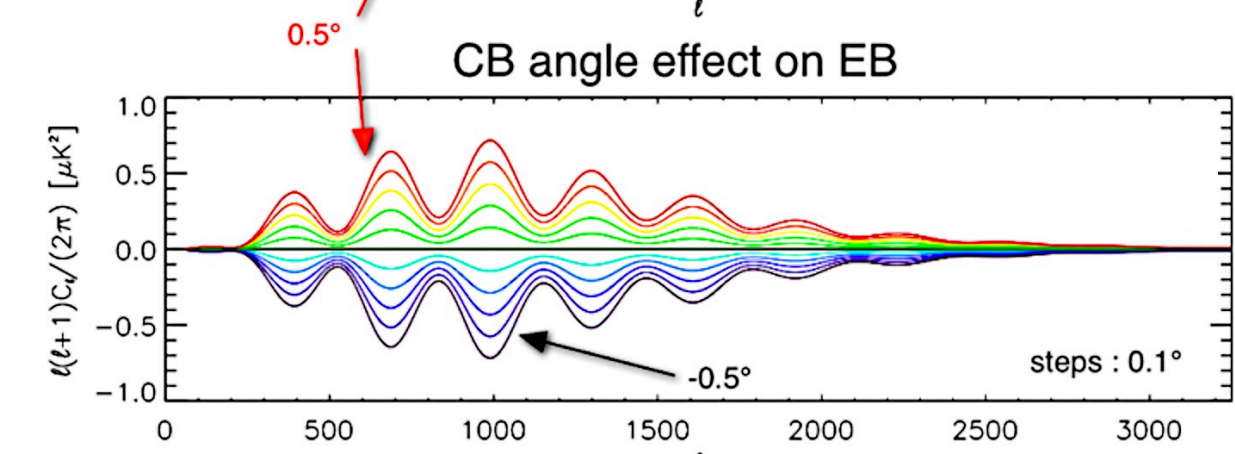
Cosmic Birefringence (CB) is referred as the rotation of the polarization plane of photons travelling cosmological distances through vacuum. The rotation can be described as a difference in left and right handed circular polarization velocities. Such an effect may occur in various extensions of the standard model of Physics. We expect the rotation angle, if exists, to be below 1 degree from the literature.



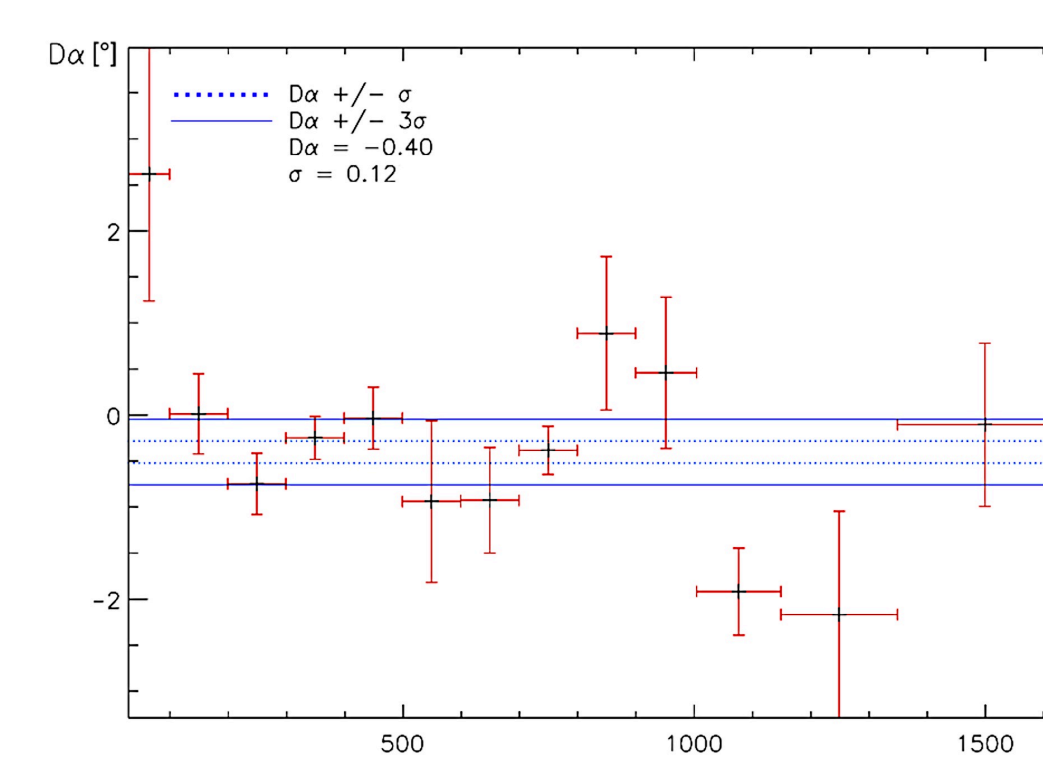
Such a rotation will induce a mixing between temperature and polarization modes (T, E, B), distorting the vanishing CMB power spectra TB and EB. In absence of such an effect, they are expected to be compatible with 0 across all angular scales.



The parity violations are expected to be of a few micro Kelvin squared at maximum, thus highly sensitive to any residual systematic in this poor signal to noise regime.



$$Q_{\ell}^{TB} = \tilde{C}_{\ell}^{TB} \cos(2\Delta\alpha) - \tilde{C}_{\ell}^{TE} \sin(2\Delta\alpha)$$



To solve for the angle, we combine polarized spectra TB and TE to build an estimator (Q_{TB}) compatible with zero, linking the CB angle (Delta alpha) to the observed spectra. Vanishing Q_{TB} admits a closed form solution for Delta alpha

We use Monte Carlo simulations of Planck polarized maps to propagate the statistical uncertainties on the recovered value of the CB angle: -0.40 ± 0.12 [degrees]

Still, such a rotation is perfectly mimicked by a consistent mismatch in the relative polarization angle of the detectors, traceable through the recovered beam orientations. We use the results from the B-Spline characterization to propagate errors due to beam orientation uncertainties and assess a total systematic error contribution completing the previous result :

$$-0.40 \pm 0.12 \text{ (statistical)} \pm 0.49 \text{ (systematics)} \text{ [degrees]}$$

Sensor effects on the study of Dark Energy using weak lensing

Principal Investigator: **Andrés Alejandro Plazas Malagón (3268-Caltech)**

Jason Rhodes (3268), Chaz Shapiro (389E)

Jet Propulsion Laboratory, California Institute of Technology

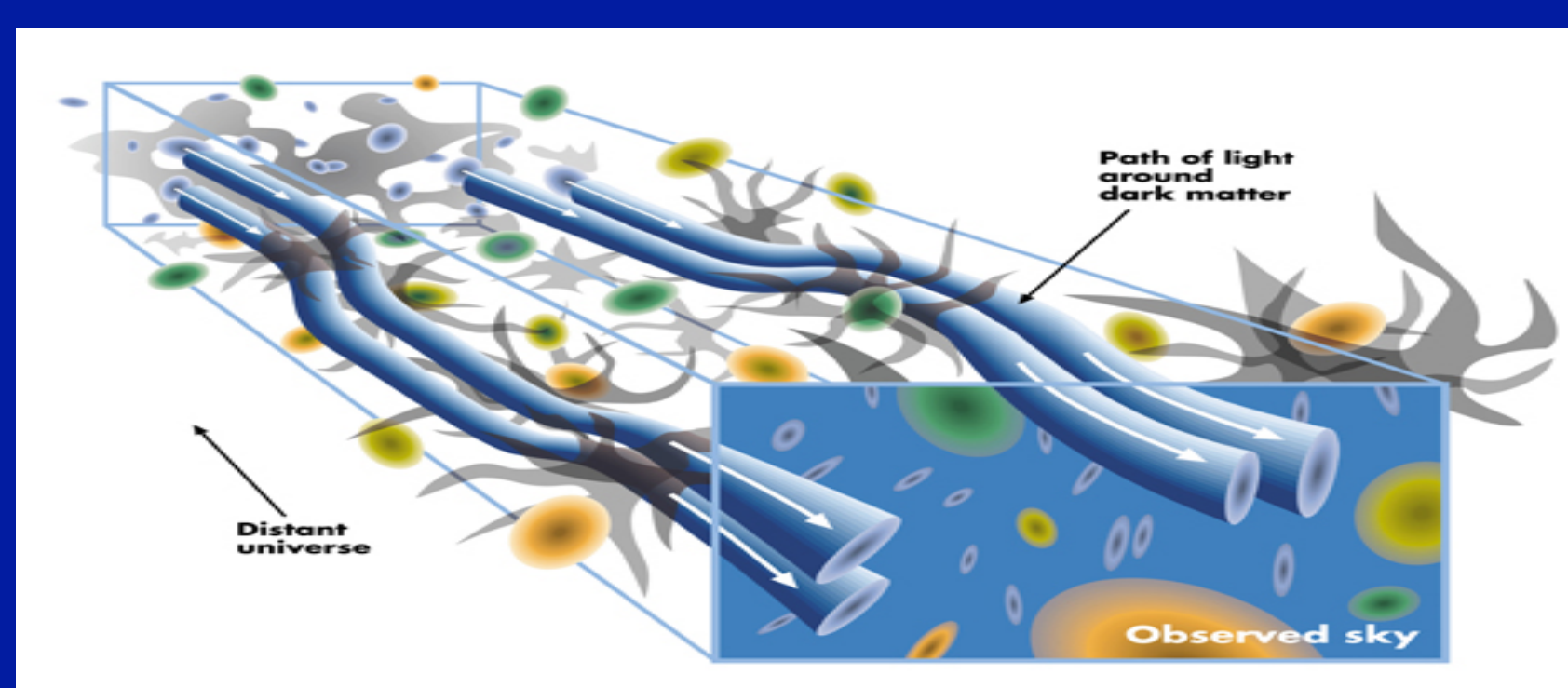
Executive Summary

The cause of the observed accelerated expansion of the Universe is one of the most important unanswered questions in modern physics. It could be due to a new component of the Universe with negative pressure (**"Dark Energy"**) or to a breakdown of General Relativity on cosmological scales (**"modified gravity"**). **Weak gravitational lensing** has become one of the most important tools to study this phenomenon, but **to reach its full potential careful attention must be paid to the characterization and control of systematic errors.**

We present here studies on the instrumental signatures that optical and infrared detectors leave on weak lensing observables.

Dark Energy and Cosmic Shear

- Dark Energy (DE) is one of the biggest mysteries in modern physics.
- We can learn about DE through cosmic shear, the subtle **distortions of galaxy shapes** by the dark matter distribution of the Universe.

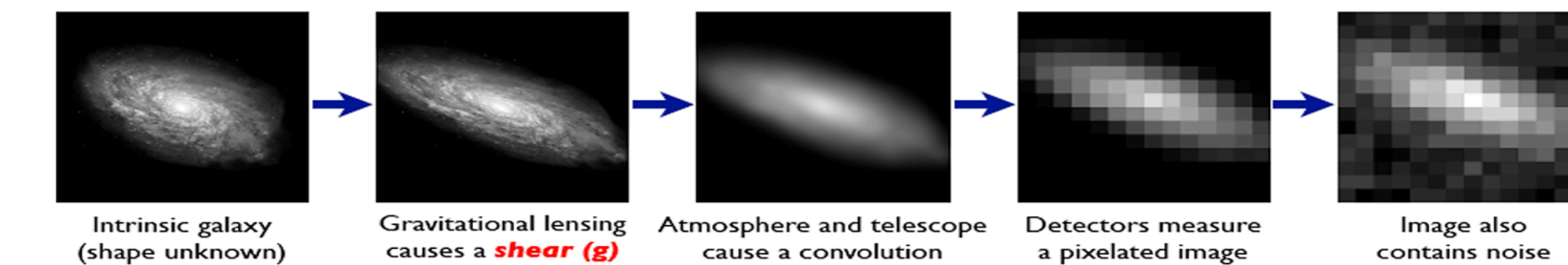


Shape measurement in weak lensing

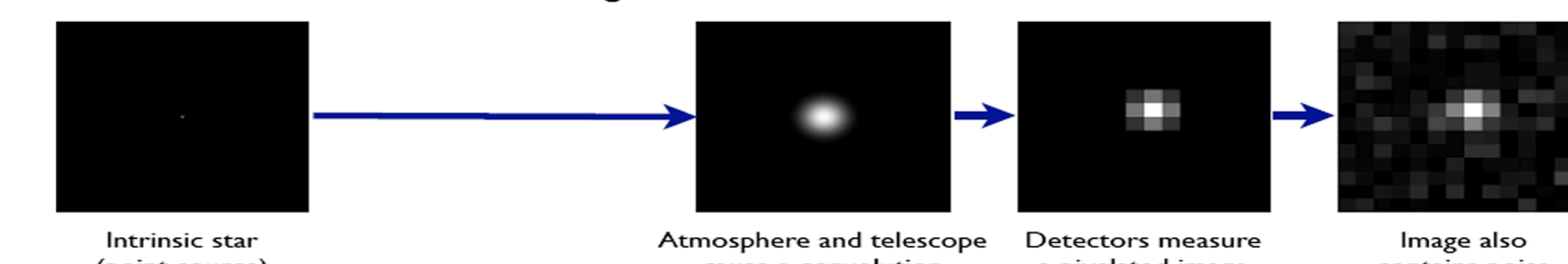
- Shape measurement is a highly non-trivial problem:

The Forward Process.

Galaxies: Intrinsic galaxy shapes to measured image:



Stars: Point sources to star images:

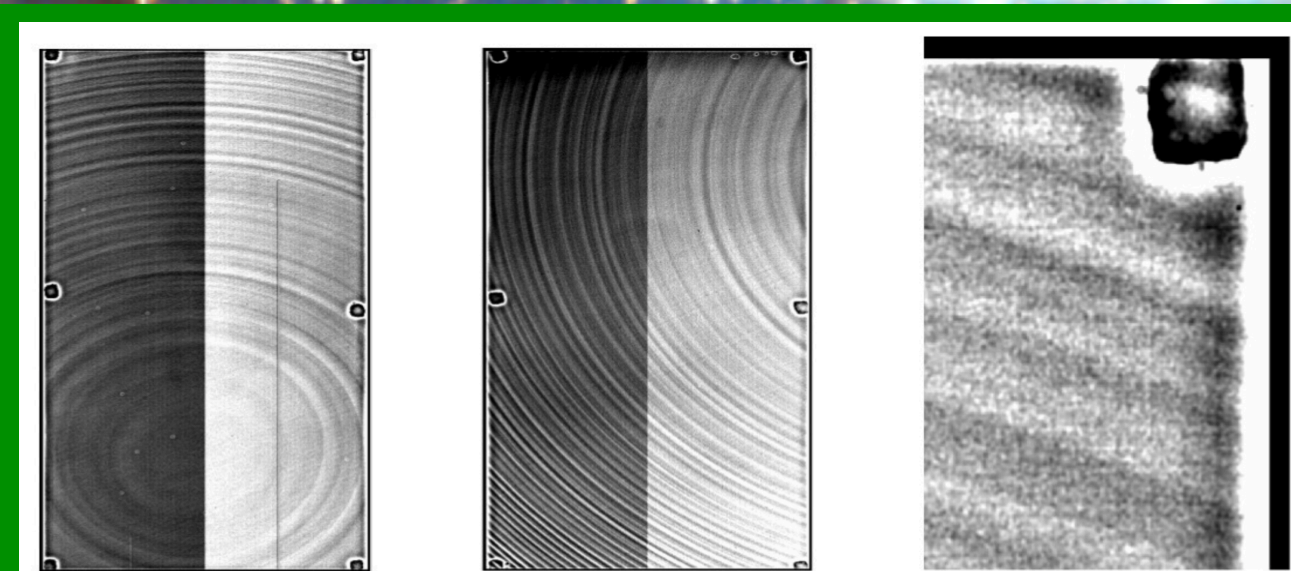


- Weak signal of 1-2%
- **Point Spread Function (PSF)** correction and modeling
- Model biases
- Noise biases
- **Instrumental signatures**
- Undersampled images in space

Objectives and Methods

- How do astronomical detectors bias astrophysical observables for weak lensing?
- What are the WL requirements that **NASA's Wide Field Infrared Survey Telescope (WFIRST)** detectors will have to satisfy?
- We use real data, lab measurements, and simulations to study this.

Structures in DES dome flats

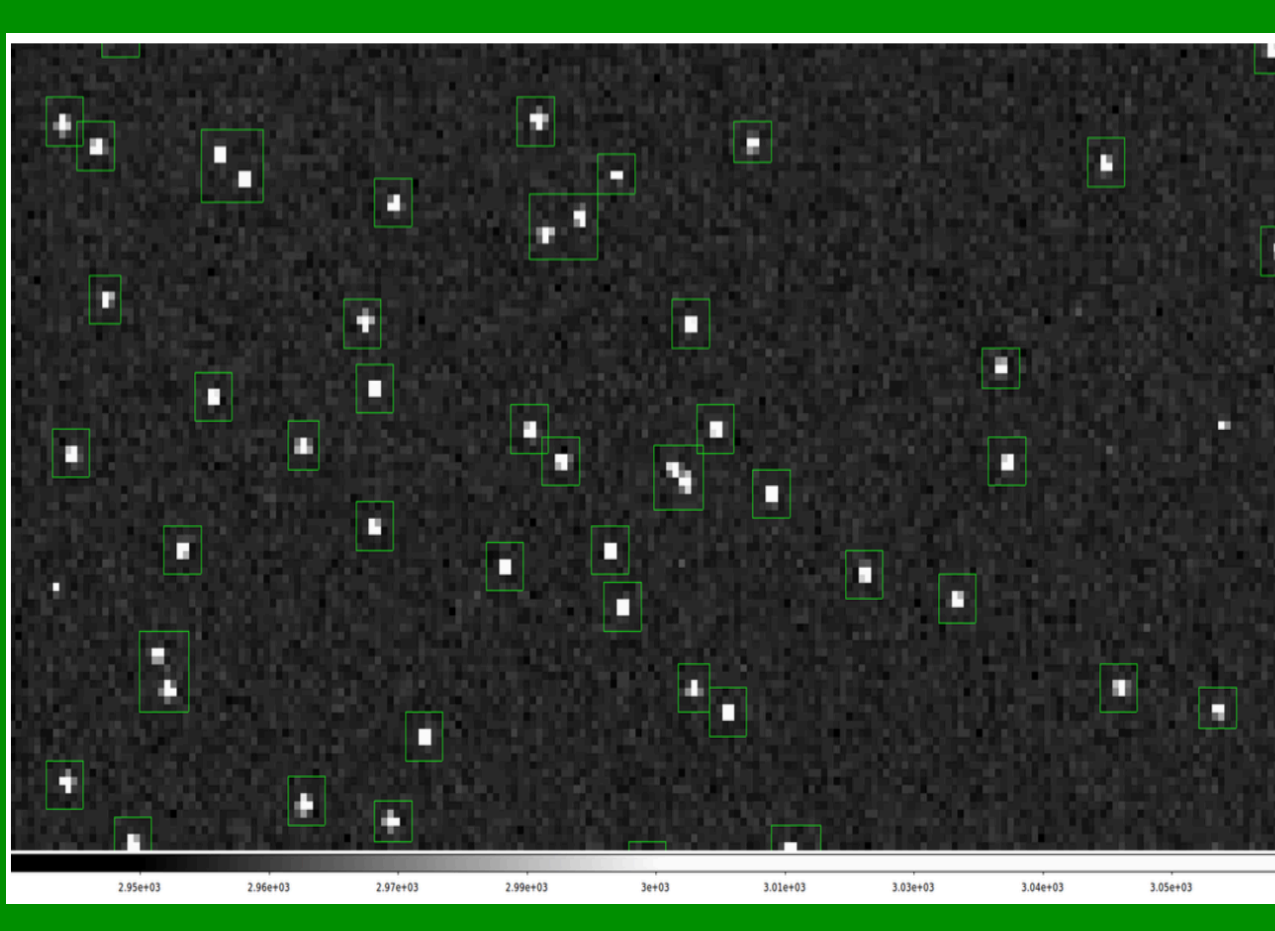


- We analyze **data** from the **Dark Energy Survey (DES)** to study biases induced by the CCDs.



X-ray flats in LSST CCDs

- We use **x-rays** hits on the CCDs of the **Large Synoptic Survey Telescope (LSST)** to probe for instrumental signatures on observables.



WFIRST detector requirements



- We use **custom simulations** to derive requirements for the detectors of the future **NASA's WFIRST** mission.

Astrometric and Photometric Biases in DES

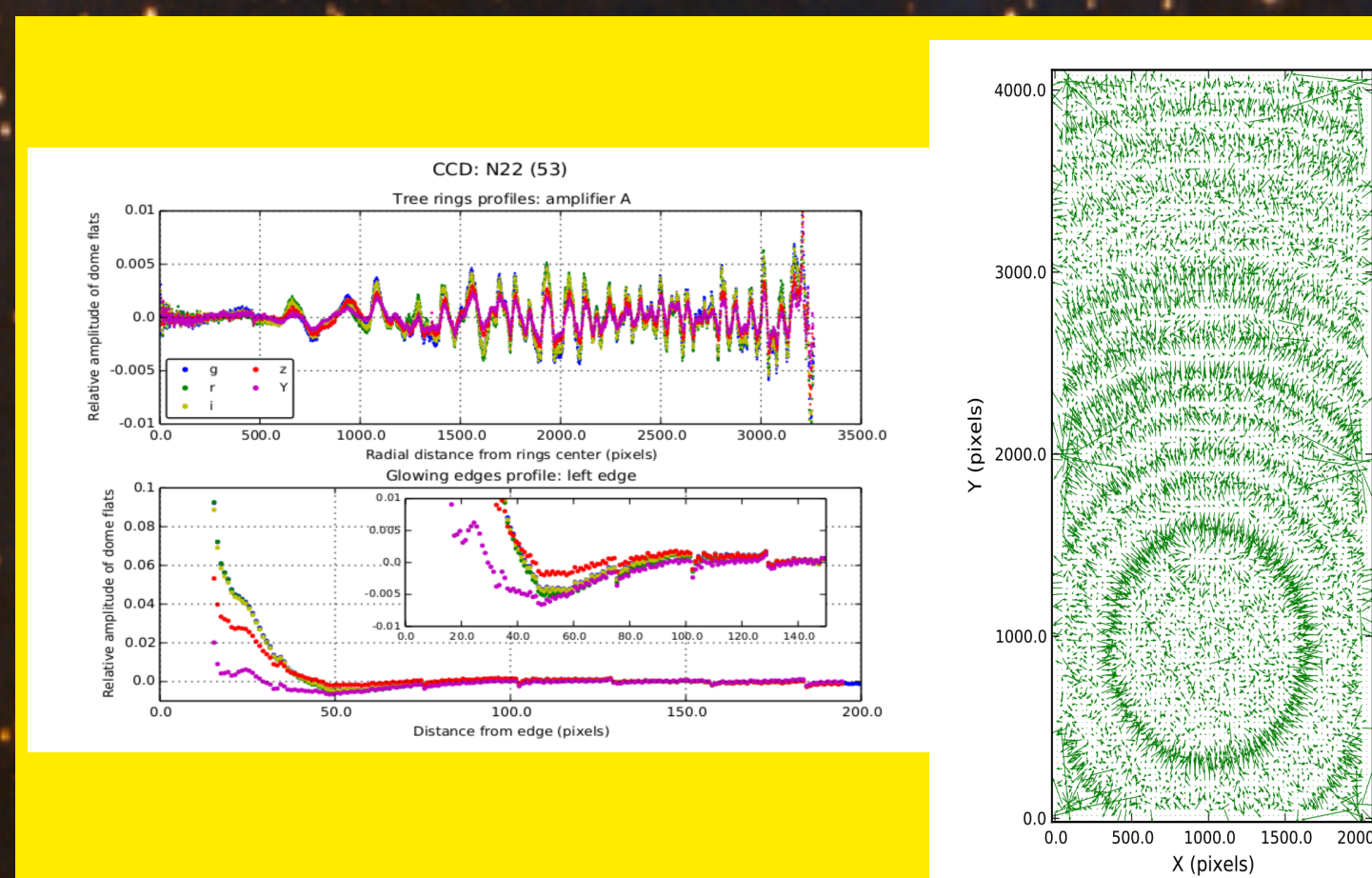


Fig. 1 Astrometric residuals from star positions (right) and photometric profiles in flat fields (left) in DES sensors.

- Structures in dome flats correlate with **biases in astrometry and photometry.**

Induced correlations in LSST CCDs

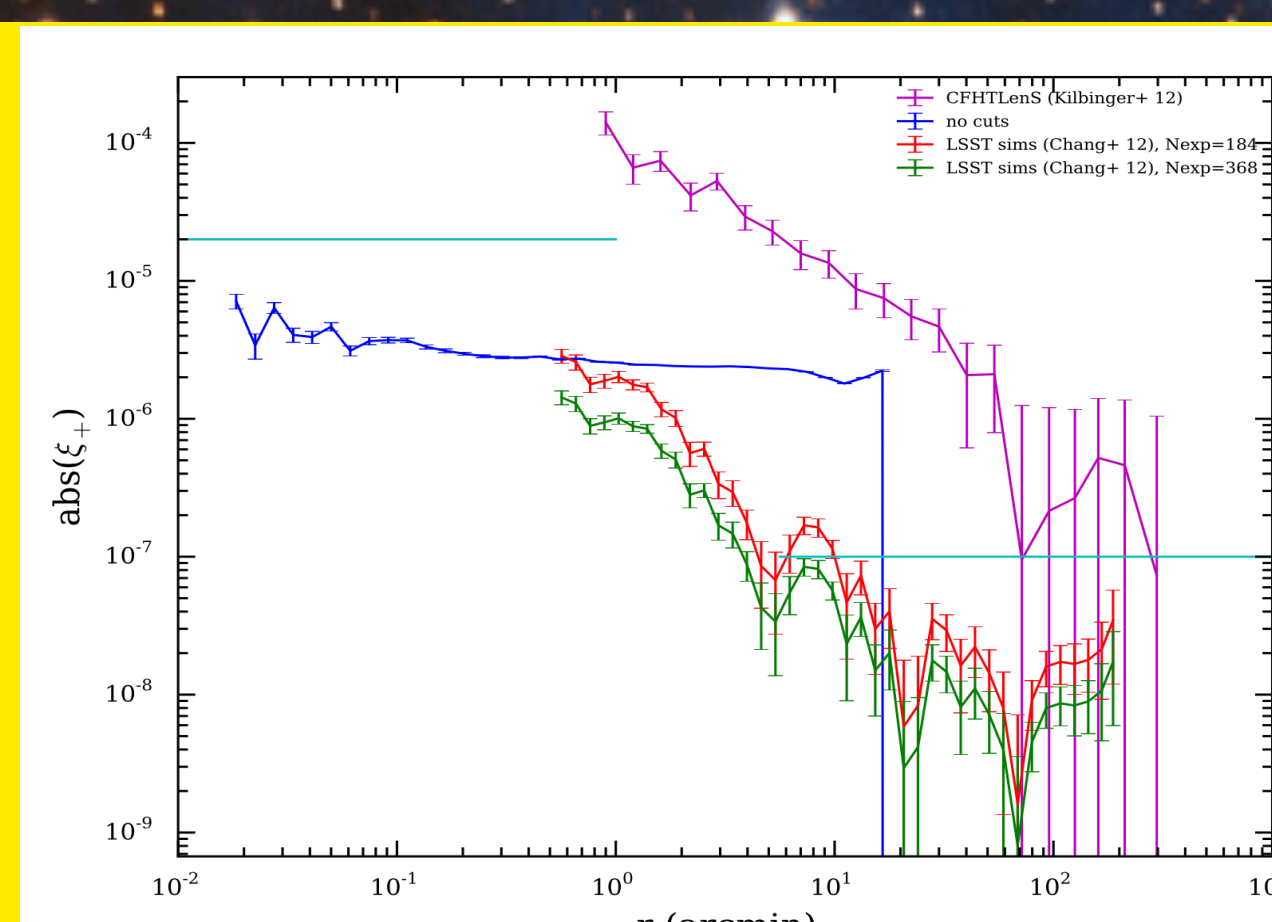
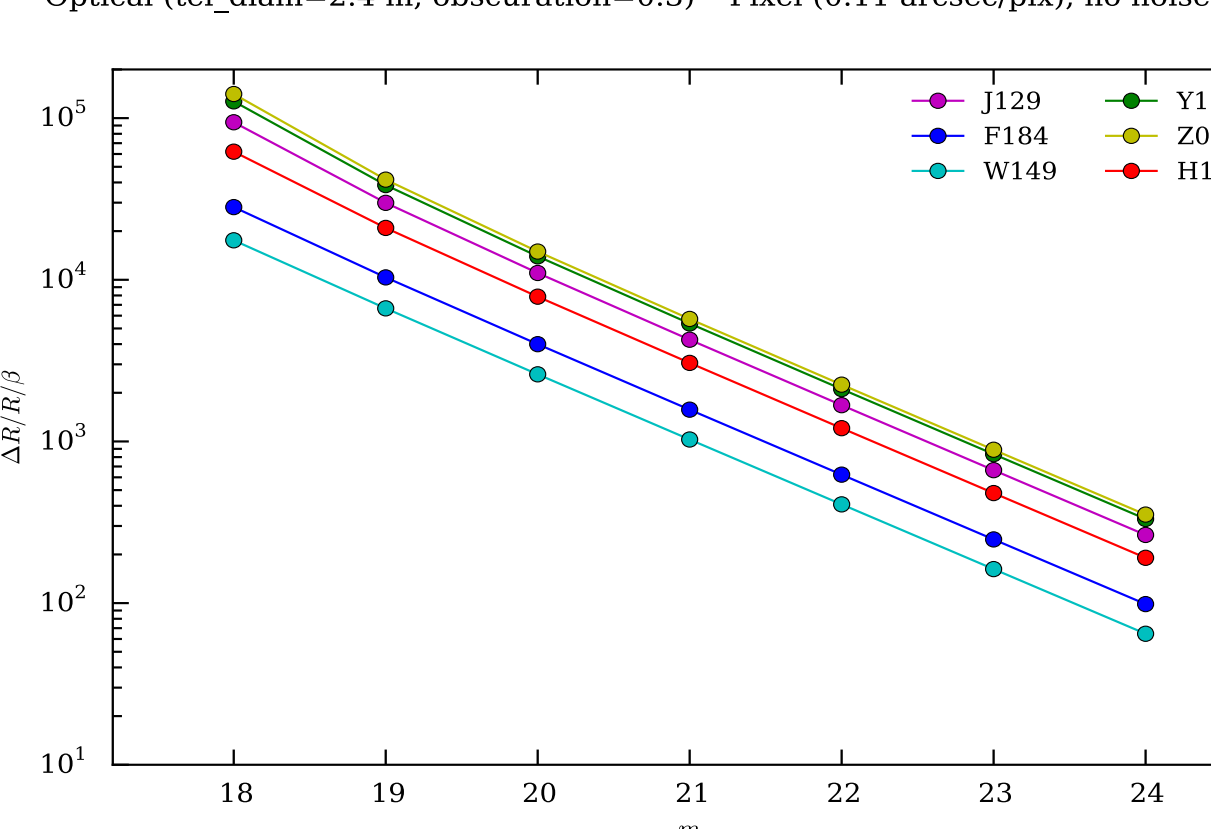


Fig. 2 Two-point correlation in object shapes as function of separation

- Distortions at the CCD edges induce non-negligible **spurious correlations in shapes** (work in progress).

Requirements for WFIRST detectors

Non-linearity: $f = x - \beta x^2$
Optical (tel_diam=2.4 m, obscuration=0.3) * Pixel (0.11 arcsec/pix), no noise.



- Simulations show that **voltage non-linearity** induce fractional **biases in size and shape** (work in progress).

Fig. 3 Fractional error in size normalized by non-linearity as a function on magnitude for all the WFIRST filters

Conclusions and future work

- Sensor effects produce **sizeable biases in WL observables** for the study of **Dark Energy**.
- We will use simulations and lab measurements to generate **requirements for the WFIRST detectors.**

Galactic environment effects on gravitational wave signals in pulsar-timing arrays

Principal Investigator: Stephen Taylor (335)

Eliu Huerta (WVU), Jonathan Gair (IoA, Cambridge), Sean McWilliams (WVU)

1

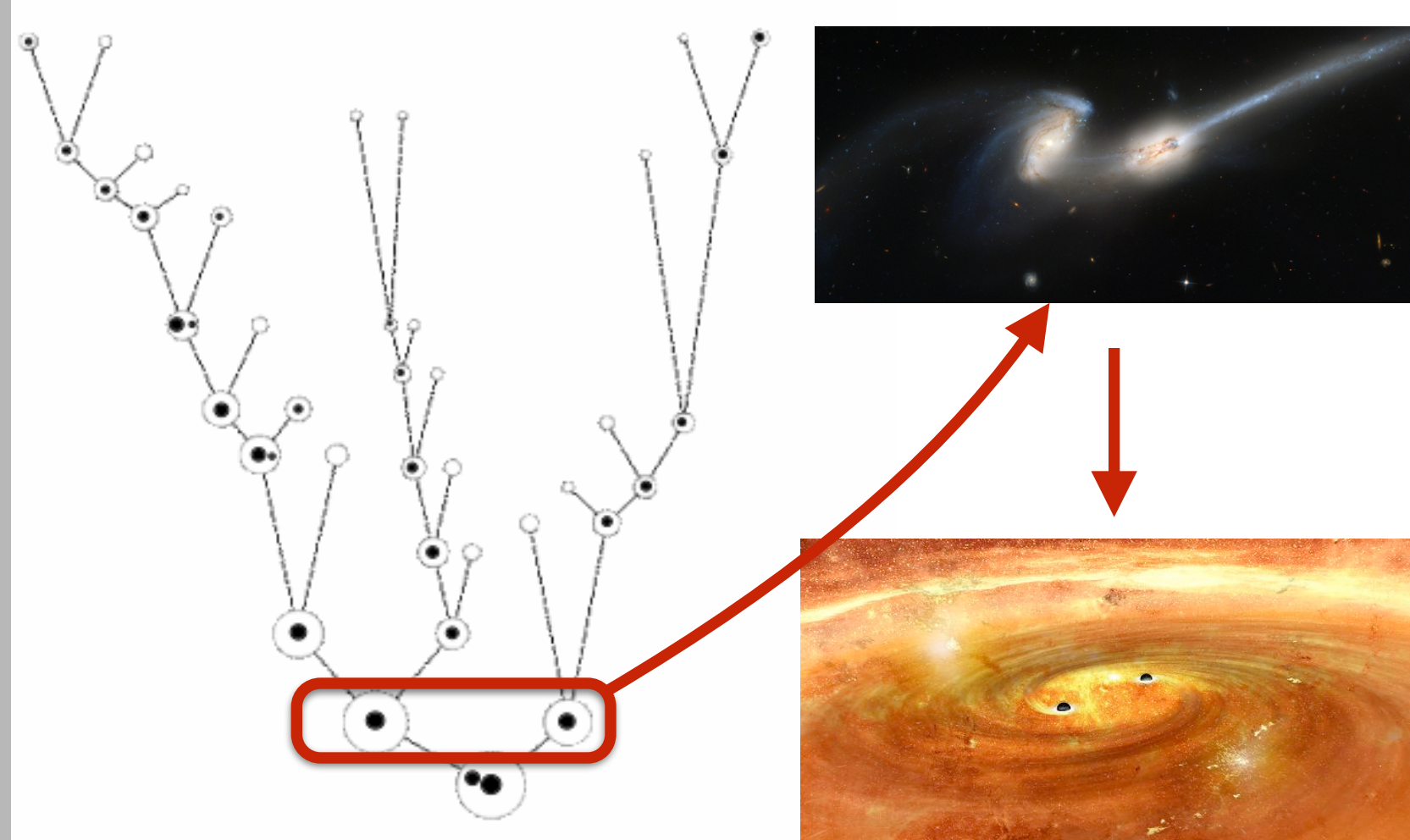
Overview and project aim

- Precision timing of dozens of Milky Way millisecond pulsars permits searches for extragalactic gravitational waves (GWs) via the deviations to the arrival times of radio pulses that they cause. The sources of these GWs are likely to be binary systems of supermassive black holes, which form when galaxies merge together throughout cosmic history.
- Until now, data analysis approaches have not modeled the early phase of the black holes sinking towards merger. This can be significantly impacted by interactions with the central galactic environments, and leave a residual signature in the GW signals being pursued with pulsar-timing searches. This project is aimed at tracking the orbital evolution of the most massive black hole systems, so that we can extract information about the influence of astrophysical environments and constrain the various mechanisms which hope to resolve the "final parsec problem".

2

Galaxy formation and black hole mergers

- The current paradigm of galaxy formation sees galaxies undergo repeated merger events throughout cosmic time.
- When galaxies merge, the black holes in their centers sink together within the common merger remnant via dynamical friction. But this stops being efficient at black hole separations of ~ 1 pc.

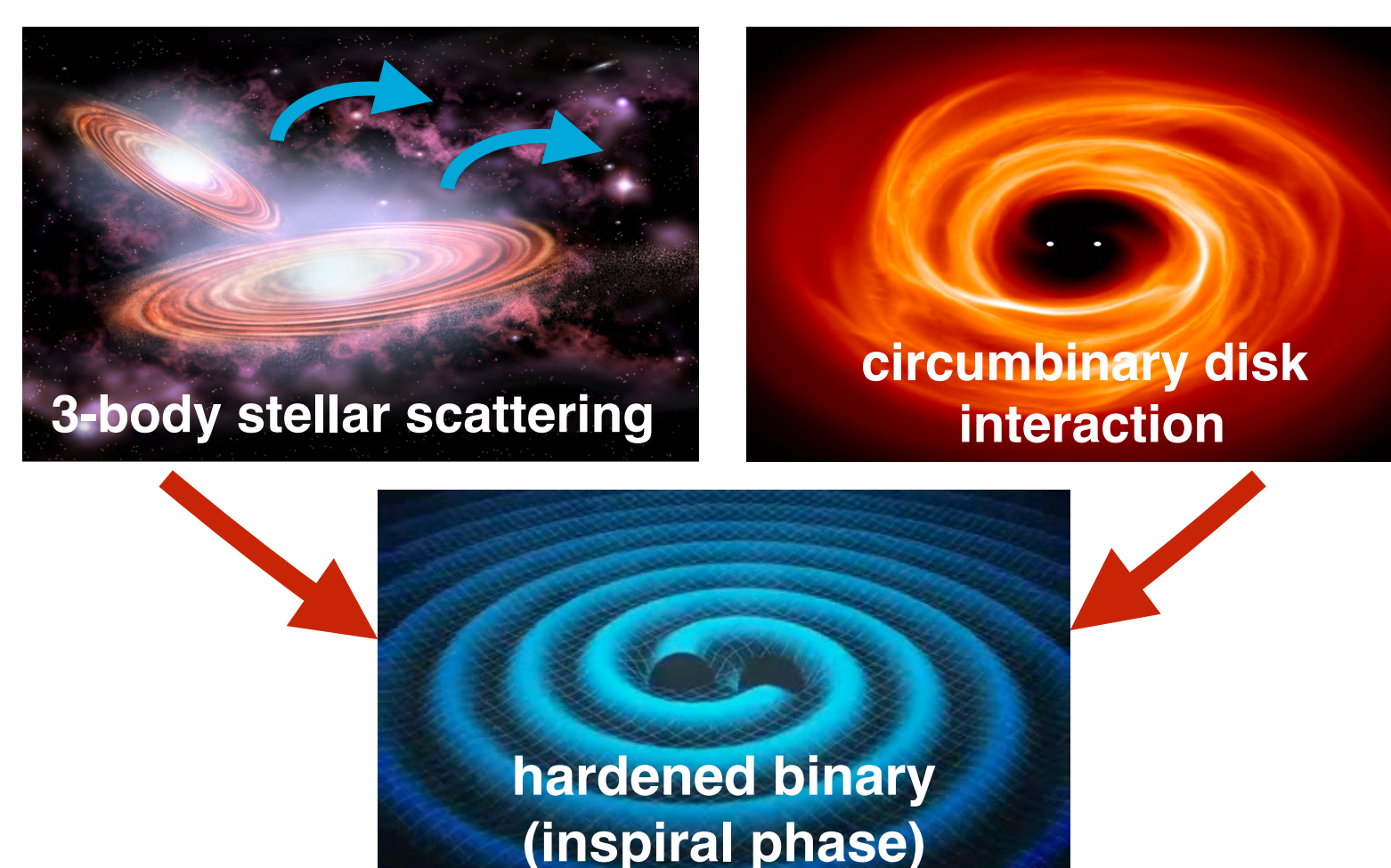


(Left): A galaxy merger tree, showing small galaxies merging together to form larger ones. (Top right): Image of interacting galaxies, showing distinctive tail features. (Bottom right): Illustration of the resident black holes sinking together.

3

The final parsec problem

- Dynamical friction is highly inefficient at small black hole separations. The emission of GWs is our target signal, but is only efficient at separations of $\sim 0.01 - 0.001$ pc.
- There must be other mechanisms, otherwise the black holes would never merge within a Hubble time ("final parsec problem").

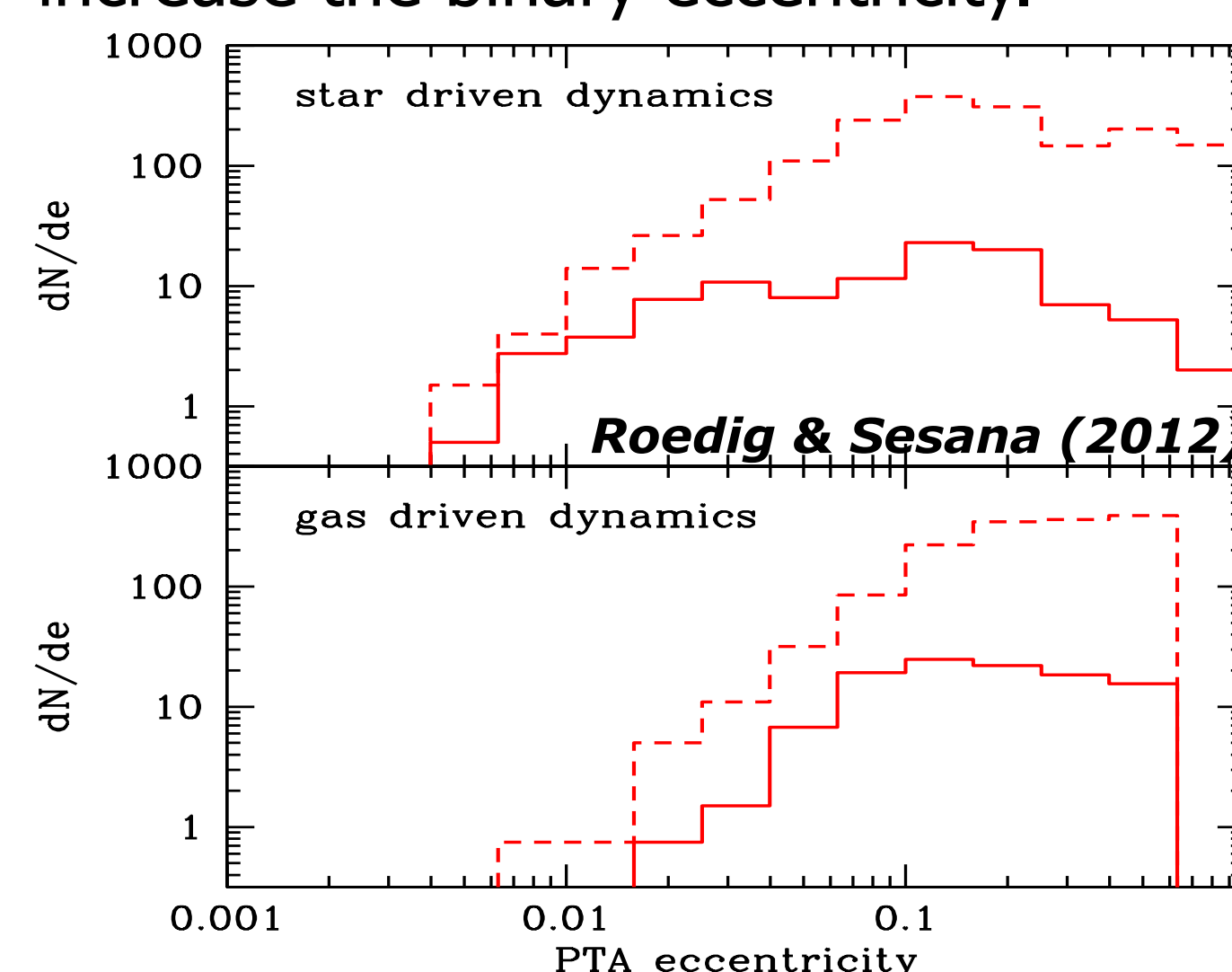


- These mechanisms extract energy and angular momentum from the binary, driving it to smaller separations, and allowing GW emission to take over as the dominant evolving mechanism.

4

The environment increases binary eccentricity

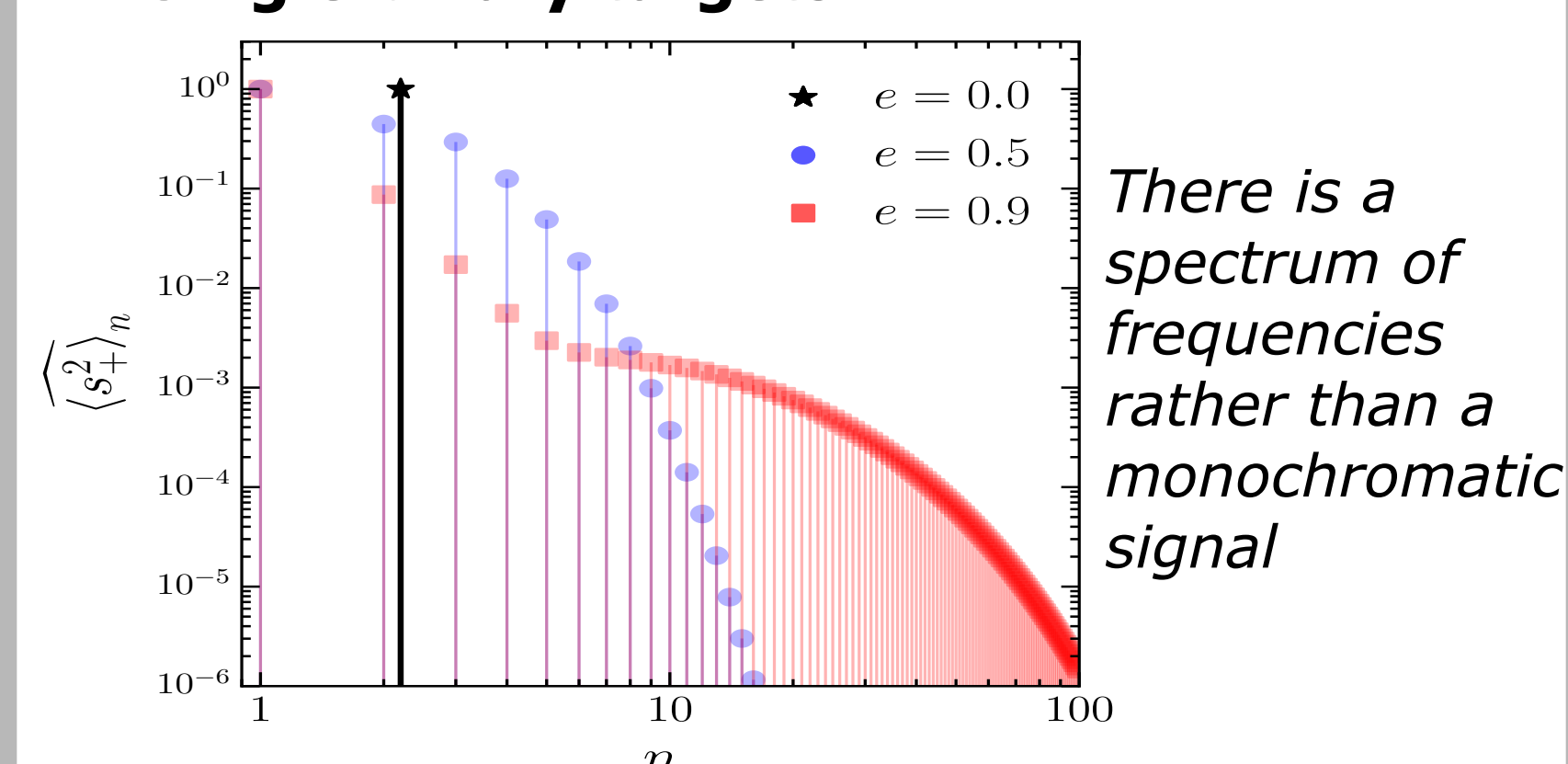
- These mechanisms can mitigate the final parsec problem, but can also drastically increase the binary eccentricity.



5

Eccentricity impacts GW signals

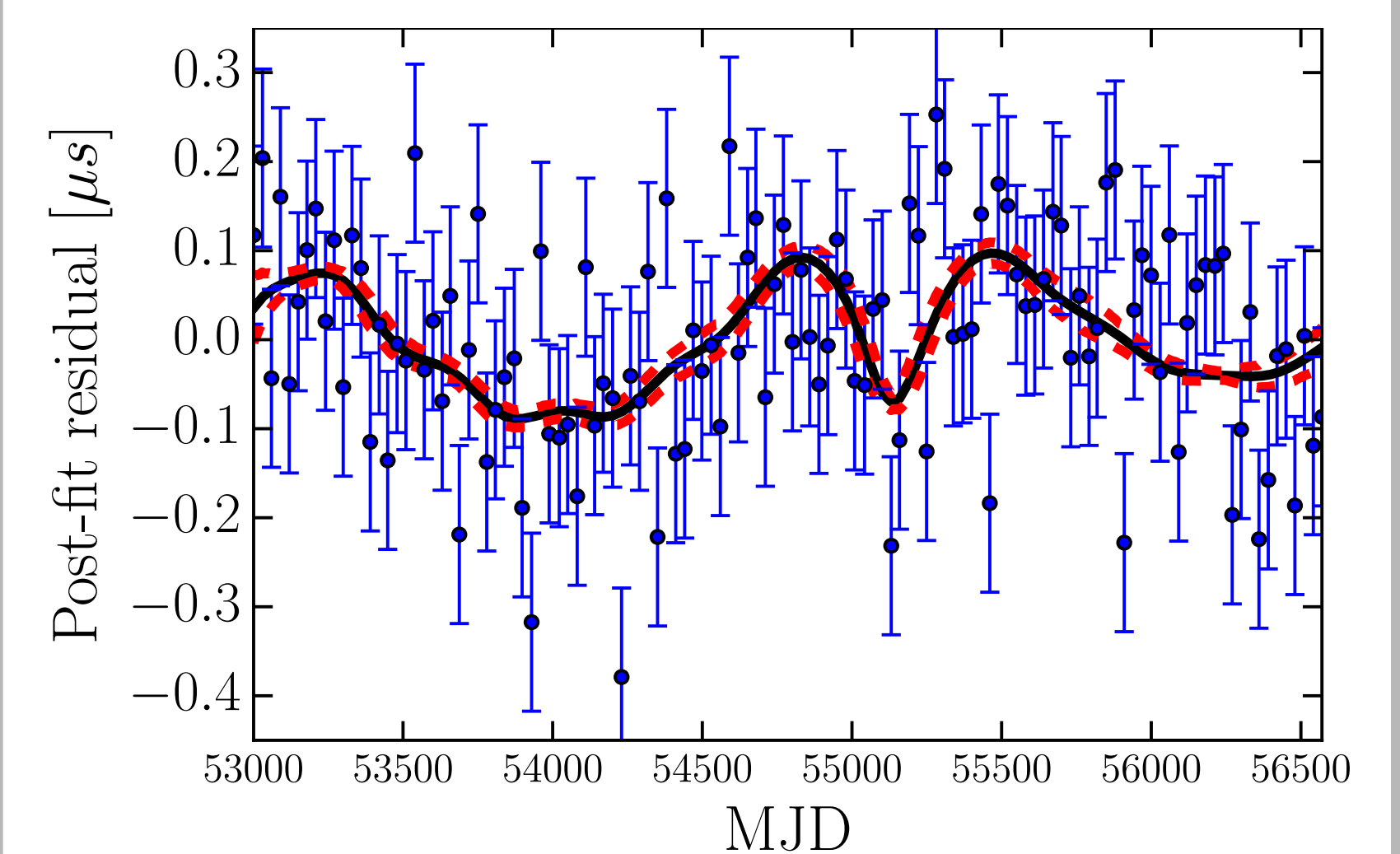
— Single binary targets



6

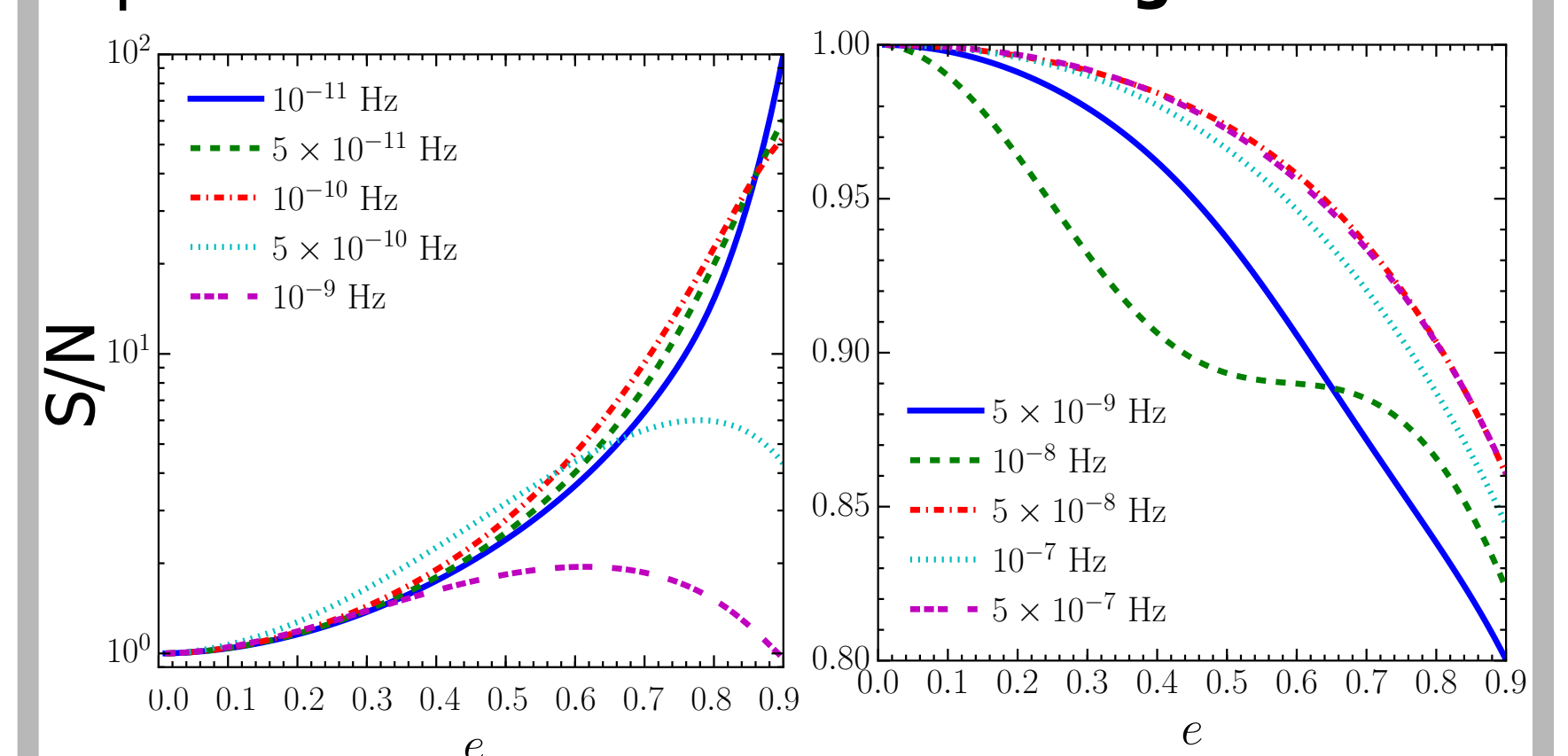
Building an eccentric single binary pipeline

- We solve the eccentric binary orbit using a Fourier analysis.
- The GW amplitude is then given analytically.
- Integrate over GW amplitude and pulsar response to give analytic signal model.



Simulated pulsar-timing data (blue points) containing a GW signal from an eccentric binary. The Bayesian recovered GW waveform is shown in black and red, illustrating excellent recovery. The burst feature around MJD 55100 is a binary periastris passage.

- Eccentricity spreads the GW signal into frequencies higher than the orbital frequency.
- This causes ultra-low frequency binaries to have signals pushed into the pulsar-timing band, whilst moderate frequency signals are pushed out of band. "Double-edged sword"



7

Conclusions

- Astrophysical environments of black hole binary systems can impact the binary's orbital evolution.
- We can now model eccentric binary signals in pulsar-timing analyses.
- Constraining binary eccentricity will provide invaluable insights into the environmental mechanisms proposed to mitigate the final parsec problem.
- NASA's DSN will allow us to expand our catalog of timed pulsars, improving our prospects for GW detection and precision science.

Panels 5 through 7 contain material directly from Taylor et al. (2015), arXiv:1505.06208, submitted to ApJ

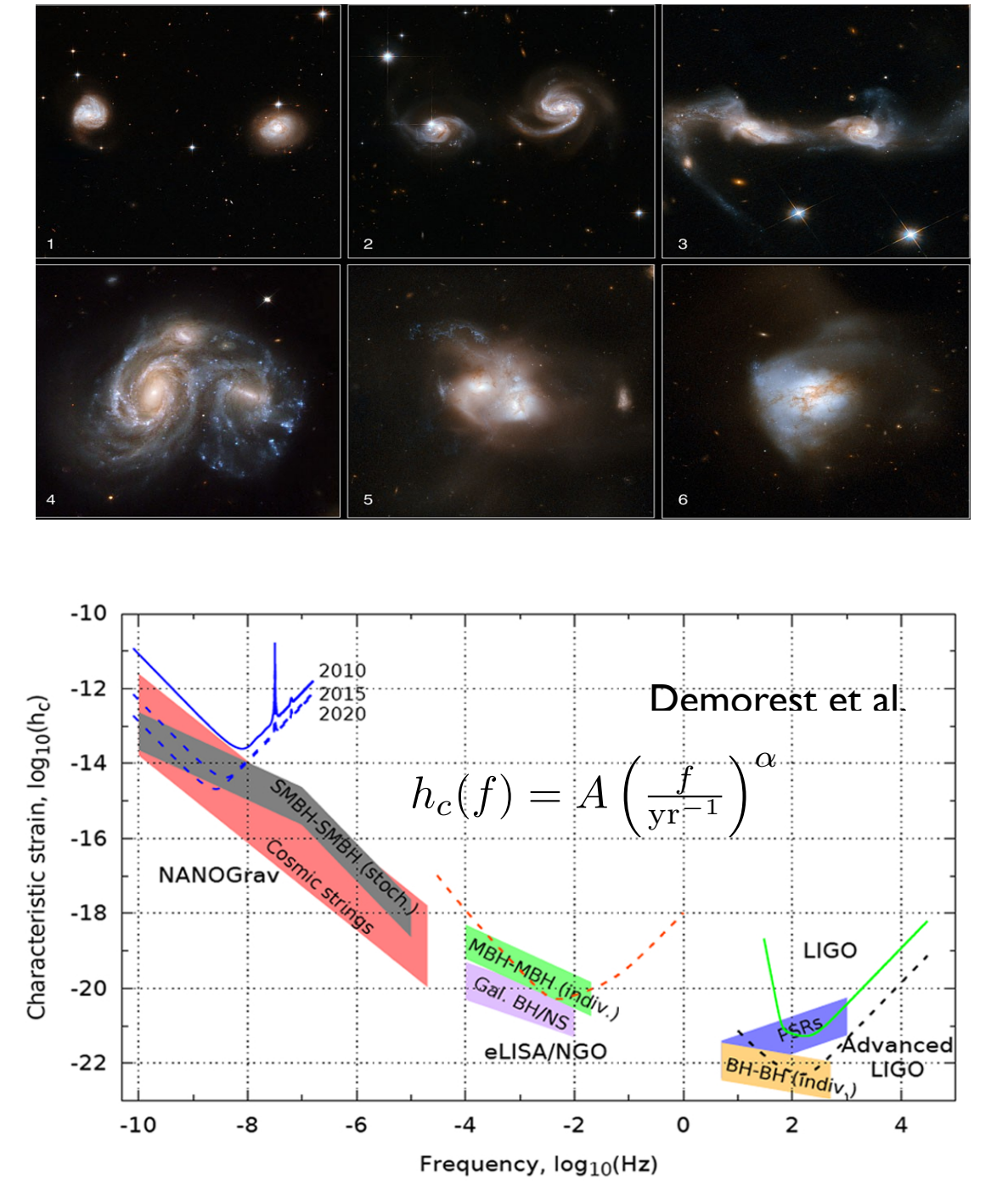
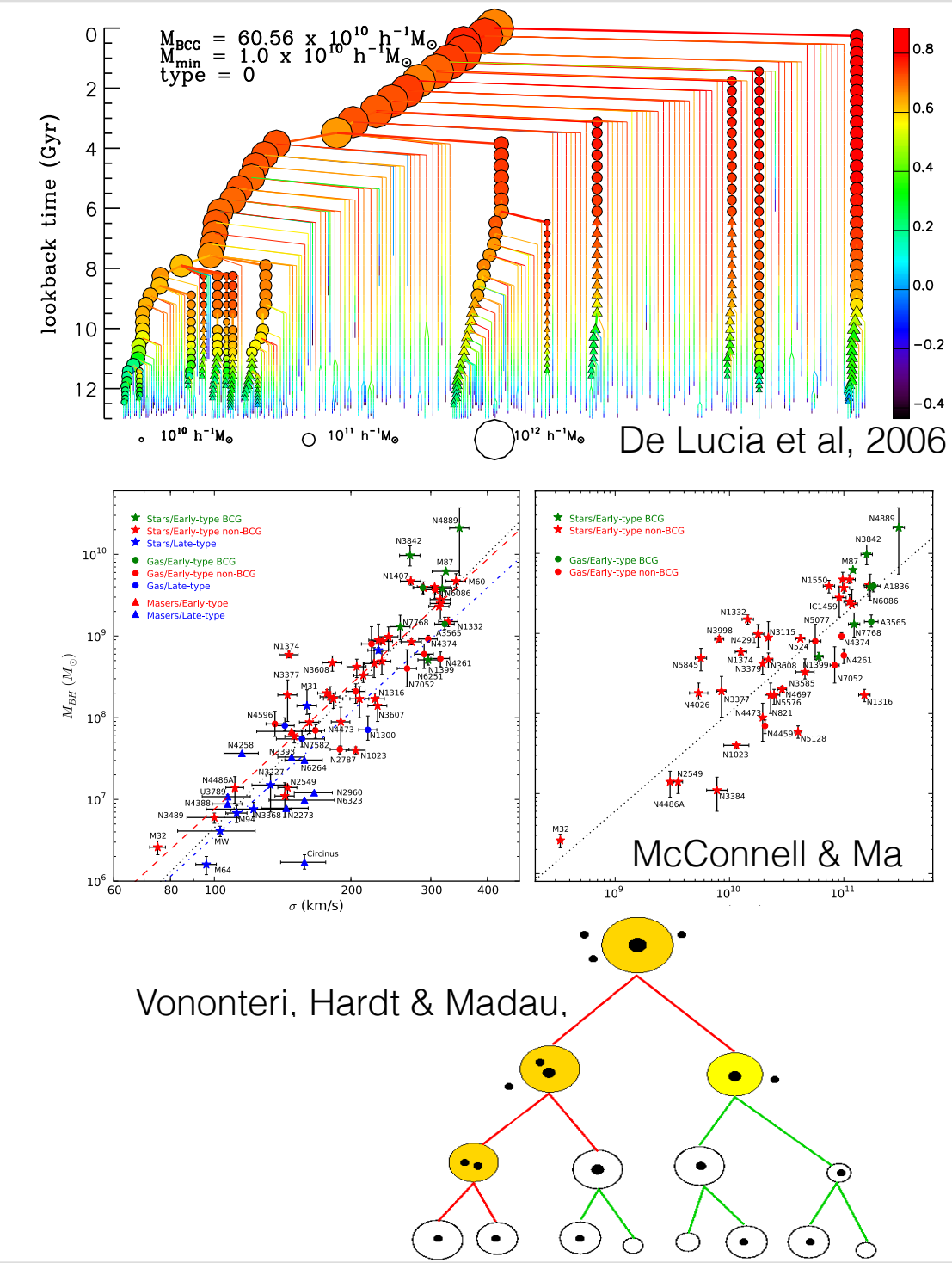
Limits on the Isotropic Stochastic Gravitational Wave Background from the NANOGrav PTA

Principal Investigator: Justin Ellis* (335)

Rutger van Haasteren* (335), Stephen Taylor* (335), Michele Vallisneri* (335)

Overview and Project Aim:

Pulsar timing arrays (PTAs) offer a unique opportunity to detect low frequency gravitational waves (GWs) in the near future. In this frequency band, the expected source of GWs are Supermassive Black Hole Binaries (SMBHBs) and they will most likely form in an ensemble creating a stochastic GW background with the possibility of a few nearby/massive sources that will be individually resolvable. We present upper limits on the strength of the isotropic stochastic background of gravitational waves using the new 9-year North American NanoHertz Observatory for Gravitational Waves (NANOGrav) data release. Using several published models for the merger rate of SMBHBs we place meaningful constraints on the transition frequency at which environmental factors such as stellar hardening and circumbinary interactions become comparable to the energy loss due to GW emission. Furthermore, we can use these constraints to place limits on stellar density in galaxy cores and the eccentricity of SMBHBs entering GW merger.



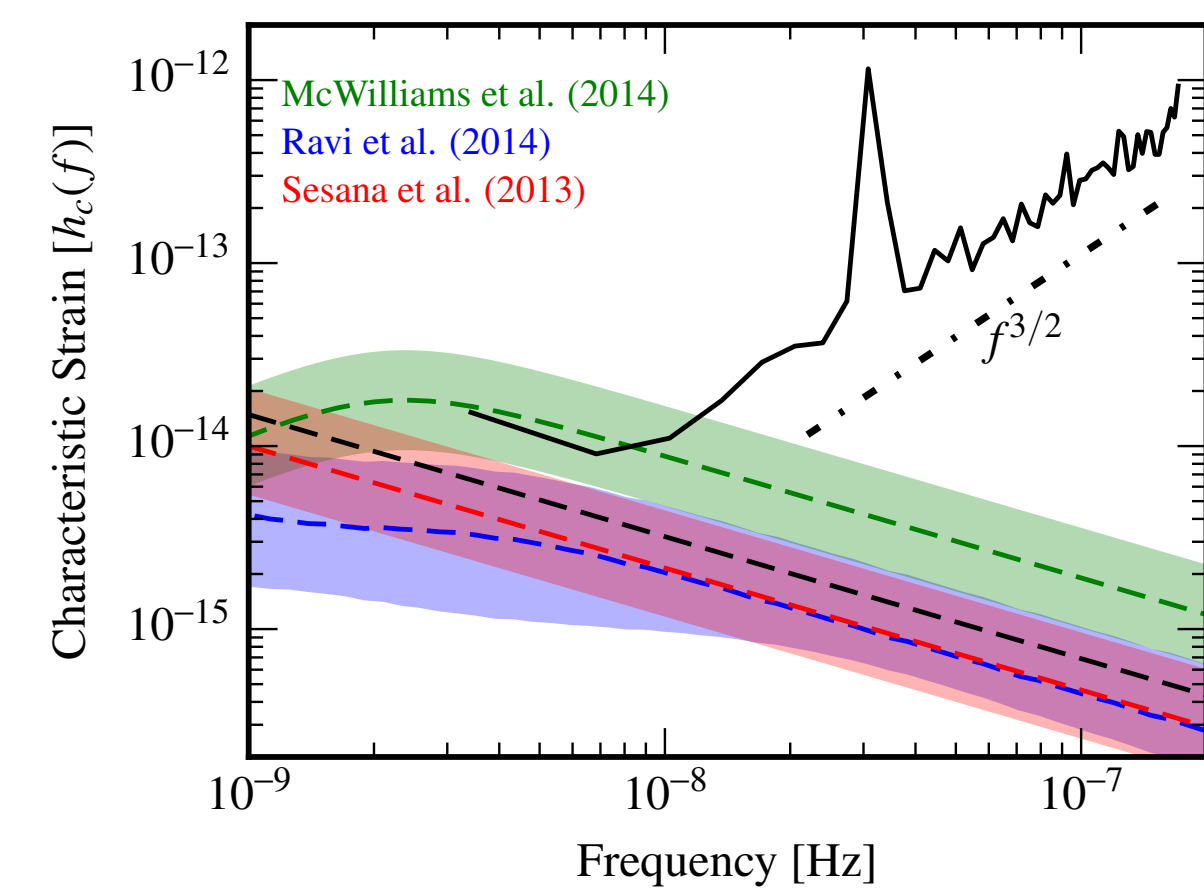
Power-law upper limits:

Under the assumption of a GW dominated merger the amplitude of the stochastic GW background is a power law of the form:

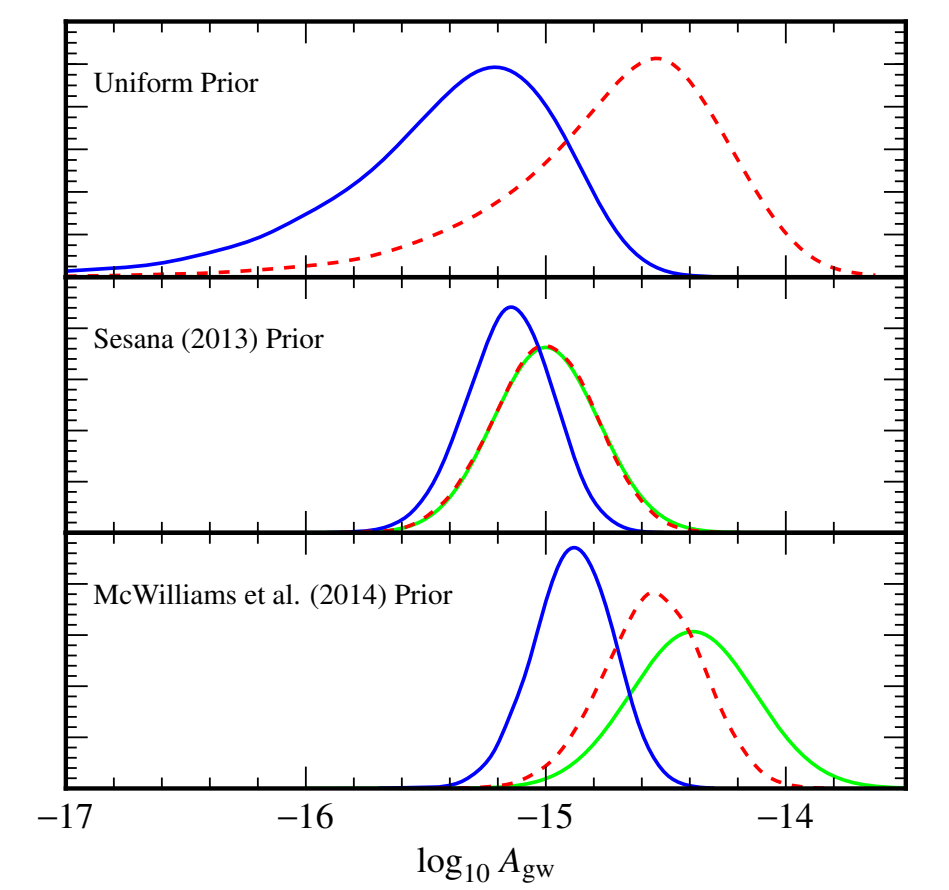
$$h_c(f) = A_{\text{gw}} \left(\frac{f}{\text{yr}^{-1}} \right)^{-2/3}$$

Several models make different predictions for the range of the dimensionless amplitude making different assumptions about the galaxy merger rate and host-galaxy black hole relations.

Using both non-informative and astrophysical priors, our upper limits are in tension with some astrophysical models and are beginning to rule out significant areas of parameter space for others. Furthermore we place significantly more constraining upper limits with the 9-year data release as opposed to the 5-year release.



Power law (dashed black) and spectral (solid black) upper limits using uniform priors on the strain amplitude. Also plotted in red, blue and green are the one-sigma confidence regions for different predictions of the GW strain spectrum.



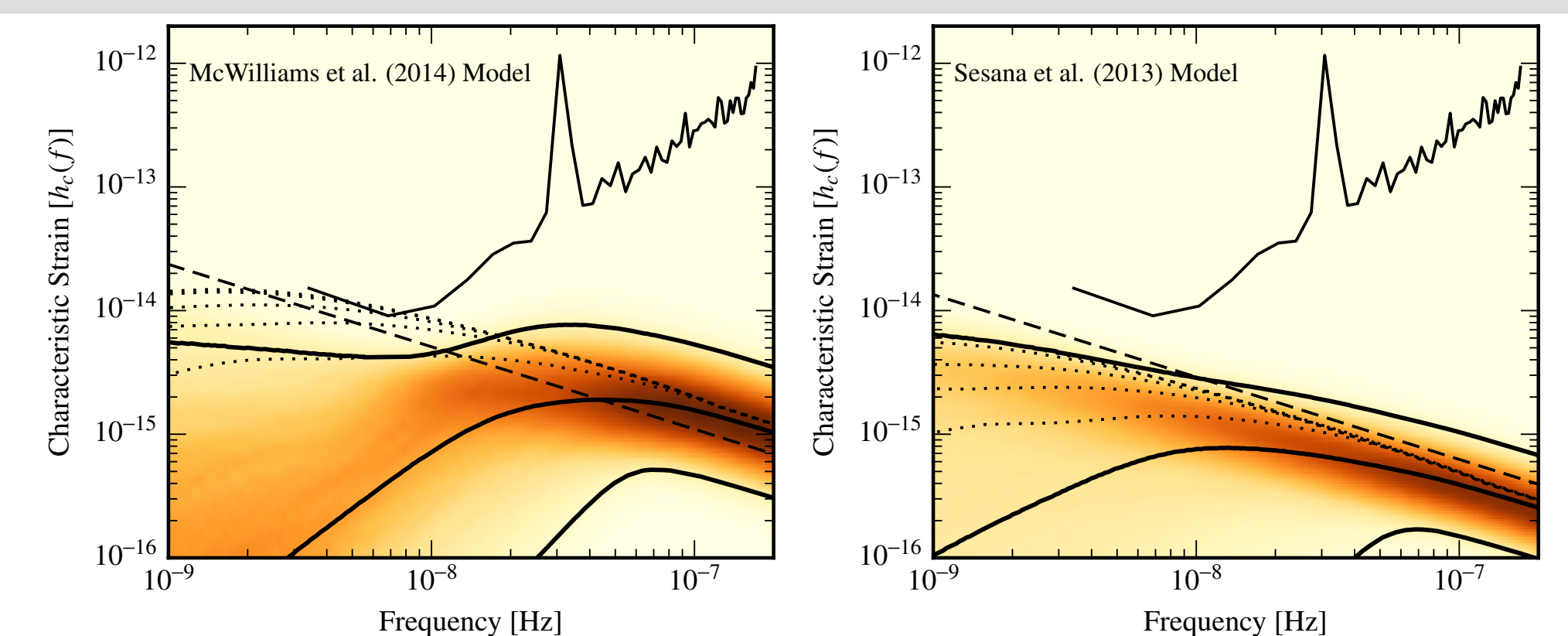
Posterior distribution for GW amplitude for different priors (green) for both the 9 (blue) and 5 (red) year data releases. It is shown that the 9-year data release is significantly more constraining than the 5-year set.

Broken power-law upper limits:

For the SMBHB to merge in a Hubble time, stronger driving mechanisms must dominate the evolution of the binary at large orbital separations (i.e low frequencies); however, it is unknown where the system will transition from environmentally driven to GW driven. If we assume that this transition region is in our frequency band then the GW strain spectrum is:

$$h_c(f) = A_{\text{gw}} \frac{(f/\text{yr}^{-1})^{-2/3}}{(1 + (f_{\text{bend}}/f)^\kappa)^{1/2}}$$

Using this more flexible model we can determine whether or not our data is consistent with a power-law and where a possible transition from environmental to GW driven takes place. Using optimistic models for the strength of the GWB in the GW dominated regime, we find that our data strongly prefers a model with a turnover in the spectrum, whereas more conservative models are still consistent with a power-law.



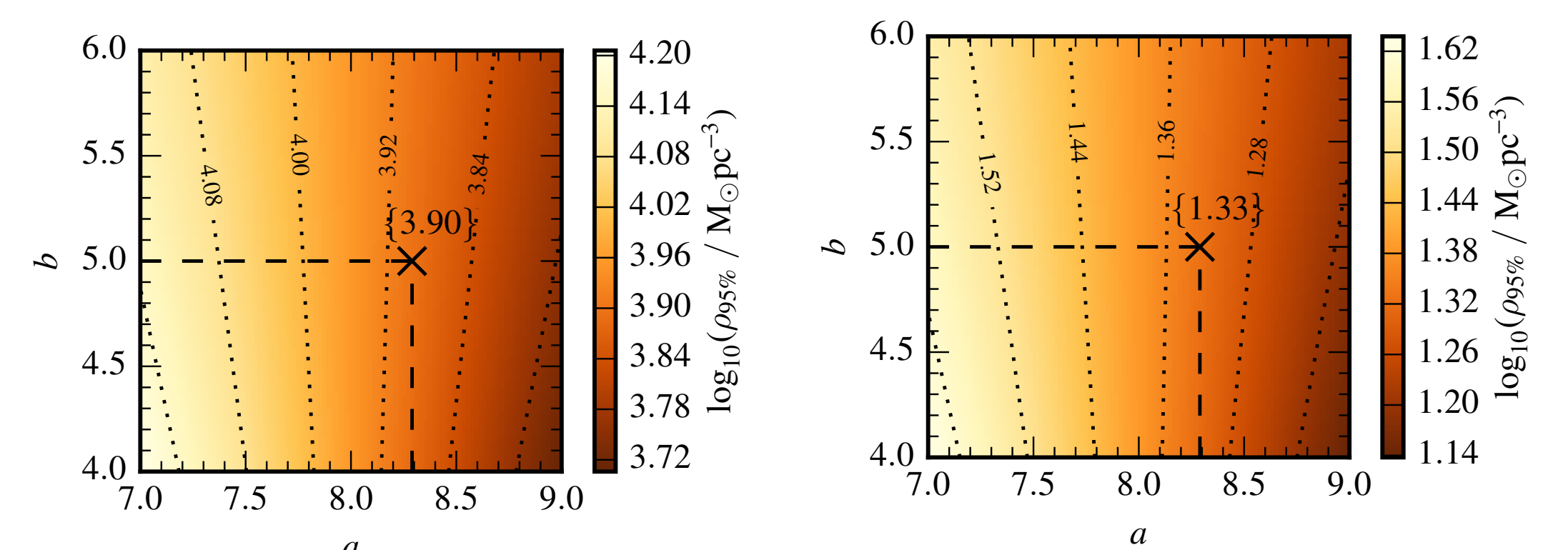
Posterior pdf of the GWB strain spectrum for two different models of the GWB amplitude in the GW driven regime. The thick solid black lines are the 95% confidence region and median of the broken power-law GWB strain spectrum, respectively. The dashed line is the pure-power-law upper limit assuming an amplitude prior predicted by the model. The dotted lines are the predicted mean spectrum for different eccentric populations from 0 to 0.9 (top to bottom). The pdf in the left panel indicates that this more optimistic model is only consistent with our data if a large fraction of binaries have large eccentricities (> 0.9) or the binaries are still tightly coupled to their environments.

Astrophysical Interpretation:

Using the above constraints with the broken power law model we can map our constraints on the decoupling frequency to physical parameters assuming a specific environmental driving mechanism such as stellar hardening. The most interesting and most unconstrained (especially at large redshifts) is the stellar density of the galaxy. However this mechanism is also sensitive to the relationship between the mass of the binary and the stellar velocity dispersion, this is known as the M-sigma relation

$$\log_{10} M_\bullet = a + b \log_{10} \left(\frac{\sigma}{200 \text{ km/s}} \right)$$

We use the broken power law limits to place a 95% lower limit on the stellar density as a function of the parameters of the M-sigma relation. We find that for both the optimistic and conservative models, the lower limit on the stellar density is quite robust to changes in the M-sigma relation.



95% lower limits on the stellar density as a function of the M-sigma parameters. The left and right panels represent the optimistic and conservative signal models. The more optimistic signal model predicts a lower limit on the stellar density that is nearly 3 orders of magnitude larger than the more conservative signal model. This limit is in tension with observations at z=0 which predict that the stellar density is on the order of 10 solar masses per cubic parsec. However, the SMBHBs contributing to the stochastic background are at larger redshifts (i.e. z=0.5-2) where the stellar density is not measured. Nonetheless, this limit shows that stellar hardening must be very efficient if this optimistic model is true.